The impact of wind forcing on estuarine circulation

Dissertation

zur

Erlangung des akademischen Grades

doctor rerum naturalium (Dr. rer. nat.)

der Mathematisch-Naturwissenschaftlichen Fakultät

der Universität Rostock

vorgelegt von

Xaver Lange, geb. am 19. März 1991 in Stralsund

aus Rostock

Rostock, 19. Dez. 2018

Kurzfassung

Ästuare sind vielfältige Systeme deren Dynamik durch eine bidirektionale Austauschströmung charakterisiert ist, mit einem bodennahen, landwärtigen Einstrom von salzhaltigem Seewasser, der sich mit Süßwasser des Flusses vermischt und in einen oberflächennahen Ausstrom verwandelt wird. Neben dem Dichtegradienten zwischen Fluss und Meer, den durch Gezeiten induzierten Effekten und den lateralen Prozessen, stellt Wind ein Schlüsselmechanismus in vielen Ästuaren dar. Hierbei zeigt sich, dass Wind, im Gegensatz zu den anderen genannten Antrieben, zumeist hoch variabel ist - sowohl in seiner Stärke als auch in seiner Richtung, was die Frage nach der Sensitivität von ästuarinen Strömungen gegenüber Wind aufwirft.

Diese Arbeit präsentiert Ergebnisse, die den Einfluss von Wind auf die ästuarine Austauschströmung beschreiben. Eine neu aufgestellte analytische Formulierung von windgetriebenen Strömungsprofilen motiviert eine kritische basis Wedderburn Zahl (Verhältnis von nicht-dimensionaler Windschubspannung und Dichtegradienten) als beschreibendes Maß für die Sensitivität eines Ästuars gegenüber Wind. Es zeigt sich, dass in der idealisierten stationären Lösung landwärts gerichteter Wind in der Lage ist die klassische Austauschströmung umzukehren, wenn die basis Wedderburn Zahl 15% erreicht. In der Gegenwart von Gezeiten, und deren Rückkopplung von vertikaler Vermischung und Schichtung auf die Austauschströmung, zeigen numerische Simulationen einen schrittweisen Anstieg auf etwa 45% an, wodurch drei mal mehr Wind benötigt wird um die Zirkulation umzukehren. Zusätzliche Berücksichtigung von lateralen Effekten erhöht diesen Wert weiter auf bis zu 130%. Realistische Simulationen von einem Ästuar im Wattenmeer (60%) und einem quasi gezeitenfreien Ästuar in der Ostsee (33%) zeigen die Anwendbarkeit und die Robustheit der Theorie gegenüber transienten Verhältnissen.

Abstract

Estuaries are diverse systems characterized by a bidirectional exchange flow, with a near-bottom landward inflow of saline seawater, which is mixed with riverine freshwater and transformed into a near-surface outflow. Aside from the density gradient between the river and the ocean, tidally induced effects, as well as lateral processes, wind is a key mechanism in estuaries. The latter is, contrary to the other drivers listed, often highly variable in magnitude and directionality, raising the question of the sensitivity of the estuarine circulation to wind forcing.

The present study shows results describing the influence of wind on the estuarine exchange flow. A newly derived analytical formulation of wind-driven along-estuary velocity profiles motivates a critical basic Wedderburn number (balance of non-dimensional wind stress and density gradient) as a measure for the sensitivity of an estuary to wind. Results show that in the idealized stationary solution up-estuary wind stress is able to invert the classical exchange flow direction when the basic Wedderburn number has reached 15%. Numerical simulations suggest that in the presence of tides, and their feedback of varying vertical mixing and stratification on the estuarine circulation, this value increases stepwise to up to approximately 45%, meaning that three times more wind is necessary to invert the circulation. The basic Wedderburn number increases even further to up to values of 130% if lateral effects are additionally taken into account. Realistic simulations of a tidally energetic estuary in the Wadden Sea (60%) and a weakly tidal estuary in the Baltic Sea (33%) confirm the applicability and robustness of the newly developed theory towards transient conditions.

Contents

List of Figures

1 Introduction

Estuaries are complex coastal systems that can be found all over the world and differ in numerous aspects, such as bio-geo-chemistry, morphology and physics. Their diversity makes them an interesting object of study, but complicates a comprehensive definition. A commonly accepted, however not universally valid, definition has been suggested by Cameron and Pritchard (1963) defining estuaries as "a semi-enclosed and coastal body of water with free communication to the ocean within which ocean water is diluted by freshwater derived from land" (Valle-Levinson, 2010). Focusing on the latter Wang et al. (2017) recently described an estuary as "a mixing machine that combines high salinity water from the ocean with fresh water from the river to form intermediate-salinity water." In order to classify the diversity of estuaries, various criteria have proven themselves useful. Besides applying classifications based on the geomorphology of estuaries, differentiating in types of fjord, coastal plain, bar-build and tectonic (Pritchard, 1952a), they can be distinguished e.g. by their water balance or vertical structure of density (stratification).

When considering the estuarine water balance in terms of direction of the net inflow and outflow volume fluxes, estuaries are classified as either positive (or classical) or negative (or inverted). Classical estuaries have in common that a net near-bottom landward inflow transports seawater into the estuary which is then transformed by estuarine processes (e.g. mixing) into a net near-surface seaward directed outflow (Fig. 1), when averaged over a certain period of time (e.g. the tidal cycle). This bidirectional exchange flow, also referred to as estuarine circulation, is a key mechanism in estuarine dynamics (MacCready and Geyer, 2010; Geyer and MacCready, 2014). A consequence of this is that the estuarine salinity as well as the up- and down-estuary volume fluxes increase when moving seaward reaching their maximum at the mouth. The outflow discharge, potentially forming a river plume, is therefore typically larger than the river discharge itself. In contrast to a positive circulation, inverse estuaries are identified by a net near-surface landward transport of volume in combination with a compensating net outflow near the bottom pointing seaward. Note that negative estuaries, as those existing e.g. in arid regions characterized by strong evaporation, are often found to have a reversed horizontal salinity gradient as for example observed in the Persian Gulf (Johns et al., 2003) or in the Spencer Gulf in south Australia (Nunes and Lennon, 1986). Inverted circulation is additionally observed in the presence of strong landward wind (Scully et al., 2005). In special cases a combination of both, classical and inverted circulation, exist in estuaries. Low-inflow estuaries (e.g. Wolanksi, 1986) are observed to have a negative circulation near the mouth, in the presence of strong evaporation, and a positive circulation further up-estuary resulting in a local salinity maximum

zone (Valle-Levinson, 2010), referred to as salt plug estuaries (Wolanksi, 1986; Valle-Levinson, 2011). On the contrary, freshwater lens estuaries are found during rare events, when hypersaline riverine water follows a freshwater run-off with a certain time lag (Hosseini and Siadatmousavi, 2018).

When considering vertical density gradients, estuaries can be distinguished between (i) well-mixed during the entire tidal cycle (Nunes and Simpson, 1985), (ii) alternating between a well-mixed and a stratified state (strain-induced periodic stratified or SIPS, Simpson et al., 1990; Verspecht et al., 2009) as well as (iii) permanently stratified (Geyer, 1997). The latter may be distinguished additionally between strongly and weakly stratified. Simpson et al. (1990) found that the transition from one stage to the other can be described using a non-dimensional formulation of the along-estuary density gradient.

Earliest studies identified this density gradient as the major driver for estuarine circulation (Pritchard, 1952b, 1954b, 1956; Hansen and Rattray, 1965; Chatwin, 1976), motivating a more precise phrasing of this type of exchange flow as gravitational or buoyancy circulation. The existence of an along-channel density gradient results from the salinity difference between seawater and riverine water, typically decreasing from the mouth of the estuary when moving landward (Pritchard, 1954a).
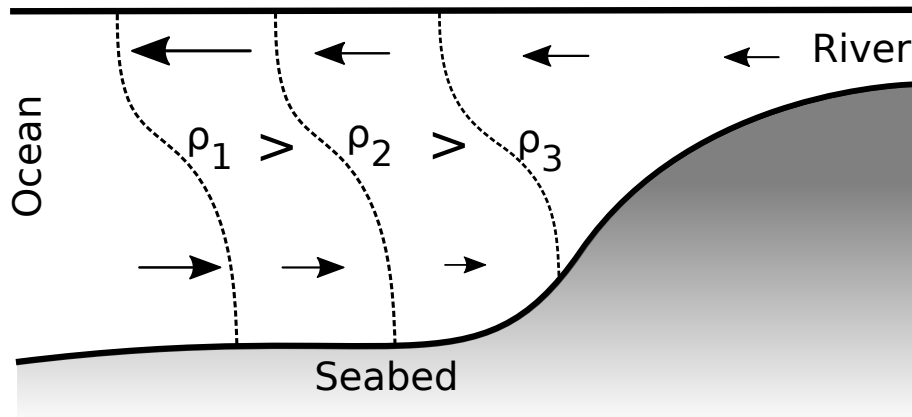
Figure 1: Sketch of an estuary with freshwater flux originating from river discharge. The direction of classical estuarine circulation, with near-bottom inflow and near-surface outflow, is depicted as arrows. The density ρ (isolines indicated as dashed lines) increases seaward and downward.

By using a vertically constant eddy viscosity for parameterization of turbulent momentum fluxes, Hansen and Rattray (1965) derived an analytical formulation for the resulting estuarine exchange flow in terms of vertically resolved profiles for the

along-estuary velocity component. They suggested that the gravitational circulation is proportional to the horizontal buoyancy gradient scaled by the turbulent viscosity. In practice this constant viscosity has been used as a tuning parameter (interpreting its value as an effective viscosity) to fit analytical models to observations, showing good results when calibrated carefully, e.g. by Geyer (1997) for two shallow estuaries in Cape Cod. A further approach in estimating the effective viscosity makes use of an algebraic parameterization depending on the tidal velocity amplitude and the horizontal buoyancy gradient, successfully developed by Ralston et al. (2008) for the Hudson River estuary. Because the analytical consideration of turbulence, in terms of eddy viscosity, turned out to be crucial when developing analytical theories for estuarine circulation, Burchard and Hetland (2010) used a depth-varying parabolic formulation for the eddy viscosity, motivated by the dependency of the size of turbulent eddies on the distance to the upper and lower boundaries (McGregor, 1972; Ianniello, 1979). Their analytical solution for the velocity showed more realistic properties, e.g. a logarithmic decrease of the current velocity near the bottom, compared to the Hansen and Rattray (1965) velocity profile. However, because Burchard and Hetland (2010) applied a no-stress boundary condition at the surface, an analytical solution for the wind-driven exchange flow based on a parabolic viscosity is still missing.

Studies analyzing the effects of wind forcing on estuarine circulation started with observations by Weisberg (1976) and Weisberg and Sturges (1976) in the Narragansett Bay, through comparisons of wind and near-bottom current velocities. Since then the importance of along-estuary wind straining in driving an estuarine exchange flow, in addition to the gravitational circulation, is highlighted in numerous studies (Geyer, 1997; Scully et al., 2005; Chen and Sanford, 2009; Purkiani et al., 2016). Contrary to the buoyancy gradient and the resulting gravitationally driven circulation, wind forcing may be highly variable (temporally and spatially) in magnitude as well as direction. Observations by Scully et al. (2005) in the York River estuary showed a strong correlation between the exchange flow and the longitudinal wind, with seaward wind increasing estuarine circulation (and stratification) and landward wind decreasing the exchange flow. They suggested that the residual vertical shear is enhanced by down-estuary wind stress while up-estuary wind causes the opposite and even reverses the estuarine exchange flow when strong enough. In order to quantify the importance of wind straining processes Monismith (1986) used the dimensionless system-wide Wedderburn number W, originally introduced by Thompson and Imberger (1980), when studying the upwelling response to wind stress in reservoirs. The Wedderburn number is defined as the ratio of wind stress and along-estuary density gradient, including geometrical properties of the estuary, with negative values representing either seaward wind forcing or a reversed buoy-

ancy gradient as found e.g. in inverse estuaries. Later Chen and Sanford (2009) used this estuary-wide number when studying the balance between wind straining and gravitational forcing using an idealized tidal estuary. Based on this Purkiani et al. (2016) defined the local Wedderburn number We by replacing the estuarine system-wide density gradient with the local density gradient, averaged over a cross-estuary transect. Using the example of a tidal channel in the Wadden Sea, they proved its usefulness by showing a high correlation between We and the strength of the exchange flow, when wind forcing is strong. However, it is still unclear if this correlation depends on other estuarine processes and how it may determine the sensitivity of an estuary to wind stress.

Besides gravitational forcing and wind forcing, tidal straining has been identified to contribute significantly to the residual exchange flow as observed e.g. by Stacey et al. (2001) in the San Francisco Bay and by Becherer et al. (2011) in the Wadden Sea. A reason for this process is found in a tidal asymmetry occurring between ebb and flood: because the velocity of a tidal current increases with the distance from the bottom, in the presence of a longitudinal buoyancy gradient less dense riverine water is sheared over denser water during ebb resulting in a stably stratified water column. Contrary this mechanism is inverted during flood with (dense) offshore
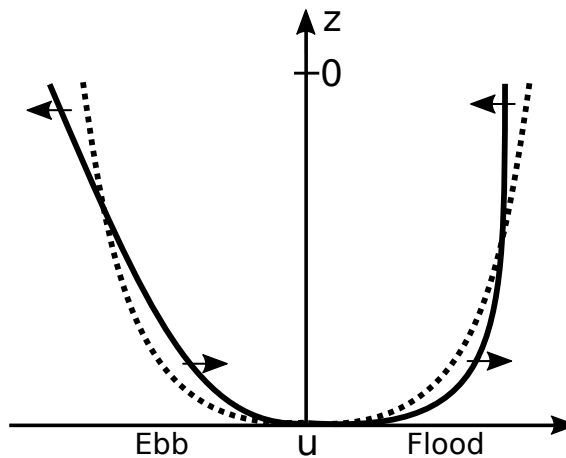
Figure 2: Depiction of the ebb-flood asymmetry caused by differential vertical mixing of momentum (based on Jay and Musiak, 1994). The resulting velocity profiles (solid lines) deviate from the semi-diurnal velocity structure (dashed lines) resulting in a near-bottom landward and a near-surface seaward residual flow.

water being sheared over onshore water reducing or even completely destroying the vertical stratification (van Aken, 1986; Linden and Simpson, 1988; Simpson et al., 1990). Since stratification is known to suppress turbulence (see e.g. Linden, 1979) a tidal-mixing asymmetry exists with vertical mixing being reduced during ebb and enhanced during flood, respectively. Consequently more momentum is transported downward to the near-bottom region during flood than during ebb (Fig. 2) resulting

in an additional residual near-bed current velocity (Jay and Musiak, 1994). This subtidal flow is found to have the same direction as the buoyancy-driven circulation (Burchard et al., 2011) and thus typically increasing classical estuarine circulation. Its contribution to the estuarine exchange flow turned out to be larger than the gravitational circulation in partially mixed estuaries (Burchard and Baumert, 1998; Stacey et al., 2008). Burchard and Hetland (2010) highlighted in an idealized study that tidal straining may even contribute to about two-thirds of the total circulation. This process, induced by tidally varying stratification, is strongly dependent on the non-dimensional buoyancy gradient (Simpson et al., 1990; Stacey et al., 2001). Formally phrased as horizontal gradient Richardson number (Monismith et al., 1996; Stacey, 1996; Stacey et al., 2001) it was later renamed Simpson number Si in honor of his important contributions to estuarine research (Stacey et al., 2010; Burchard et al., 2011). Using the Simpson number as a threshold the transition from well-mixed to SIPS state is found to take place at $Si = 8.8 \times 10^{-2}$ and between SIPS and permanently stratified at $Si = 8.4 \times 10^{-1}$ (Simpson et al., 1990). Later Verspecht et al. (2009) found that these threshold values depend on wind stress, while Burchard (2009) showed additional changes with respect to the relative tidal frequency and Earth rotation.

Other tidally induced effects result from a laterally varying bathymetry and its effect of differential advection as postulated by Smith (1976) and observed by e.g. Nunes and Simpson (1985) in terms of surface convergence during flood. The along-
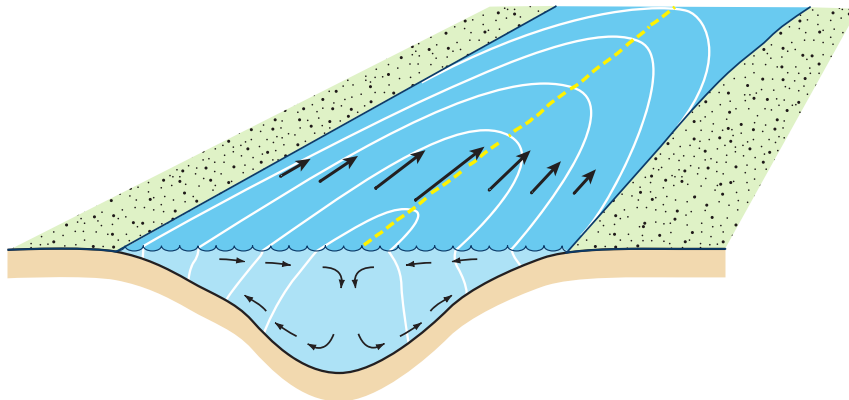
Figure 3: Schematic for lateral circulation induced by along-estuary differential advection. Higher salinities (white contour lines) are located in the center due to stronger along-channel velocities (black arrows), resulting in baroclinic-driven lateral exchange flows. Figure taken from MacCready and Geyer (2010).

channel tidal current velocity varies cross-sectionally due to different water depths with smallest values at the shoals and largest at the thalweg. This results in a lateral buoyancy gradient during flood with buoyancy in the center of the tidal channel

being weaker than at the edges and vice versa during ebb (Lerczak and Geyer, 2004), leading to a cross-sectional (or secondary) circulation. These circulation cells are convergent at the surface during flood (Nunes and Simpson, 1985) with the result that the larger along-estuary momentum is advected downward enhancing the up-estuary bottom currents during flood (flood-oriented transverse circulation, Burchard et al., 2011). During ebb the situation is different: the cross-sectional circulation is surface-divergent due to larger densities being at the shoals compared to the thalweg, advecting larger momentum from the center to the shoals leading to enhanced surface currents during ebb (ebb-oriented transverse circulation). This tidal asymmetry results in a residual flow which has the same direction as the gravitational circulation and therefore contributes additionally to classical estuarine circulation (Burchard et al., 2011). Another effect of a laterally varying bathymetry is a cross-channel varying turbulent mixing. Scully and Friedrichs (2007) concluded from observations in the York River estuary that turbulent mixing at the shallow areas of the cross-section (at the shoals) is constantly high while being periodic in the channel, resulting in a longitudinal circulation with landward flow at the shoals and seaward above the channel. In order to quantify mixing in estuaries different approaches have been suggested in the past. Aside from using the eddy diffusivity as a measure for tidal mixing (e.g Hansen and Rattray, 1965; Hetland and Geyer, 2004), a quantification in terms of the dissipation of salinity variance (Umlauf and Burchard, 2005) drew some attention recently. Wang et al. (2017) applied the latter in order to study volume-integrated mixing in the Hudson River estuary using a numerical model and the isohaline Total Exchange Flow framework (TEF, MacCready, 2011), for describing transports of volume and salt. Using TEF and a salinity variance budget MacCready et al. (2018) showed that the total system-wide mixing in an estuary can be estimated as the simple product of in- and outflow salinity as well as freshwater discharge when considering long-term averages. Based on this Burchard et al. (2018b) derived a more detailed formulation by allowing non-constancy of salinity and including the effect of storage of volume and salt.

Thus, the estuarine exchange flow and its related salt and volume fluxes are dependent on the amount of freshwater discharge, mixing and stratification, local tidal characteristics as well as the prevailing buoyancy gradient and wind stress. Note that apart from the mechanisms mentioned above estuarine circulation may be modulated by local topographic features such as curvature (Geyer, 1993; Chant, 2002; Becherer et al., 2015) or channel convergence (longitudinally changing cross-estuary area, Ianniello, 1979; Burchard et al., 2014; Geyer and Ralston, 2015). However, it turned out that especially the role wind plays in this complex estuarine dynamics needs further attention. That applies to a realistic analytical description of the wind-driven exchange flow and a deeper understanding of how the directionally vari-

able wind either supports or opposes the classical estuarine circulation. The latter is of particular interest when additionally considering wind-induced stratification and mixing in the presence of mechanisms related to tidal forcing. Moreover, still unclear is to what extent the various drivers affect the way an estuarine exchange flow responds if the wind forcing changes.

The aim of this study is to systematically evaluate the effect of wind straining on estuarine circulation in tidally energetic and weakly tidal estuaries. The major question is how up-estuary wind stress is related to the inversion of density-driven exchange flows and how the sensitivity of an estuary to wind stress can be quantified using a parameter describing an estuarine-system rather than the state of an estuary (which can be highly variable in time). Therefore, a new analytical stationary solution for wind- and buoyancy-driven estuarine circulation, including a parabolic parameterization for the eddy viscosity, is derived, motivating the existence and significance of a critical local Wedderburn number for the cancellation of estuarine circulation. By successively considering additional drivers of estuarine circulation the complexity of realistic estuaries is recreated, using state-of-the-art numerical models. These includes: (i) adding tidal oscillations and stratificational effects, (ii) adding effects of lateral circulation and (iii) adding the full complexity of realistic transient forcing of a real tidally energetic inlet and a real weakly tidal estuary.

The present study is structured as follows: First, conventions, definitions of non-dimensional parameters as well as basic equations are introduced in Section 2, followed by three chapters presenting the major results. These include the derivation of an idealized analytical solution for the subtidal along-estuary velocity profile in Section 3 based on a balance of pressure-gradient and friction and analysis of the resulting strength of the exchange flow in a non-dimensional parameter space depending on wind stress and density gradient. Building upon these findings various numerical studies with increasing complexity are performed in order to obtain a condition for inversion of estuarine circulation in the same parameter space. This is done in terms of a one-dimensional comparative study (Section 4.2) and a 2D cross-estuarine model studying the effect of wind stress on the estuarine exchange flow in the presence of lateral circulation (Section 4.3). In Section 4.4 the applicability of the theoretical findings for real tidally energetic inlets is tested for a realistic 3D model of a tidal inlet in the Wadden Sea. Finally the estuarine circulation of a highly variable weakly tidal estuary in the south-western Baltic Sea is investigated in Section 5 testing the generality of the results obtained in the former studies. The results are summarized and discussed in Section 6 and conclusions are drawn in Section 7 including an outlook with open questions. The appendix contains supplementary material.

2 Theoretical background

2.1 Basic equations and conventions

The conventions used in this study are defined as follows (Fig. 4): The Cartesian z-coordinate is looking upward, the x-axis points into the estuary (longitudinal direction) and the y-axis points cross-estuary (lateral direction). With this, the seabed is located at $z = -H$ and the free surface at $z = \eta$ defining the total water depth as $D = \eta + H$. *Up-estuary* or landward is defined in positive x-direction and *down-estuary* or seaward in negative direction.
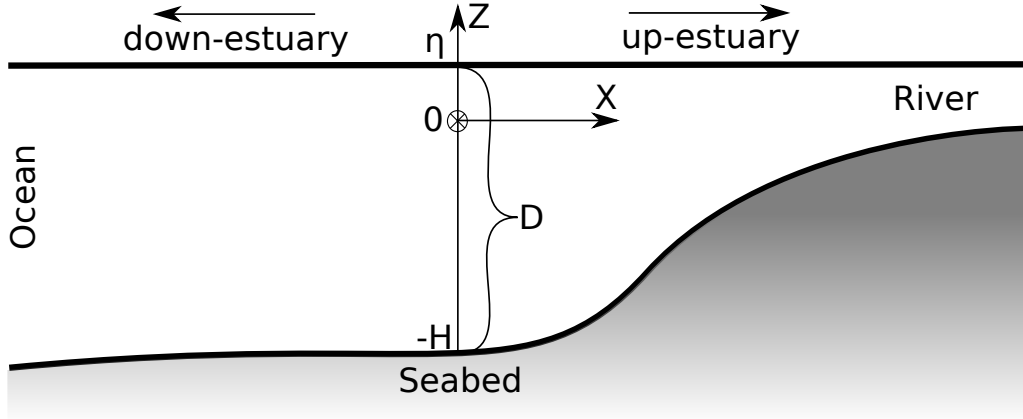
Figure 4: Conventions for the orientation of the coordinate system with the x-axis pointing up-estuary. The seabed is at $z = -H$ and the surface at $z = \eta$ resulting in a total water depth D.

Time average with the averaging period T is denoted by angular brackets $\langle \cdot \rangle$

$$\langle X \rangle (t_0) = \frac{1}{T} \int_{t_0 - T/2}^{t_0 + T/2} X(t) \, dt, \tag{1}$$

while depth-averaged quantities $\overline{\cdot}$ and volume-averaged $\widehat{\cdot}$ are defined as

$$\overline{X} = \frac{1}{D} \int_{-H}^{\eta} X(z) \, dz \quad \text{and} \quad \widehat{X} = \frac{1}{V} \int X(x, y, z) \, dV, \tag{2}$$

with the averaging volume V. An ensemble average with its weights p is denoted as

$$[X] = \sum_{i \epsilon I} p_i X_i. \tag{3}$$

Partial derivations are denoted by an abbreviation:

$$\frac{\partial}{\partial x} = \partial_x, \quad \frac{\partial}{\partial y} = \partial_y, \quad \frac{\partial}{\partial z} = \partial_z, \quad \frac{\partial}{\partial t} = \partial_t. \tag{4}$$

8

The time average operator $\langle \cdot \rangle$ and the ensemble average operator $[\cdot]$ fulfill the following properties:

i) Linearity: $\langle X + \alpha Y \rangle = \langle X \rangle + \alpha \langle Y \rangle$, with $\alpha = const.$

ii) Product average: $\langle X \langle Y \rangle \rangle = \langle X \rangle \langle Y \rangle$

iii) Commutativity with respect to the derivative operator: $\langle \partial_{\mathbf{x}} X \rangle = \partial_{\mathbf{x}} \langle X \rangle$

2.1.1 The momentum equation

The equation of motion for a fluid is described by the Navier-Stokes equation. The following assumptions are frequently used in physical oceanography:

- Reynolds average: A quantity is separable into an ensemble average and a deviation from it $X = [X] + X'$

- Boussinesq approximation: The changes of density are only important in the gravitational term

- shallow water assumption: The horizontal scales are much larger than the vertical scales $D/W \ll 1$

- incompressibility of water: The velocity field is divergence-free $\nabla \cdot \mathbf{u} = 0$

With this the governing set of momentum equations can be formulated as

$$\partial_t [u] + [\mathbf{u}] \cdot \nabla [u] - f [v] = -\frac{1}{\rho_0} \partial_x [p] + \partial_z \left(\nu \partial_z [u] - [u'w'] \right), \tag{5}$$

$$\partial_t [v] + [\mathbf{u}] \cdot \nabla [v] + f [u] = -\frac{1}{\rho_0} \partial_y [p] + \partial_z \left(\nu \partial_z [v] - [v'w'] \right), \tag{6}$$

$$\partial_z [p] = -g [\rho], \tag{7}$$

where $\mathbf{u} = (u, v, w)$ is the current velocity vector using the Cartesian framework defined above. The Coriolis parameter is defined as $f = 2\Omega \sin \varphi$, where φ denotes the local latitude and $\Omega = 2\pi/86\,154\,\mathrm{s}^{-1}$ is the angular frequency of the Earth. $\nu \approx 1.3 \times 10^{-6}\,\mathrm{m^2\,s^{-1}}$ is the molecular viscosity, $\rho_0 = 1025\,\mathrm{kg\,m^{-3}}$ is a constant reference mass density, $g = 9.81\,\mathrm{m\,s^{-2}}$ is the gravitational acceleration and $[u'w']$ and $[v'w']$ are vertical turbulent momentum fluxes. The hydrostatic equation (7) gives a formulation for the horizontal pressure gradient in (5) and (6) if integrated vertically and derived horizontally:

$$-\frac{1}{\rho_0} \nabla^h p = -g \nabla^h \eta - \frac{g}{\rho_0} \int_z^\eta \nabla^h \rho \, \mathrm{d}z' - \frac{1}{\rho_0} \nabla^h p_a. \tag{8}$$

with the horizontal derivation operator $\nabla^h = (\partial_x, \partial_y)$ and the atmospheric pressure $p_a = p(\eta)$. With this, the pressure gradient is composed of the barotropic pressure gradient, the baroclinic pressure gradient and the atmospheric pressure gradient (from left to right). In estuarine dynamics the baroclinic pressure gradient is especially of great relevance, because it suggests that a horizontal density gradient leads to a pressure gradient driving a current.

2.1.2   The viscosity

The vertical turbulent momentum fluxes are often expressed as

$$[u'w'] = -\nu_t \partial_z [u], \quad [v'w'] = -\nu_t \partial_z [v]. \tag{9}$$

This has the advantage that all turbulent properties are reduced to the turbulent viscosity ν_t, which is valid, since no assumptions are made for the properties of ν_t. ν_t can be calculated from information of the turbulent kinetic energy $k = \sum_i [u_i' u_i'] / 2$ and its dissipation rate ε:

$$\nu_t = c_\mu \frac{k^2}{\varepsilon}, \tag{10}$$

where c_μ is a stability function. The diffusion term in the momentum equation can then be rewritten as

$$\partial_z (\nu \partial_z [u] - [u'w']) = \partial_z (A_v \partial_z [u]), \tag{11}$$

with the vertical eddy viscosity $A_v = \nu + \nu_t$. Note that ν_t can be several orders of magnitude larger than the molecular viscosity ν. From now on the brackets $[\cdot]$ will be dropped for reasons of clarity, treating all quantities as ensemble-averaged. Boundary conditions for (11) are given by the the surface stress τ_x^s and the bottom stress τ_x^b

$$(A_v \partial_z u)|_{z=\eta} = \frac{\tau_x^s}{\rho_0} = u_*^s |u_*^s|, \tag{12}$$

$$(A_v \partial_z u)|_{z=-H} = \frac{\tau_x^b}{\rho_0} = u_*^b |u_*^b|, \tag{13}$$

with the surface friction velocity u_*^s and the bottom friction velocity u_*^b. The surface stress and the wind velocity are connected via a drag coefficient

$$\tau_x^s = C_D^w \rho_a U_{10} |\mathbf{U}_{10}|, \tag{14}$$

where $\mathbf{U}_{10} = (U_{10}, V_{10})$ is the wind velocity in $10\,\mathrm{m}$ height, ρ_a is the density of air and C_D^w is a drag coefficient (Large and Pond, 1981).

2.1.3 The density

The mass density of water ρ (denoted as density in the following) in the momentum balance is dependent on salinity s, temperature θ of the water as well as pressure. This is described by the equation of state:

$$\rho = \rho(s, \theta, p). \tag{15}$$

The internationally accepted standard is an empirical formula described as TEOS-10 (Thermodynamic Equation Of Seawater - 2010) standard. Fig. 5 shows the density of seawater at surface level for varying salinity and temperature calculated with the TEOS-10 formula. While the density varies only moderately in relation
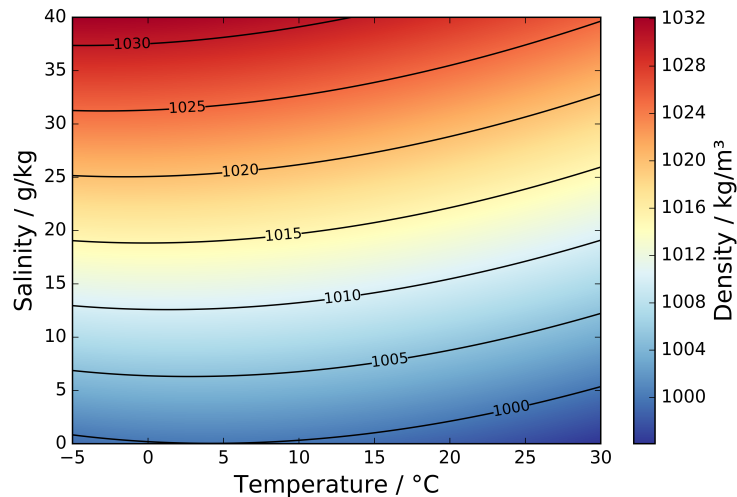
Figure 5: Density of seawater for varying temperature and salinity calculated with the TEOS-10 formula.

to temperature, an increase in salinity leads to a greater increase in density. Since the salinity in estuaries varies longitudinally from $s \approx 0\,\mathrm{g\,kg^{-1}}$ (freshwater) up to $s \approx 30\,\mathrm{g\,kg^{-1}}$ at the mouth (ocean water, depending on the study site) the density changes due to changes in salinity play an important role in estuarine dynamics. Because of that the density gradient and the salinity gradient are used analogously in this study. For analytical applications a linearized form of (15) is useful:

$$\frac{\rho}{\rho_0} = 1 - \delta\left(\theta - \theta_0\right) + \beta\left(s - s_0\right), \tag{16}$$

with the thermal expansion coefficient $\delta = \left(\partial_\theta \rho\right)_{S,p}/\rho_0$, the haline contraction coefficient $\beta = \left(\partial_s \rho\right)_{\theta,p}/\rho_0$ and the constant reference values ρ_0, θ_0 and s_0. Typical values for seawater applications are in the order of $\delta = 2 \times 10^{-4}\,\mathrm{K^{-1}}$ and $\beta = 7.4 \times 10^{-4}\,\mathrm{kg\,g^{-1}}$. By introducing the buoyancy $b = -g\left(\rho - \rho_0\right)/\rho_0$ the density

gradient in (8) can be expressed as

$$-\frac{g}{\rho_0}\partial_x\rho = \partial_x b \approx -g\beta\partial_x s. \tag{17}$$

The existence of a vertical density gradient $\partial_z\rho$ is defined as stratification. As a measure for the strength of stratification the potential energy anomaly (Simpson, 1981; Burchard and Hofmeister, 2008) is used:

$$\phi = \frac{1}{D}\int_{-H}^{\eta} gz\,(\bar{\rho}-\rho)\,\mathrm{d}z, \tag{18}$$

with the vertical mean density $\bar{\rho}$. The potential energy anomaly is equal to the energy needed to instantaneously homogenize the entire water column, with larger values corresponding to more stratification.

2.1.4 Scaling and non-dimensional parameters

Following the approach of Burchard (2009), the previous set of equations may be cast into a non-dimensional formulation using the following scalings:

$$\tilde{t} = t\omega, \qquad \tilde{z} = \frac{z}{H}, \quad \tilde{u} = \frac{u}{U_*},$$

$$\tilde{U}_r = \frac{U_r}{U_*}, \quad \tilde{z}_0^b = \frac{z_0^b}{H}, \quad \tilde{A}_v = \frac{A_v}{U_* H}, \tag{19}$$

where z_0^b denotes the bottom roughness length and U_* is the reference bottom friction velocity scale defined as

$$U_* = \left\langle \left(u_*^b \right)^2 \right\rangle^{1/2}. \tag{20}$$

Note that Burchard (2009) used a different velocity scale depending on tide- and wind-induced current speed scales. The bottom friction velocity in (20) can be calculated using the law of the wall (see e.g. Burchard et al., 2011):

$$C_D = \left(\frac{u_*^b}{U(t)} \right)^2 = \left(\frac{\kappa}{(1 + \tilde{z}_0^b)\ln\left(\frac{1}{\tilde{z}_0^b} + 1\right) - 1} \right)^2, \tag{21}$$

where $\kappa = 0.41$ denotes the van Karman constant. Based on this, the following essential non-dimensional parameters are defined as:

- Simpson number $\mathrm{Si} = \frac{\partial_x b H^2}{U_*^2}$, describing the balance between stratification, caused by density gradient forcing, and destratification due to vertical mixing (Stacey et al., 2010; Burchard et al., 2011)

- Non-dimensional wind stress $\mathrm{Ts} = \frac{u_*^s |u_*^s|}{U_*^2}$, ratio of surface momentum flux to momentum flux at the seabed stating the relative strength of wind stress to bottom stress (or tidal stress)

- local Wedderburn number $\mathrm{We} = \frac{u_*^s |u_*^s|}{\partial_x b H^2} = \mathrm{Ts/Si}$, measure for the competition between gravitational forcing and wind forcing in driving estuarine circulation (Purkiani et al., 2016)

- Unsteadiness number $\mathrm{Un} = \omega H / U_*$, relative tidal frequency (Burchard et al., 2011, 2013; Hosseini and Siadatmousavi, 2018)

2.2 The numerical models

2.2.1 GOTM

The General Ocean Turbulence Model GOTM (see Umlauf and Burchard, 2005) is a community wide, 1D water column model providing numerous turbulence closure schemes and stability functions. The source code of GOTM is open source (see http://www.gotm.net). The present studies make use of an algebraic second-moment closure scheme (Cheng et al., 2002) solving equations for the turbulent kinetic energy k and its dissipation rate ε.

2.2.2 GETM

The General Estuarine Transport Model GETM (Burchard and Bolding, 2002; Hofmeister et al., 2010) is a three-dimensional numerical model developed for studying coastal ocean processes and has been successfully applied in numerous studies (e.g. Holtermann et al., 2014; Gräwe et al., 2015; Gräwe et al., 2016). It solves the Reynolds-averaged Navier-Stokes equations under Boussinesq-approximation by using the finite volume approach in order to guarantee numerically full conservation of mass, energy and momentum. GETM makes use of GOTM for calculation of the vertical diffusivities and the equation of state is solved by using an implementation of the TEOS-10 framework. GETM is used for modeling exchange processes (Purkiani et al., 2016), dynamics of sediments (Sassi et al., 2015), particle tracking (Gräwe and Wolff, 2010) and bio-geo-chemistry (Schiele et al., 2015). Output parameters are 3D time series of salinity, temperature, velocities and sea surface height, among others. It uses state-of-the-art advection schemes of second and third order with minimal numerical mixing (Klingbeil et al., 2014). The vertical discretization is solved by using e.g. bottom following σ-coordinates, with the possibility of using a vertical adaption on the density gradient, minimizing the numerical error (Gräwe et al., 2015; Hofmeister et al., 2010). The model is, due to implementations of MPI (Message Passing Interface) and OpenMP (Open Multi-Processing), highly scalable and designed for use on supercomputers. The source code of GETM is open source (see http://www.getm.eu).

3 Drivers of estuarine circulation

3.1 Motivation

In order to investigate the bidirectional exchange flows in estuaries, simplified analytical theories have already proven their usefulness in earliest studies (e.g. Pritchard, 1956; Hansen and Rattray, 1965). While the latter identified the along-estuary density gradient, originating mainly from the salinity difference between riverine water and seawater, as the major driver for estuarine circulation, the role of wind is questioned and studied frequently in observations (e.g. Scully et al., 2005) and numerical simulations (e.g. Purkiani et al., 2016). As a result the basic mechanism of wind-driven circulation is understood in general: Along-estuary wind stress adds horizontal momentum at the surface, accelerating the upper layer of water in wind direction. This process drags water in up-wind direction leading to a tilted sea surface, inducing a barotropic pressure gradient and resulting in a near bottom current in down-wind direction and thus in a bidirectional exchange flow. In contrast to the density gradient wind forcing may be highly variable in time and is found to enhance and to counteract the classical estuarine circulation. While gravitational circulation has already been investigated analytically in numerous studies, including realistic parameterizations of vertical turbulence (Burchard and Hetland, 2010), a deeper analytical understanding of wind-driven velocity profiles is suggested here using a parabolic formulation of the eddy viscosity, laying the foundation for the subsequent studies.

This chapter is structured as follows: first, analytical solutions for the along-estuary velocity profile are derived using different parameterizations of vertical turbulence, leading to a new solution for wind-driven flows (Section 3.2), followed by an analytical formulation of the resulting strength of estuarine circulation depending on the density gradient, the residual flow velocity and the wind stress. The properties of the solutions, as well as the critical condition for cancellation of gravitational forcing due to wind stress, are studied in Section 3.3. Conclusions are drawn in Section 3.4. The results presented in this section are partially published in Lange and Burchard (2019).

3.2 Derivation of an analytical solution

The 1D water column equation of motion for the along-estuary velocity (5) can be written without non-linear terms and Coriolis force as:

$$\partial_t u - \partial_z \left(A_v \partial_z u \right) = -z \partial_x b - \frac{1}{\rho_0} \partial_x p^{ext}(t), \tag{22}$$

where (8) and (9) have been used. The buoyancy gradient $\partial_x b$ in (22) is assumed to be prescribed and constant and $\partial_x p^{ext}$ is an external barotropic pressure gradient function forced by tidal constituents. Decomposition of (22) into a tidal-mean and a tidally fluctuating component ($X = \langle X \rangle + X'$) followed by a tidal-average, (22) reads then as:

$$\partial_z \left(\langle A_v \rangle \partial_z \langle u \rangle \right) = z \partial_x b + \frac{1}{\rho_0} \partial_x \left\langle p^{ext} \right\rangle - \partial_z \left\langle A'_v \partial_z u' \right\rangle, \tag{23}$$

where $\langle X' \rangle = 0$ holds for tidally periodic flows and consequently the relation $\langle A_v \partial_z u \rangle = \langle A_v \rangle \partial_z \langle u \rangle + \langle A'_v \partial_z u' \rangle$ has been used. In (23), the newly appearing term $\partial_z \left\langle A'_v \partial_z u' \right\rangle$ describes the effect of the interaction between the tidally varying eddy viscosity and vertical velocity shear. This ESCO-term (eddy viscosity shear covariance, Dijkstra et al., 2017) is known to amplify density-driven exchange flows due to enhanced asymmetries between ebb and flood (Jay and Musiak, 1994). For simplicity the covariance-term is neglected in the following by assuming a tidally constant turbulent viscosity ($A'_v = 0$). This assumption will be dropped later in the numerical simulations (see Section 4). With this, (23) can be integrated from an arbitrary position in the water column to the zero mean sea surface to yield

$$\partial_z \langle u \rangle = \frac{\partial_x \left\langle p^{ext} \right\rangle}{\rho_0 \langle A_v \rangle} z + \frac{\partial_x b}{2 \langle A_v \rangle} z^2 + \frac{\langle u_*^s \mid u_*^s \mid \rangle}{\langle A_v \rangle}, \tag{24}$$

where (12) has been used at the surface. By calculating the depth-averaged velocity

$$\bar{u}(t) = \frac{1}{D} \int_{-H}^{\eta} u(z,t) \mathrm{d}z = U_r + U_t \cdot \sin(\omega t), \tag{25}$$

the pressure gradient term $\partial_x \left\langle p^{ext} \right\rangle$ is defined in way which guarantees that the tidal mean transport equals the residual transport, where U_r is the residual flow velocity, U_t is the tidal velocity amplitude and $\omega = 2\pi/T$ is the tidal frequency, with $T = 44\,714\,\mathrm{s}$ for the semi-diurnal tidal mode $\mathrm{M_2}$. Finally, after choosing a formulation for the eddy viscosity A_v in (24) and thus the parameterization of turbulence leads to an analytical solution for the along-estuary velocity profile. Here, the two approaches of i) a vertically constant viscosity and ii) a parabolic viscosity will be both used to derive a solution, respectively.

i) Constant eddy viscosity: By using the simplest approach of a vertically constant viscosity $\langle A_v \rangle = const.$ (assuming vertically homogeneous turbulence) and after integrating (24) vertically from the bottom $-H$ to position z in the water column, the classical Hansen and Rattray (1965) solution for the velocity profile in an estuary is obtained:

$$\langle u\left(\tilde{z}\right)\rangle = \underbrace{\frac{\partial_x b H^3}{48\left\langle A_v\right\rangle}\left(8\tilde{z}^3 + 9\tilde{z}^2 - 1\right)}_{u_g} + \underbrace{\frac{3}{2}U_r\left(1 - \tilde{z}^2\right)}_{u_r} \\ \underbrace{- \frac{\left\langle u_*^s \mid u_*^s \mid\right\rangle H}{4\left\langle A_v\right\rangle}\left(3\tilde{z}^2 + 4\tilde{z} + 1\right)}_{u_w}, \tag{26}$$

where the no-slip boundary condition $u(-H, t) = 0$ has been used. Note that the residual flow term u_r on the right hand side belongs to the class of Hagen-Poiseuille flows with a parabolic velocity profile obtained usually for laminar flows (see e.g. Mortensen et al., 2005).

ii) Parabolic eddy viscosity: More realistic scenarios of turbulent flows include a vertically varying eddy viscosity, with $\langle A_v \rangle = \langle A_v\left(z\right)\rangle$ scaling with the size of turbulent eddies. This motivates a parabolic formulation (see e.g. Burchard and Hetland, 2010), as the eddies grow with the distance to the upper and lower boundaries, if the water column is unstratified:

$$\left\langle A_v\left(z\right)\right\rangle = -\kappa U_*\left(z + z_0^b + H\right)\left(\frac{z}{H}\right), \tag{27}$$

where $\kappa = 0.41$ is the van Kàrmàn constant and U_* and z_0^b are the bottom friction velocity scale and bottom roughness as defined in Section 2, respectively. Insertion of (27) into (24) leads after vertical integration from the bottom to position z (Burchard and Hetland, 2010; Lange and Burchard, 2019) to:

$$\langle u(\tilde{z})\rangle = \underbrace{\frac{\partial_x b H^2}{2\kappa U_*}\left(\frac{\ln B\left(\tilde{z}\right)}{2C} - \left(\tilde{z} + 1\right)\right)}_{u_g} + \underbrace{U_r\frac{\ln B\left(\tilde{z}\right)}{C}}_{u_r} \\ \underbrace{- \frac{\left\langle u_*^s \mid u_*^s \mid\right\rangle}{\kappa U_*}\frac{1}{1 + \tilde{z}_0^b}\left(\ln\left(-\tilde{z}\right) + \frac{\ln B\left(\tilde{z}\right)}{C}\right)}_{u_w}, \tag{28}$$

with the integration constant

$$C = \int_{-1}^0 \ln B\left(\tilde{z}\right)\mathrm{d}\tilde{z} = \left(1 + z_0^b\right)\ln\left(\frac{1}{\tilde{z}_0^b} + 1\right) - 1 \tag{29}$$

and the dimensionless depth parameter $B(\tilde{z}) = (\tilde{z} + \tilde{z}_0^b + 1)/\tilde{z}_0^b$. Here, the no-slip boundary condition $u(-H, t) = 0$ as well as the surface and bottom stress as defined in (12) and (13) have been used, respectively. For simplicity the angular brackets will be dropped from now on, considering all quantities as tidally averaged.

The classical solution (26) and the solution with a more realistic turbulent viscosity (28) have in common that the resulting velocity profile is composed of a gravitational term including the effects of a horizontal density gradient u_g, a residual flow term u_r and a term driven by along-estuary wind u_w. Note that the latter is here newly derived for a parabolic eddy viscosity. Fig. 6 shows the velocity pro-
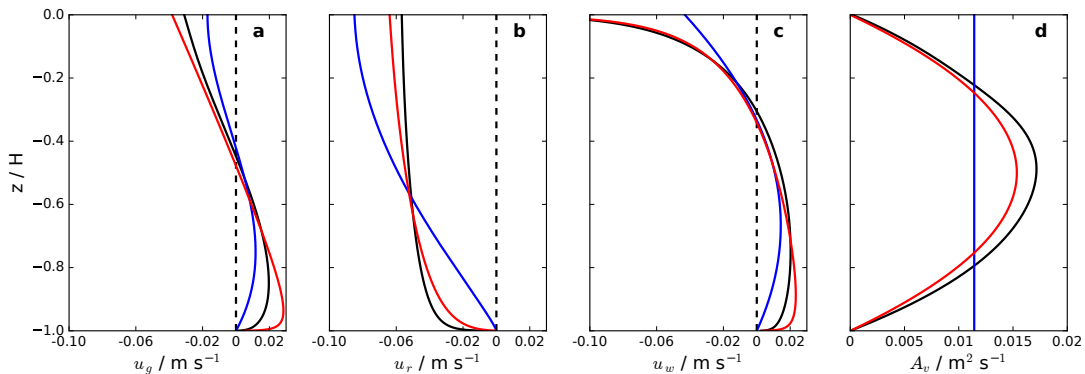

Figure 6: Comparison of analytical solutions for velocity profiles with constant (blue) and parabolic eddy viscosity (red) with results calculated by a numerical model (black), driven by a horizontal salinity gradient $\partial_x s = -1.5\,\mathrm{g\,kg^{-1}\,km^{-1}}$ (a), residual flow $U_r = -0.05\,\mathrm{m\,s^{-1}}$ (b) and down-estuary wind stress $\tau_x^s = -0.2\,\mathrm{Pa}$ (c). The underlying viscosity profiles for (c) are shown in (d).

files of (26) and (28) compared to solutions calculated with a numerical turbulence model (k-ε, second-moment closure) by using the General Ocean Turbulence Model GOTM (see Section 2.2.1 and Section 4 for details). The simulations were configured with a constant horizontal salinity gradient (a), residual flow velocity (b) and down-estuary wind stress (c). In order to compare the goodness of the analytical solutions with the numerical model for the stated assumptions the effect of stratification on vertical exchange is neglected for the moment. The Hansen and Rattray (1965) solution, shown in blue, is calculated by using the vertical mean of the tidally averaged eddy viscosity of the numerical solutions obtained with GOTM (see Fig. 6, d) $A_v = \overline{\langle A_{GOTM} \rangle}$. For (28) U_* is calculated according to (20) using the numerical bottom friction velocity $u_{*,GOTM}^b$. The analytical solutions both agree with the numerical results in a way that in the presence of a density gradient or down-estuary wind there is a two-layered flow structure with near-bottom water flowing up-estuary and near-surface water going down-estuary - the estuarine exchange flow. However, the analytical solution using the parabolic eddy viscosity profile describes the ver-

18

tical structure of the velocity in a more realistic way, especially for the wind-driven flow, and will therefore be analyzed in more detail in the following studies.

In order to reduce the number of essential state parameters a non-dimensional formulation of (28) is established by scaling the results with the bottom friction velocity scale U_*:

$$
\tilde{u}\left(\tilde{z}\right) = \underbrace{\frac{\mathrm{Si}}{2\kappa}\left(\frac{\ln B\left(\tilde{z}\right)}{2C} - \left(\tilde{z}+1\right)\right)}_{\tilde{u}_g} + \underbrace{\tilde{U}_r \frac{\ln B\left(\tilde{z}\right)}{C}}_{\tilde{u}_r}
$$

$$
\underbrace{-\mathrm{Ts}\frac{1}{\kappa\left(1+\tilde{z}_0^b\right)}\left(\ln(-\tilde{z}) + \frac{\ln B\left(\tilde{z}\right)}{C}\right)}_{\tilde{u}_w},
$$

(30)

where Si is the Simpson-number, Ts is the non-dimensional wind stress and $\tilde{U}_r$ is the dimensionless residual flow velocity as introduced in Section 2.1.4. Note that other velocity scales like the tidal velocity amplitude U_t or the surface friction velocity u_*^s are suitable as well for deriving a non-dimensional formulation, but by choosing U_* the Simpson number, known as an important parameter in estuarine dynamics, is already included in the results.

3.3 Properties of the analytical solution

The analytical solution for the non-dimensional velocity (30) consists of three terms representing the influence of a horizontal density gradient, residual flow and along-estuary wind stress on estuarine circulation. Profiles of these contributors as well as the resulting overall circulation $\tilde{u}$ are shown in Figure 7 for up- and down-estuary wind (Ts > 0 and Ts < 0) and no wind (Ts $= 0$) in combination with different Simpson numbers Si. The bottom roughness length of $\tilde{z}_0^b = 1.5 \times 10^{-4}$ and the residual flow velocity of $\tilde{U}_r = -0.1$ is kept constant for all results.

The newly derived wind straining profiles show the logarithmic *law of the wall* at the bottom and a strong logarithmic increase near the surface. Directly at the surface $z = 0$ the value of $\tilde{u}_w$ goes towards infinity because of the vanishing viscosity $A_v (z = 0) = 0$ in the analytical expression in (27). This could be avoided by using a viscosity profile with $A_v (z = 0) = |u_*^s| \kappa z_0^s$, with z_0^s representing the surface roughness length, but with this the integrals can not be solved analytically in closed form. Similar to the density-driven flow the wind-driven velocity profiles show a two-layered flow structure with down-estuary wind resulting in a layer of near-surface water flowing down-estuary and near-bottom water flowing up-estuary. For up-estuary wind the profile is identical but the sign of the wind-driven velocity profiles changes. In the down-estuary wind case (Ts < 0) the resulting overall estuarine circulation $\tilde{u}$ is more pronounced than without any wind, while up-estuary wind (Ts > 0) reduces or even reverses the net circulation direction.

To quantify the importance of wind stress and horizontal density gradient on the strength of the estuarine exchange flow through an estuarine cross-section a dimensionless circulation parameter $\tilde{I}$ is used:

$$\tilde{I} (\tilde{u}) = -\frac{4}{\langle A \rangle} \int_0^L \langle D(y) \rangle \int_{-1}^0 \langle \tilde{u}(y, z) \rangle \left(\tilde{z} + \frac{1}{2} \right) \mathrm{d}\tilde{z} \mathrm{d}y, \qquad (31)$$

with the cross-estuarine transect area $\langle A \rangle = \int_0^L \langle D(y) \rangle \, \mathrm{d}y$ and the width of the transect L. $\tilde{I}$ is defined in a way that a steplike exchange flow around mid-depth $\tilde{u} (-H... - H/2) = +k$ and $\tilde{u} (-H/2...0) = -k$ results in an overall value of $\tilde{I} (\tilde{u}) = k$. The definition of $\tilde{I}$ guarantees linearity in a way, that all contributions $\tilde{I}_i$ from $\tilde{u}_g, \tilde{u}_w, \tilde{u}_r$ sum up to the total $\tilde{I}$. Note that Equation (31) is a modified version of the integral of the depth-weighted scaled velocity originally proposed by Burchard et al. (2011), now taking lateral changes in water depth into account. The one-dimensional formulation is identical to a cross-section with constant water depth and reads as

$$\tilde{I} = -4 \int_{-1}^0 \langle \tilde{u} (\tilde{z}) \rangle \left(\tilde{z} + \frac{1}{2} \right) \mathrm{d}\tilde{z}. \qquad (32)$$
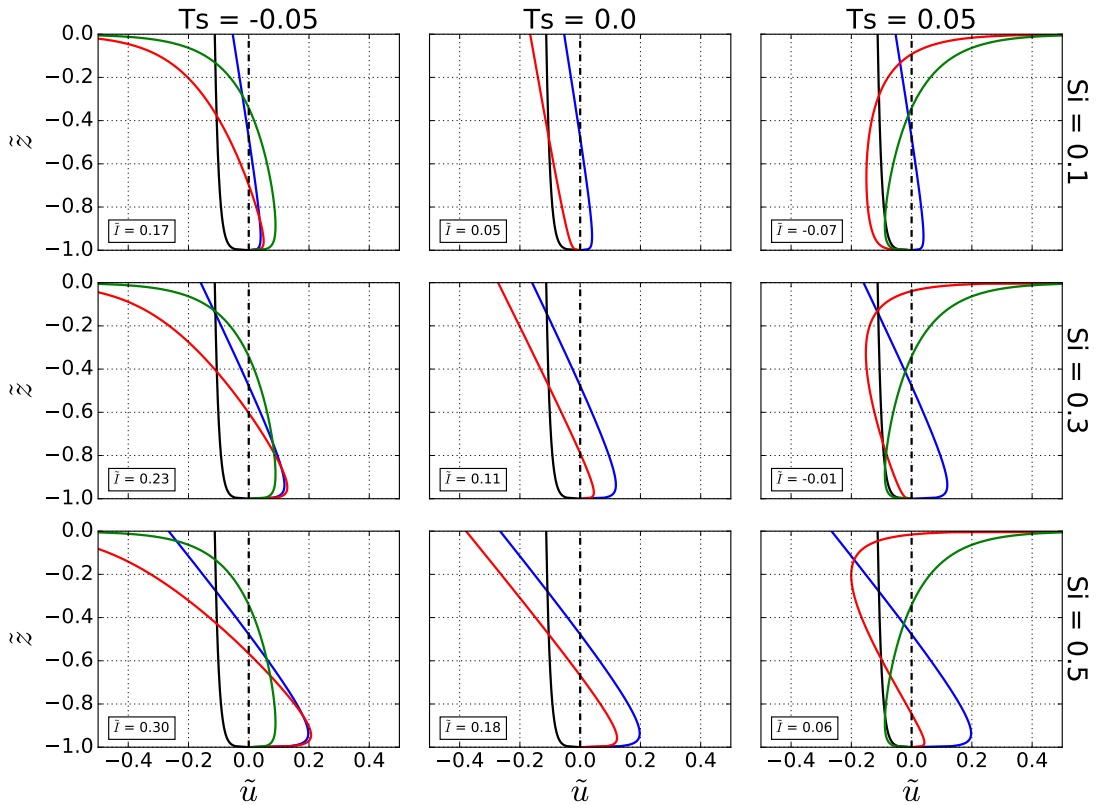
Figure 7: Analytical velocity profiles for varying Simpson number Si and non-dimensional wind stress Ts. Blue: density-driven component $\tilde{u}_g$; black: residual flow component with $\tilde{U}_r = -0.1$; green: wind-driven component $\tilde{u}_w$. The resulting overall profile $\tilde{u}$ is shown in red. Down-estuary wind (Ts < 0) amplifies gravitational circulation, while up-estuary wind (Ts > 0) antagonizes and even reverses the classical circulation direction when strong enough.

With this, three ranges can be distinguished: $\tilde{I} > 0$ describes classical estuarine circulation, $\tilde{I} < 0$ is a reversed circulation direction with inflow near the surface and outflow near the bottom and the special case $\tilde{I} = 0$ describes situations where wind- and density-driven estuarine circulation cancel each other out. An analytical expression for $\tilde{I}$ dependent on the various drivers of estuarine circulation is obtained after inserting (30) into (32):

$$\tilde{I} = \frac{\text{Si}}{2\kappa}\left(0.5\gamma + \frac{1}{3}\right) + \tilde{u}_r\gamma - \text{Ts}\frac{1+\gamma}{\kappa\left(1+\tilde{z}_0^b\right)}, \tag{33}$$

with $\gamma = 2\tilde{z}_0^b - 1/C$ which is only dependent on the non-dimensional bottom roughness length $\tilde{z}_0^b$. Fig. 8 shows the analytical solution (33) for varying Simpson number Si and non-dimensional wind stress Ts. Panel (a) and (b) is without residual flow velocity while (c) and (d) includes $\tilde{U}_r = -1$. For presentation of the results a constant

21

bottom roughness length of $\tilde{z}_0^b = 1.5 \times 10^{-4}$ is chosen. Classical circulation direction $\tilde{I} > 0$ is color-coded in red and inversed circulation $\tilde{I} < 0$ in blue, respectively. In the Si-Ts parameter space the isolines of $\tilde{I}$ are straight and parallel lines describing situations with wind and gravitational forcing leading to equal strength of estuarine circulation. As seen above, larger values of Si increases $\tilde{I}$ if Ts is kept constant and for Ts $= 0$ the circulation is purely density-driven. Note that negative values of Si may describe estuaries with an inversed density gradient as e.g. found in arid regions. For constant Simpson numbers down-estuary wind (Ts < 0) increases the value of $\tilde{I}$ while up-estuary wind decreases $\tilde{I}$ and inverses the circulation direction when strong enough. The critical condition for the transition $\tilde{I} = 0$ is highlighted in Fig. 8 as a bold line. For larger values of Si more up-estuary wind is needed to cancel the gravitational circulation. If a residual flow is added (c) the $\tilde{I} = 0$ isoline is shifted in a way that even more wind is needed for cancellation, where the dashed line shows the zero run-off situation in (a) for reference. The Si-Ts parameter space indicates that the slope of the $\tilde{I} = 0$ isoline is an important parameter since it describes how much wind is necessary for cancellation of the gravitational circulation.

An analytical formulation for the critical condition for inversion of estuarine circulation $\tilde{I} = 0$ is obtained by setting (33) equal to zero:

$$\text{Ts}_c = \text{Si} \cdot \text{We}_b + \alpha \cdot \tilde{U}_r \quad \Leftrightarrow \quad \text{We}_c = \text{We}_b + \frac{\alpha \cdot \tilde{U}_r}{\text{Si}}, \qquad (34)$$

with $\alpha = \gamma\kappa \left(1 + \tilde{z}_0^b\right) / (1 + \gamma)$ and $\text{We}_b = (0.5\gamma + 1/3)\left(1 + \tilde{z}_0^b\right) / (2 + 2\gamma)$. The critical non-dimensional wind stress Ts_c is the up-estuary wind needed to cancel the estuarine circulation forced by gravitational and residual flow forcing.

By introducing the local Wedderburn number We $= $ Ts/Si (see Section 2.1.4 for details), Eq. (34) reads as follows: if the ratio of wind-forcing to gravitational forcing becomes larger than the critical local Wedderburn number We_c the circulation reverses its direction. This critical condition is a threshold consisting of a constant value We_b and a second term representing the state of the estuary. We_b is hereby the inverse slope of the $\tilde{I} = 0$ isoline in the Ts-Si parameter space giving the sensitivity of an estuary to wind stress. The analytical value of the basic Wedderburn number is $\text{We}_b \approx 0.15$ depending slightly on the non-dimensional bottom roughness (see Fig. 9) stating that non-dimensional wind forcing has to be 15% of the non-dimensional gravitational forcing for inversion of estuarine circulation. In the Si-We parameter space in Fig. 8 this critical value is a constant value without discharge (b) and goes asymptotically against We_b for large Simpson numbers in (d) indicating that for larger density gradients the discharge loses the importance for the wind-driven estuarine dynamics.
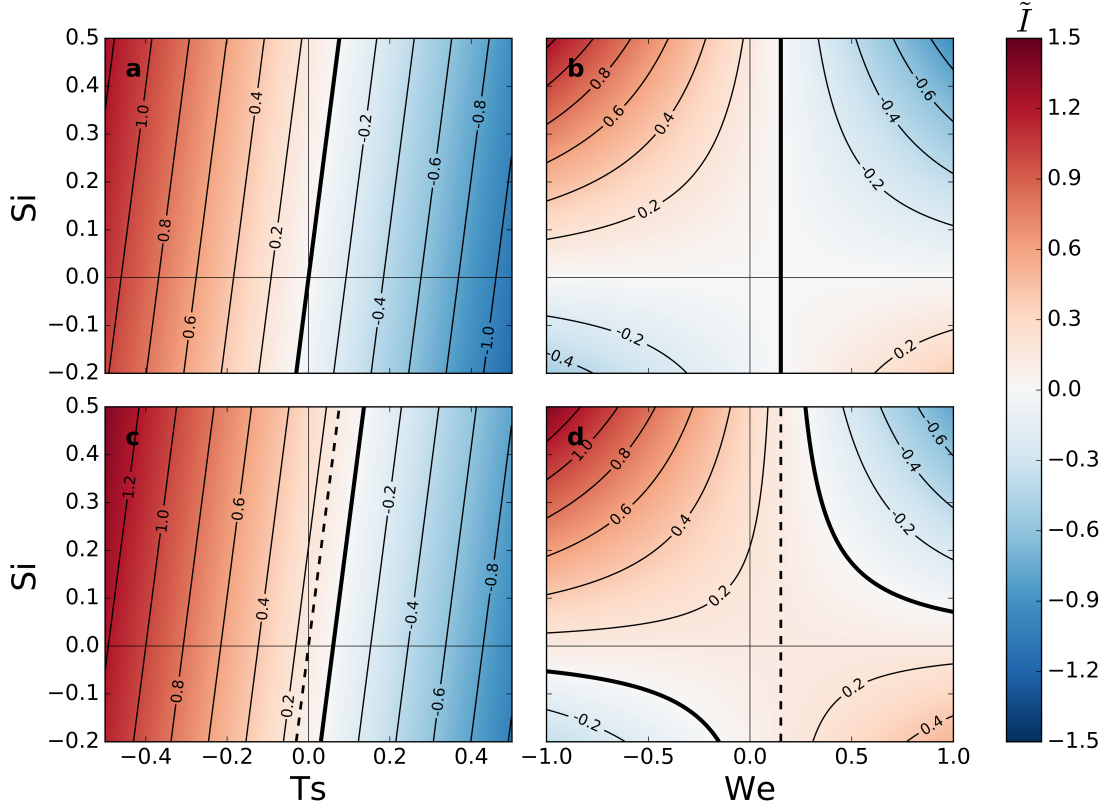
Figure 8: Analytical strength of the estuarine circulation $\tilde{I}$ for varying Simpson number Si, non-dimensional wind stress Ts and local Wedderburn number We. (a) and (b) without residual flow, (c) and (d) including $\tilde{U}_r = -1$. The bold line indicates the critical $\tilde{I} = 0$ condition for inversion of estuarine circulation. The dashed line represents the $\tilde{U}_r = 0$ case.

The definition of $\tilde{I}$ in (31) is originally motivated by two-layered exchange flows as can be found in purely density-driven and purely wind-driven estuarine circulation. Since in realistic estuaries three-layered flow structures can be observed (see Section 5.4.3) the analytical occurrence of this special type of flow is shown here for reference, by counting the number of zero-crossings in the Si-Ts and Si-We parameter space (see Fig. 10) based on the results in Fig. 8. A three-layered flow is possible in an area spanned by two straight lines crossing the origin of coordinates. The $\tilde{I} = 0$ isoline, shown in bold, is approximately the bisector of this cone. In the Si-We parameter space the condition for three-layered flow can be expressed in terms of constant Wedderburn numbers, which reads in the analytical parameter study as: $\text{We}_{min} \leq \text{We} \leq \text{We}_{max}$ with $\text{We}_{min} = 0.03$ the lower boundary and $\text{We}_{max} = 0.28$ the upper boundary.
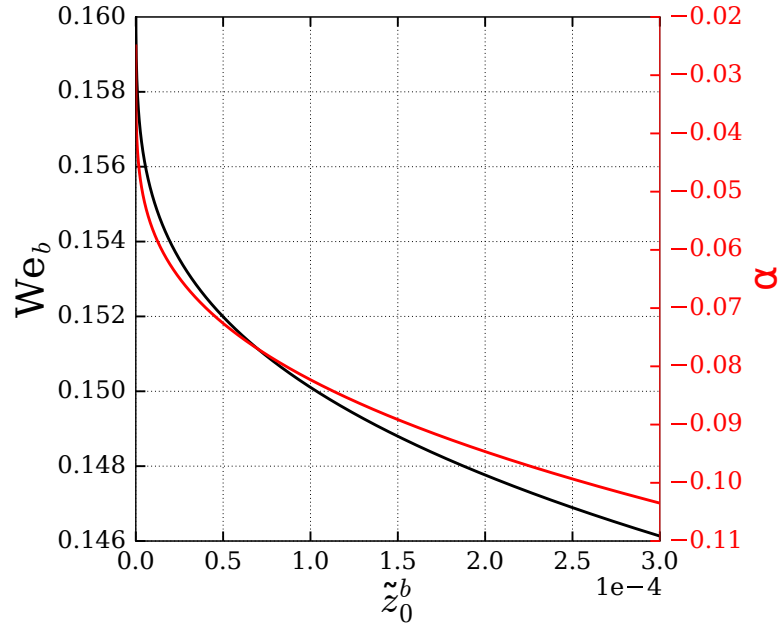
Figure 9: Dependency of the analytical basic Wedderburn number We_b in black and the parameter α in red on the non-dimensional bottom roughness $\tilde{z}_0^b$.
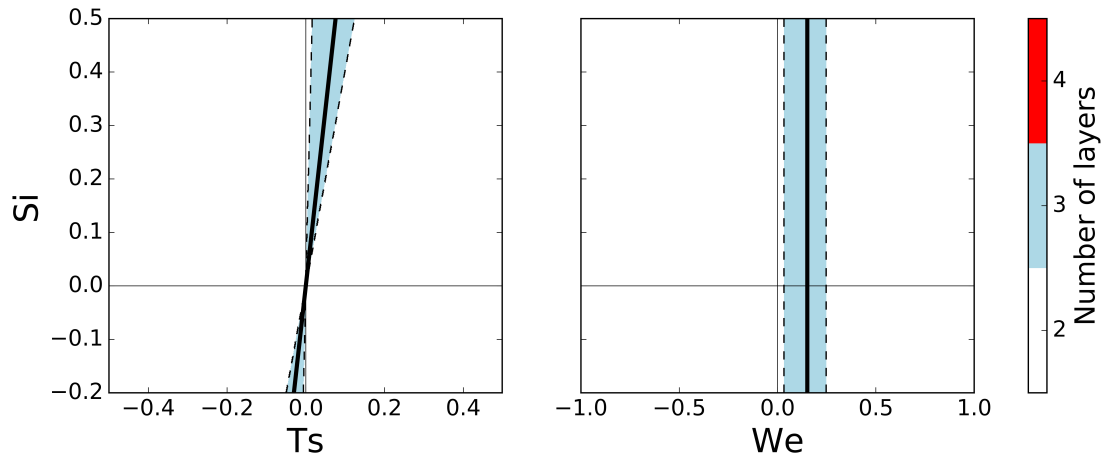

Figure 10: Number of velocity layers for varying Simpson number Si, non-dimensional wind stress Ts and local Wedderburn number We, calculated with an analytical solution for the velocity. The bold line represents the $\tilde{I} = 0$ condition for inversion of estuarine circulation.

3.4 Conclusions

Analytical solutions for exchange flows in estuaries have already been derived by Hansen and Rattray (1965), suggesting that the presence of along-channel wind and horizontal density gradient both drive estuarine circulation by creating opposing flow directions near-surface and near-bottom. While the classical solution assumes a vertically constant eddy viscosity the analytical solution with a parabolic viscosity profile results in more realistic profiles for the velocity components (Fig. 6) driven by gravitational forcing (u_g), residual flow forcing (u_r) and wind forcing (u_w), where an expression for the latter is here newly derived (Eq. (28)). Based on this, an analytical formulation for the strength of the exchange flow $\tilde{I}$ can be constructed, suggesting that non-dimensional density gradient forcing (described by the Simpson number Si) and non-dimensional wind forcing (described by Ts) compete in driving estuarine circulation (Eq. (33)). Down-estuary wind stress (Ts < 0) supports the classical density-driven estuarine circulation (Si > 0) leading to increased values of $\tilde{I} > 0$, while up-estuary wind (Ts > 0) is found to counteract and even to reverse the circulation direction when strong enough ($\tilde{I} < 0$). The critical condition $\tilde{I} = 0$, indicating scenarios with up-estuary wind and buoyancy gradient forcing canceling each other out, is fulfilled if the actual local Wedderburn number We (ratio of non-dimensional wind stress to non-dimensional horizontal buoyancy gradient) is larger than a threshold given by the critical Wedderburn number We_c. The results show that this critical value is composed of a constant value We_b which is independent of the state of the estuary (river discharge, wind stress and horizontal density gradient) and a term varying with the drivers (Eq. (34)). The analytical solution suggests a value of 0.15 for the basic Wedderburn number We_b, meaning that if up-estuary wind forcing is larger than 15% of the non-dimensional gravitational forcing the exchange flow reverses the direction, when the relative residual flow forcing is small. The results reveal that the overturning circulation can be fully described in a parameter space spanned by Simpson number Si and non-dimensional wind stress Ts.

Nevertheless, the analytical solution simplifies the estuarine dynamics significantly by e.g. neglecting stratification due to prescribing a constant parabolic eddy viscosity and setting its tidal variation to zero ($A'_v = 0$). By doing so its feedback on the exchange flow is not included in the solution and thus the ESCO-driven circulation (Dijkstra et al., 2017) as well as tidal straining (Jay and Musiak, 1994) is neglected, besides additional 2D and 3D processes. However, the analytical solution is useful by proposing the existence of We_b as a coefficient which is independent on the state of an estuary but rather describes the sensitivity of an estuary to wind stress itself, allowing the comparison and classification of different estuaries in the following.

4 Numerical Simulations

4.1 Motivation

The analytical solutions derived in the previous Section 3 motivate the study of the strength of the estuarine circulation $\tilde{I}$ in a parameter space spanned by the Simpson number Si and the non-dimensional wind stress Ts in order to obtain the sensitivity of the exchange flow to wind in terms of the basic Wedderburn number We_b. The present section aims to study the variability of this parameter when stepwise including more realistic dynamical processes than in the analytical solution. These tidal dynamics are known to drive additional exchange flows, primary due to asymmetries between ebb and flood. The latter is caused e.g. by varying stratification and mixing during the tidal cycle (Simpson et al., 1990; Jay and Musiak, 1994) when considering vertical processes. If in addition a laterally varying bathymetry is taken into consideration, secondary circulations occur, e.g. due to differential advection (Lerczak and Geyer, 2004), enhancing the classical circulation even further and opposing an inversion of the circulation direction by landward wind. A realistic up- and down-estuary wind straining also includes the induced stratification and mixing, aside from the forcing of the estuarine exchange flow (Scully et al., 2005).

These effects are included here by applying numerical models with increasing complexity: Using a numerical 1D turbulence model the Si-Ts parameter space is investigated, now including the tidal dynamics of a varying stratification and enhanced classical circulation in Section 4.2. This is subsequently repeated with varying 2D estuarine cross-sections, now additionally considering lateral effects (Section 4.3). The findings are applied to a 3D realistic model of a tidal inlet including the full dynamic of the driving forces in Section 4.4 followed by a summary of the main conclusions. The results presented in this section are partially published in Lange and Burchard (2019).

4.2 1D numerical simulations

4.2.1 The Si-Ts parameter space

The non-dimensional strength of the estuarine exchange flow $\tilde{I}$ (Eq. 31) in the Si-Ts and Si-We parameter space, as introduced in Section 3.3, is now calculated with more realistic velocity profiles obtained by using the one-dimensional water column model GOTM (k-ε model with algebraic second-moment closure, see Section 2.2.1 for details) instead of the analytical solution. As free parameters the horizontal salinity gradient $\partial_x s$ and the along-estuary wind stress τ_x^s were varied. The salinity gradient is, similar to the buoyancy gradient in the analytical solution, constant in time and space, but now additionally a buoyancy equation is solved considering feedback from an evolving stratification on the viscosity.

By prescribing the Simpson number Si^0 and the non-dimensional wind stress Ts^0, the corresponding salinity gradient $\partial_x s$ and surface stress τ_x^s are chosen as:

$$\frac{\tau_x^s}{\rho_0} = \text{Ts}^0 \cdot \left(U_*^0\right)^2 \quad ; \quad \partial_x s = -\frac{\text{Si}^0 \cdot (U_*^0)^2}{H^2 g \beta}, \tag{35}$$

where (17) has been used with the constant haline contraction coefficient $\beta = 7.4 \times 10^{-4}\,\text{kg}\,\text{g}^{-1}$. Here, the non-dimensional parameters were varied over a range of $\text{Ts}^0 = [-0.5 \ldots 0.5]$ and $\text{Si}^0 = [-0.2 \ldots 0.5]$ in steps of 0.01. The friction velocity scale U_*^0 is calculated by using the prescribed tidal velocity amplitude U_t and Eq. (21). Contrary to the analytical value of U_*^0, calculated with help of (21), the realistic bottom friction velocity scale is now dependent on wind stress, horizontal density gradient and residual flow velocity. Due to this, a rescaling of the prescribed parameters (superscript 0) with the actual tidal mean friction velocity, calculated by the numerical model, is necessary:

$$\text{Ts} = \text{Ts}^0 \cdot \left(\frac{U_*^0}{U_*}\right)^2 \quad ; \quad \text{Si} = \text{Si}^0 \cdot \left(\frac{U_*^0}{U_*}\right)^2 \quad ; \quad \text{Un} = \text{Un}^0 \cdot \frac{U_*^0}{U_*}. \tag{36}$$

A semi-diurnal M_2 tide with a tidal velocity amplitude of $U_t = 1.0\,\text{m}\,\text{s}^{-1}$ and a constant water depth of $H = 10\,\text{m}$ is prescribed for all simulations, which corresponds to an Unsteadiness number of $\text{Un}^0 = 0.04$. The resulting exchange flow $\tilde{I}$ is shown in Figure 11 in the Si-Ts and the Si-We parameter space for classical and reversed circulation in red and blue, respectively. The upper panels (a,b) show results without residual flow, the lower panels (c,d) include an additional $\tilde{U}_r = -1$. The bold line represents the critical condition $\tilde{I} = 0$ for an inversion of the estuarine circulation, which is additionally shown as a dashed line in (c) and (d) for $\tilde{U}_r = 0$ for reference. In good agreement with the analytical solution the isolines of $\tilde{I}$ are largely in
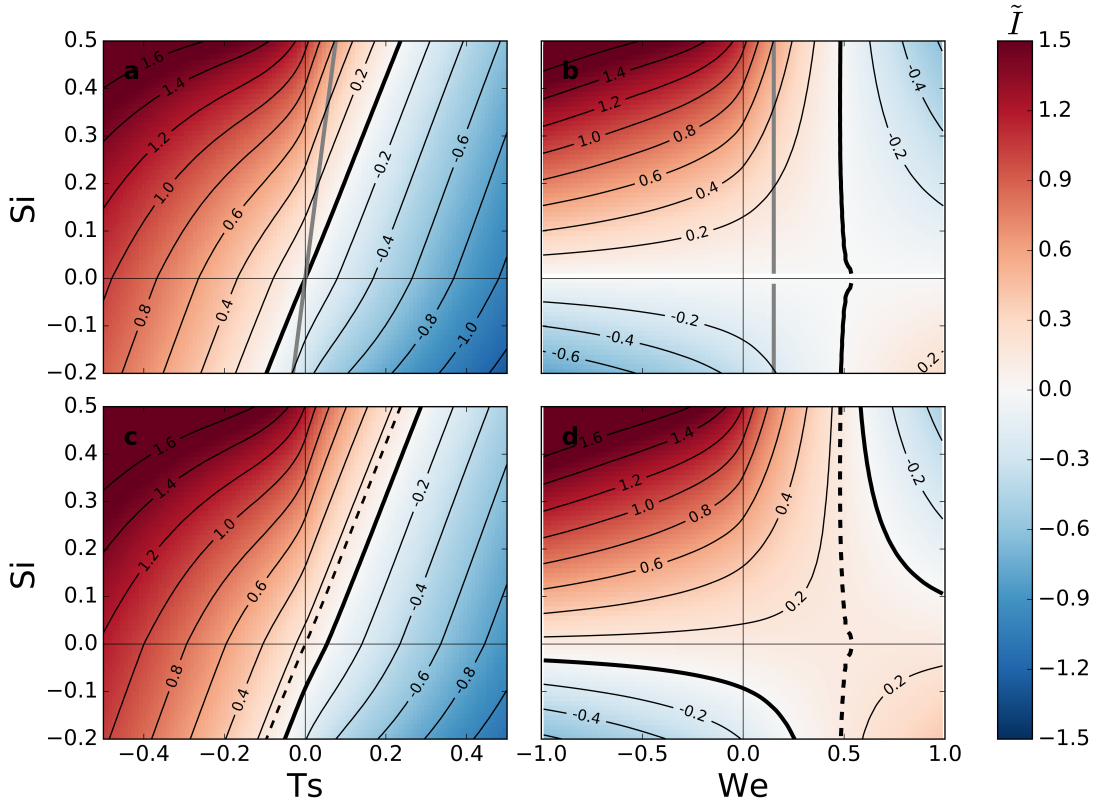
Figure 11: Strength of estuarine circulation $\tilde{I}$ for varying forcing parameters (defined as in Fig. 8), calculated with a 1D numerical model. The gray line indicates the analytical condition for $\tilde{I} = 0$.

straight and parallel lines for varying Si and Ts. Deviating from the results in (30) $\tilde{I}$ becomes more non-linear for stronger down-estuary winds (Ts < 0). If residual flow is included (c) the $\tilde{I} = 0$ isoline is shifted in a way that more wind is needed to invert the circulation, but without changing the slope of the line as predicted by the analytical solution. The numerical results show a smaller slope than in the analytical case indicating a larger basic Wedderburn number We_b. This is additionally described in the Si-We parameter space, where the $\tilde{I} = 0$ isoline in (b) approximates a straight, vertical line with a value of $\text{We}_c = \text{We}_b = 0.46$. The gray line in (a) and (b) is the analytical $\tilde{I} = 0$ solution for comparison. To study how the larger value of We_b is connected to the newly considered tidal dynamics, the simulations without residual flow were repeated with different Unsteadiness numbers. Figure 12 indicates that for small Un (large tidal velocity amplitude) the basic Wedderburn number is about 0.45 which decreases with larger Un up to the approximate value of 0.15 of the analytical case without tidal dynamics. This suggests that in tidally energetic estuaries, with tidal straining increasing the value of We_b, three times more wind is needed than in non-tidal estuaries to invert the estuarine circulation. This
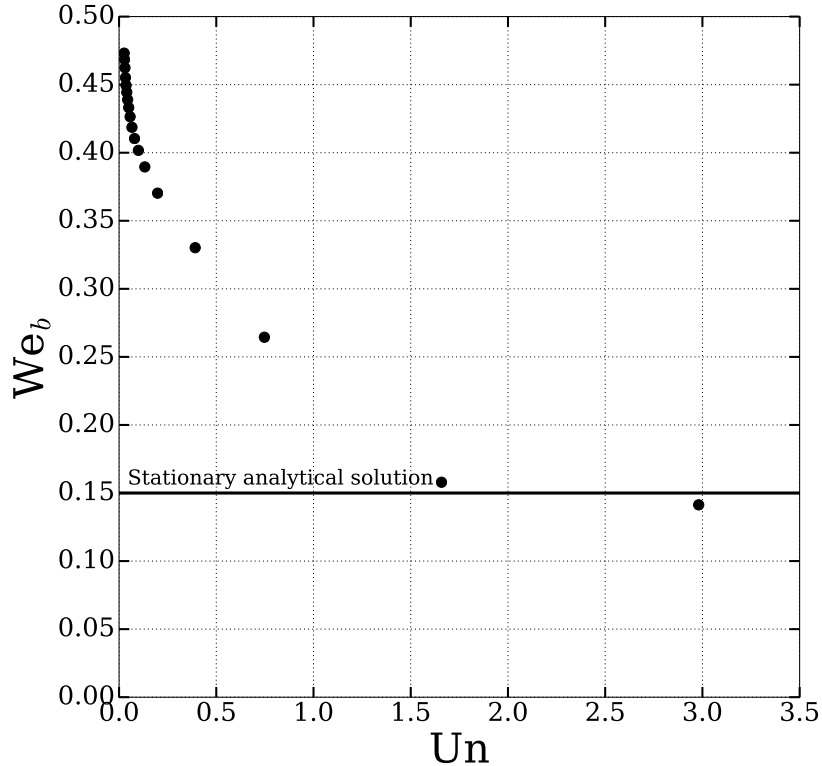
Figure 12: Basic Wedderburn number We_b for varying Unsteadiness numbers Un based on numerical model results. Small values of Un (larger tidal velocity amplitudes) results in a critical condition of about $We_b \approx 0.45$ for inversion of estuarine circulation. The analytical solution of $We_b \approx 0.15$ is the limiting case for large Unsteadiness numbers.

can be explained as follows: Within a tidal cycle stratification is pronounced during ebb, where low saline water is transported above high saline water, while during flood mixing is enhanced. Because stratification suppresses turbulence leading to a smaller eddy viscosity, an asymmetry in the viscosity profile exists during the ebb-flood tidal cycle, with the effect, that the ESCO term $\langle A'_v \partial_z u' \rangle$ in (23) does not vanish but drives estuarine circulation in a way that density-driven exchange flows are amplified. The strong amplification of gravitational exchange flows in the presence of tides agrees with findings which suggest that tidal straining contributes to about 2/3 to classical estuarine circulation (Burchard and Hetland, 2010).

4.2.2 Stratification

To study how stratification changes for varying wind stress and density gradient the tidally averaged non-dimensional potential energy anomaly $\left\langle \tilde{\phi} \right\rangle$ (see Section 2.1.3) is shown in Figure 13 in the Si-Ts parameter space for the data presented in Figure 11a (without residual flow velocity). Here, $\left\langle \tilde{\phi} \right\rangle$ is a measure for the stratification in the water column with increasing values meaning increased stratification and vice versa. The isolines of constant $\left\langle \tilde{\phi} \right\rangle$ are almost straight lines (except for a transition range)
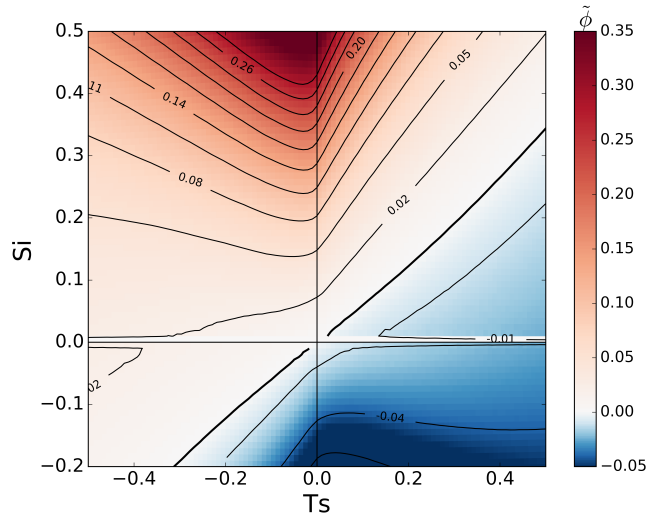

Figure 13: Non-dimensional potential energy anomaly $\left\langle \tilde{\phi} \right\rangle$ for varying Simpson number Si and non-dimensional wind stress Ts calculated from numerical results used in Fig. 11a (without residual flow velocity). Up-estuary wind (Ts > 0) decreases stratification stronger than down-estuary wind. For a density gradient smaller than Si = 0.1 down-estuary wind stratifies the water column. The bold line indicates transition to unstable stratification.

whereby the slope $\partial_{\mathrm{Ts}} \left\langle \tilde{\phi} \right\rangle$ is dependent on the direction of the wind stress. Note that the results are point symmetrically with respect to the coordinate origin, with the exception of a change of sign. For constant Ts the stratification increases with increasing Simpson number. Increasing up-estuary wind (Ts > 0) destratifies the water column for constant values of Si which becomes unstably stratified $\left(\left\langle \tilde{\phi} \right\rangle < 0 \right)$ for We > 1.3.

For down-estuary wind (Ts < 0) three cases can be distinguished:

- Si > 0.1 : wind stress stratifies for values up to Ts ≈ −0.25 and starts to decrease stratification if stronger

- Si < 0.1 : wind increases stratification

- Si ≈ 0.1 : a balance between wind induced mixing and wind straining induced stratification exists.

The changes in stratification for up- and down-estuary wind stress are asymmetric, with up-estuary wind causing a stronger decrease in stratification than down-estuary wind: For landward wind the wind straining of the buoyancy field shearing dense water over less dense water as well as the additional wind mixing reduce stratification, such that a small increase in wind speed can cause a large decrease in $\langle\tilde{\phi}\rangle$. In contrast, for down-estuary wind, stratifying wind straining and de-stratifying wind mixing have opposite effects, such that the decrease in stratification with increased wind speed is more moderate.

For weak buoyancy gradient forcing (Si < 0.1), the situation is different: stratification is steadily increasing with wind straining Ts, in the sense that for stronger down-estuary winds stratification is still increasing. This can be explained in such a way that for small Si vertical mixing is already strong (due to weak stratification) and additional wind mixing does not have a strong effect on $\langle\tilde{\phi}\rangle$.

4.2.3 Three-layered flow

As predicted by the analytical solution (30) exchange flow profiles with more than two layers can result from the interaction between gravitational forcing and wind forcing. Figure 14 shows the number of velocity layers obtained by counting the zero-crossings in the numerical velocity profiles used in Figure 11a. In the Si-Ts parameter space (without residual flow) exists an area of three-layered flow spanned by two straight lines and $\tilde{I} = 0$ as angle bisector, similar to the analytical results in Section 3.3. The lower and the upper limit of the three-layered flow can be represented as local Wedderburn numbers marking the transition of the estuarine circulation from density-driven to wind-driven flow, which are $We_{min} = 0.08$ and $We_{max} = 0.71$ in the actual case. With this, the estuarine circulation can be divided into five flow types, where the stated boundaries apply to the zero residual flow case:

- Type I, We < 0: classical density-driven estuarine circulation enhanced by wind straining

- Type II, $0 < We < We_{min}$: classical density-driven estuarine circulation

- Type III, $We_{min} < We < \tilde{I} = 0$: classical estuarine circulation plus third layer due to inverse wind straining

- Type IV, $\tilde{I} = 0 < We < We_{max}$: inverse wind-driven estuarine circulation plus third layer due to gravitational forcing

- Type V, $We > We_{max}$: inverse wind-driven estuarine circulation

An overview of the velocity profiles for the different flow types can be found in Figure 14.
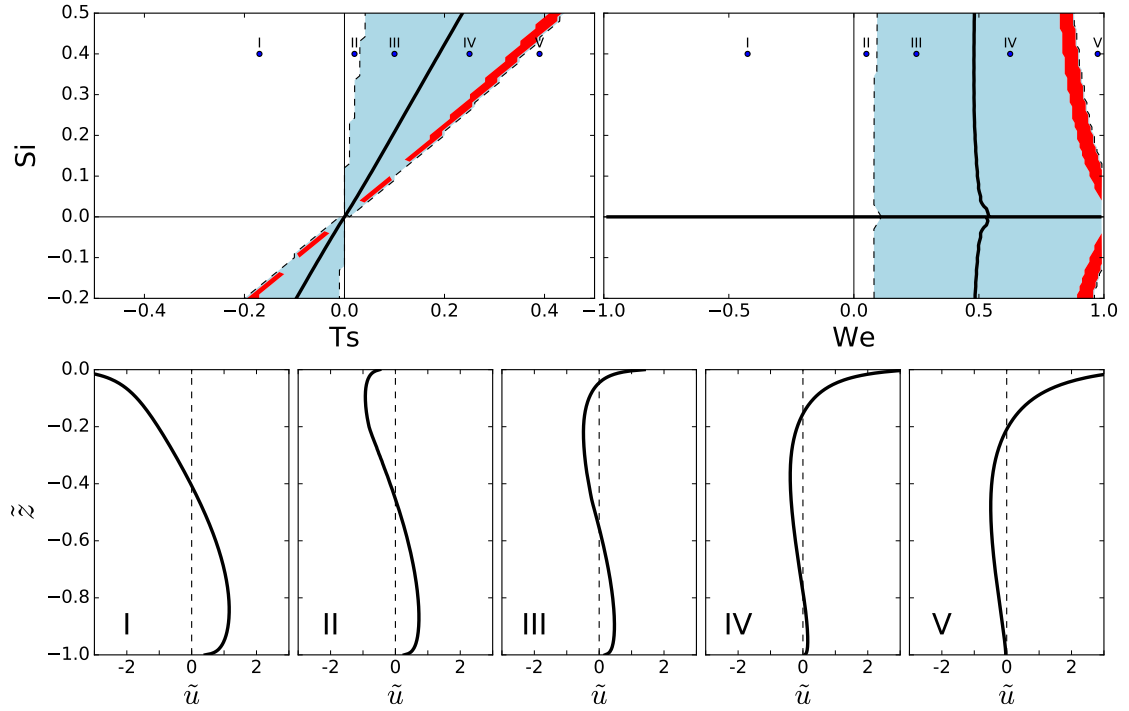
Figure 14: Top: Number of flow layers for varying Simpson number Si, non-dimensional wind stress Ts and local Wedderburn number We for data shown in Fig. 11a, with two-layered flow in white and three-layered flow in blue. Rare four-layered flow is shown in red. The black line is the $\tilde{I} = 0$ isoline for inversion of estuarine circulation. Bottom: Five flow classes can be distinguished showing the transition from gravitational circulation supported by wind (I) to wind dominated reversed circulation (V). Velocity profiles are taken from situations depicted in the upper panels.

4.3 Numerical 2D slice model

The numerical results in Section 4.2 are a generalization of the findings in Section 3.2 in terms of stratification and the derived effects of tidal straining but represent only the special cases of 1D scenarios or an estuarine transect with flat bottom. Here the influence of a laterally varying water depth and the resulting enhanced exchange flow on the basic Wedderburn number We_b is studied. In addition to vertical stratification and its feedback on turbulent viscosity, now lateral changes in buoyancy are considered by numerically solving a 2D buoyancy equation in combination with varying cross-sectional water depths. A non-uniform cross-section is known to amplify estuarine circulation due to a pronounced flood-ebb asymmetry (Lerczak and Geyer, 2004) in viscosity (see Figure 15) and vertical velocity shear resulting in an increased ESCO (Burchard and Schuttelaars, 2012). The reasons for this are lateral circulations induced by a lateral buoyancy gradient $\partial_y b$ caused by varying current velocities at the center and the banks. Comparable numerical studies with varying lateral bathymetry and its feedback on the exchange flow have been applied by e.g. Burchard et al. (2011), Burchard and Schuttelaars (2012) and Schulz et al. (2015). The bathymetry in this study is calculated by using
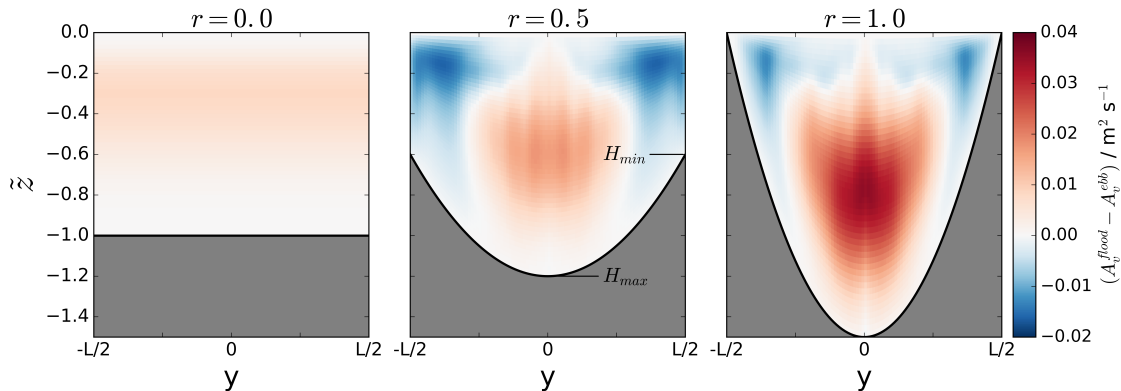
Figure 15: Difference in eddy viscosity A_v for fully developed flood and ebb for varying bathymetries. Cross-section area, tidal velocity amplitude $U_t = 1.0\,\mathrm{m\,s^{-1}}$ and Simpson number of Si = 0.25 are kept constant. Increasing steepness $r = 1 - H_{min}/H_{max}$ of the estuarine transect amplifies flood-ebb asymmetry of A_v. H_{min} and H_{max} denote the water depth at the shoals and at the center of the channel, respectively.

$$H(y) = \frac{3\bar{H}}{3-r}\left(1 - \left(\frac{y - 0.5L}{0.5L}\right)^2 \cdot r\right), \tag{37}$$

where the ratio $r = 1 - H_{min}/H_{max}$ is a parameter describing the steepness of the transect with H_{min} and H_{max} being the depth at the banks and at the center, respectively (see Fig. 15). Note that the special case $r = 0$ represents a flat bottom,

while $r = 1$ is a bathymetry with maximum steepness in this study. The water depth in Eq. (37) is defined in a way, that guarantees an equal cross-section area through all simulations by prescribing equal mean water depth $\bar{H}$ and transect length L. Here $\bar{H} = 10\,\text{m}$ and $L = 1000\,\text{m}$ is used for all simulations. The 2D cross-estuarine simulations were carried out by using the General Estuarine Transport Model (GETM, see Section 2.2.2 for details) which makes use of the same turbulence closure model applied in Section 4.2. Similar to the 1D GOTM simulations the longitudinal salinity gradient $\partial_x s$ and wind stress τ_x^s are prescribed and a tidal velocity amplitude of $U_t = 1.0\,\text{m}\,\text{s}^{-1}$ is used $\left(\text{representing } \text{Un}^0 = 0.04\right)$. The residual flow velocity $\tilde{U}_r = 0$ is kept constant. The resulting tidal mean velocity (left) and
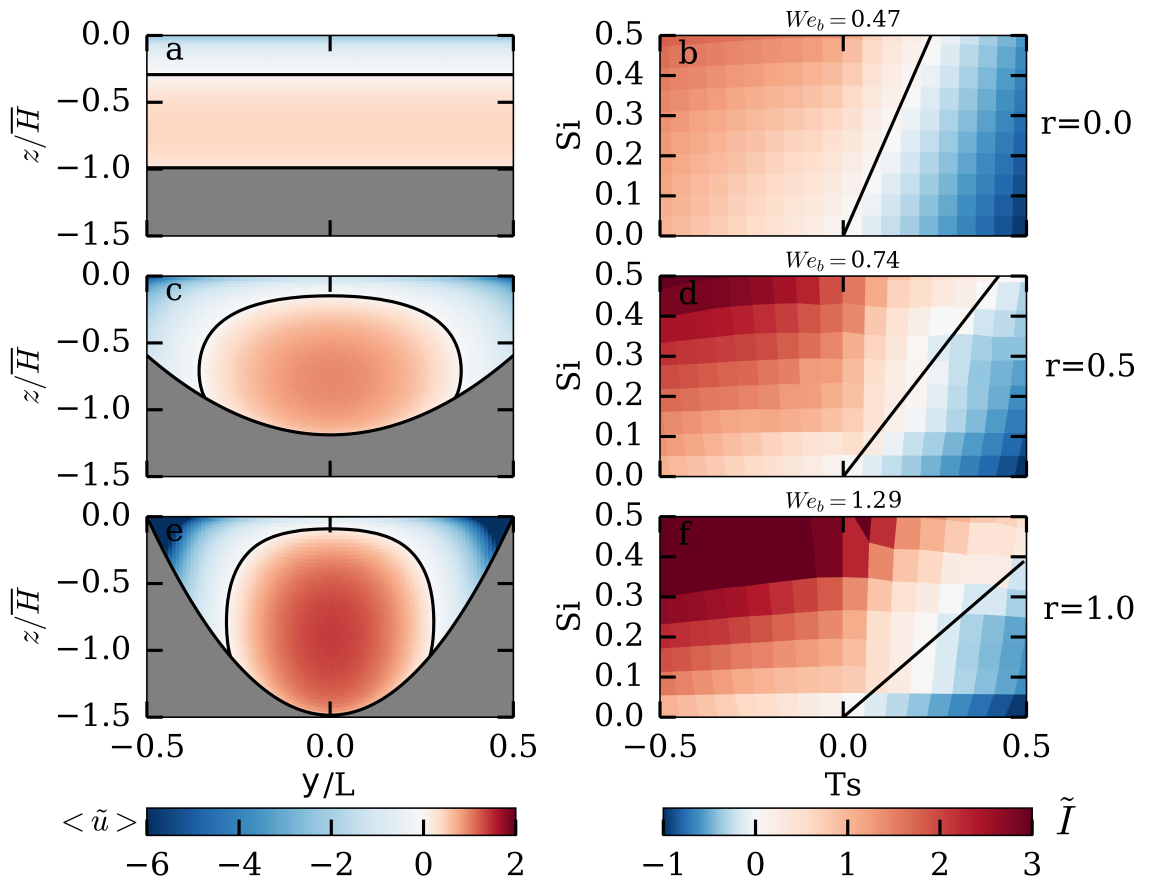
Figure 16: Exemplary tidal mean velocity $\tilde{u}$ (left) and strength of exchange flow $\tilde{I}$ (right) in a cross-section of an estuary with varying steepness parameter r. The bold line in (b,d,f) marks the $\tilde{I} = 0$ condition where gravitational forcing (Si) and up-estuary wind stress (Ts > 0) cancel each other out.

exchange flow strength $\tilde{I}$ (right) for different bathymetries are shown in Figure 16 exemplarily for the three ratios $r = 0, 0.5$ and 1.0. For the presentation of velocities Si $= 0.0$ and Ts $= 0.25$ has been used. Larger steepness of the transect results in a pronounced near-bottom current in the center of the channel while the return

flow occurs mainly at the banks. The maximum velocity observed in the different simulations increases with larger values of r indicating a stronger exchange flow with increasing cross-section steepness. The latter becomes more clear in Figure 16 b,d,f which shows $\tilde{I}$ in the Si-Ts parameter space, as introduced in Section 3.2, with the black line representing the transition from classical to inversed estuarine circulation. For the special case $r = 0$ (flat bottom) the results are identical with the 1D simulations in Section 4.2 with $\text{We}_b \approx 0.45$ for the tidally dominated scenario. An increasing value of r leads to a smaller slope of the $\tilde{I} = 0$ isoline indicating a larger basic Wedderburn number. Increasing the steepness to $r = 0.5$ increases We_b to a value of 0.74 (Fig. 16d) and for a fully parabolic bathymetry ($r = 1.0$) $\text{We}_b = 1.29$ is reached (Fig. 16f). Since tidal velocity amplitude and cross-section area are kept constant within the simulations, an increased value of We_b originates from lateral variations in the bathymetry. These amplify density-driven estuarine circulation in such a strong way that three times the up-estuarine wind stress is needed to compensate the gravitational forcing. We_b depends nearly linearly on the steepness parameter r (Fig. 17).
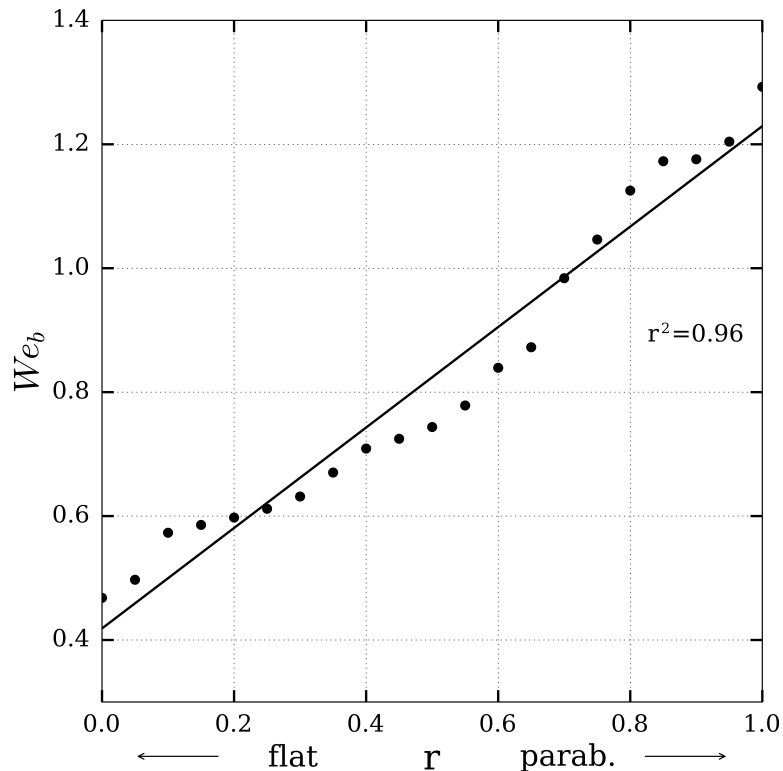

Figure 17: Basic Wedderburn number We_b for varying cross-section steepness r. Larger values of We_b means stronger up-estuary wind is needed to invert gravitational estuarine circulation.

4.4 3D-Application

The preceding analytical and numerical studies with reduced physics highlighted the significance of the slope of the $\tilde{I} = 0$ isoline in the Si-Ts parameter space and the derived basic Wedderburn number We_b, as an indicator for the sensitivity of an estuary to wind stress. The objective of this study is now to calculate We_b for a full 3D realistic scenario. For that, the theoretical findings of above will be applied and compared to results of a numerical model of a tidal inlet in the Wadden Sea. The latter are validated and published model simulations obtained by Purkiani et al. (2015) and Purkiani et al. (2016) which are here reevaluated in terms of the newly derived theory. Different from the previous studies the buoyancy (calculated using the full 3D buoyancy equation) and wind stress are now evolving and spatially heterogeneous.

The tidal inlet has a maximum depth of about 30 m and a width of 2 km connecting the Sylt-Rømø Bight to the German Bight in the south-eastern North Sea (see Figure 18). The Sylt-Rømø Bight is a semi-enclosed bight covering an area of approximately 410 km^2 (including 190 km^2 intertidal flats). Freshwater sources in the bight are mainly given by precipitation ($P \approx 0.8$ m/year) and river discharge ($4 - 10 \, \mathrm{m^3 \, s^{-1}}$) which generally leads to a positive buoyancy gradient into the Sylt-Rømø Bight (Burchard et al., 2008). Observations in the tidal inlet show significant tidal straining (Becherer et al., 2011), which is strongly modified by lateral circulation mainly triggered by curvature (Purkiani et al., 2015). Analysis of numerical model results for the Sylt-Rømø Bight showed a strong dependence of the estuarine circulation on wind straining (Purkiani et al., 2016). Similar to the idealized simulations the tidal velocity amplitude is up to $1 \, \mathrm{m \, s^{-1}}$, with a tidal range of about 1.8 m characterized by the semi-diurnal M$_2$ tidal mode.

The model results were calculated with the 3D coastal ocean model GETM (see Section 2.2.2) on a numerical grid with 100 m horizontal resolution, 25 equidistant bottom following σ-coordinates for the vertical discretization and using the same turbulence closure model as above. The model is one-way nested into a larger scale model of the North Sea and German Bight which calculates time series of current velocities and water level as well as vertically resolved temperature and salinity at the open boundaries (see Purkiani et al., 2015, for details). Temporally and spatially varying realistic wind forcing is calculated using data provided by the *German Weather Service Local Model* (DWD-LM) giving highly resolved results on a grid with 7 km horizontal resolution. The original study focuses on a transect across the tidal inlet connecting two moorings which has been used to calibrate the model results with observational data (Purkiani et al., 2015). Purkiani et al. (2016) then reused this transect, for consistency reasons, for evaluating the influence of wind
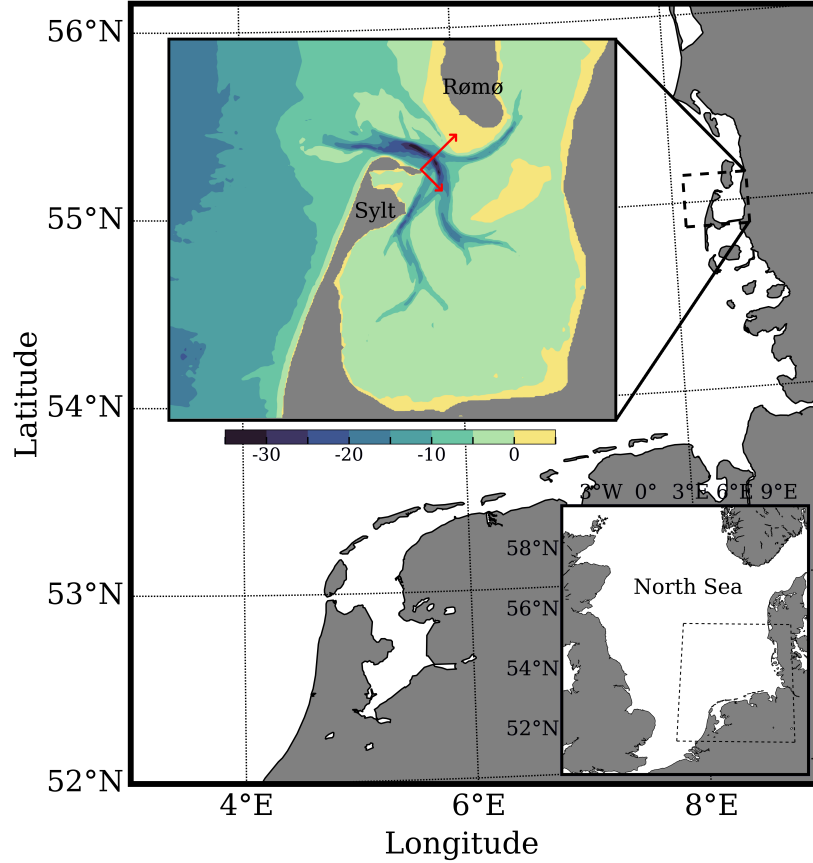
Figure 18: Map of the Sylt-Rømø Bight (upper left panel) with its bathymetry and the German Bight in the North Sea (lower right panel). The cross-estuary transect with the orientation of the local coordinate system (x-axis pointing into the bight) is shown in red.

straining on the circulation in the channel. Reanalysis of these results showed that the monthly mean lateral cross-section velocity component is about $5\,\mathrm{cm\,s^{-1}}$ instead of zero, indicating a slightly misaligned transect biasing along-estuary results. For this reason, the alignment and position of the transect were optimized in the current study to achieve a zero-mean cross-channel circulation. With this, delinking of along-channel and cross-channel stresses, density gradients and horizontal velocity components is possible for further analysis:

First, the horizontal vectorial quantities (current velocity, wind stress and density gradient) were projected on the cross-sectional transect followed by a tidal-average according to Eq. (1), considering depth-weighting in the σ-space for conserving mass and momentum (Klingbeil et al., 2018). Then, Simpson number Si and non-dimensional wind stress Ts are calculated using the definitions in Section 2.1.4 and the non-dimensional strength of the exchange flow $\tilde{I}$ is calculated according to (31). Figure 19 shows time series of Ts, $\tilde{I}$ and Si calculated for the transect in Fig. 18 for February 2008. In times of no wind and a positive buoyancy gradient (day 8 -

16) the resulting exchange flow corresponds to classical estuarine circulation ($\tilde{I} > 0$) driven by a positive buoyancy gradient. An inversed circulation ($\tilde{I} < 0$) results from up-estuary wind (Ts > 0) or an inversed density gradient (Si < 0). The existence of the latter in non-arid regions will be shown in more detail in Section 5.4.3. The analytical value of $\tilde{I}$, calculated according to Eq. (33), is shown in dashed for comparison. It underestimates the numerical $\tilde{I}$ due to missing physical processes in its derivation, but generally follows the trend. The response time of the exchange flow upon changes in wind and density gradient is almost instantaneously which allows the presentation of the results in a Si-Ts and Si-We parameter space without further processing (Fig. 20).
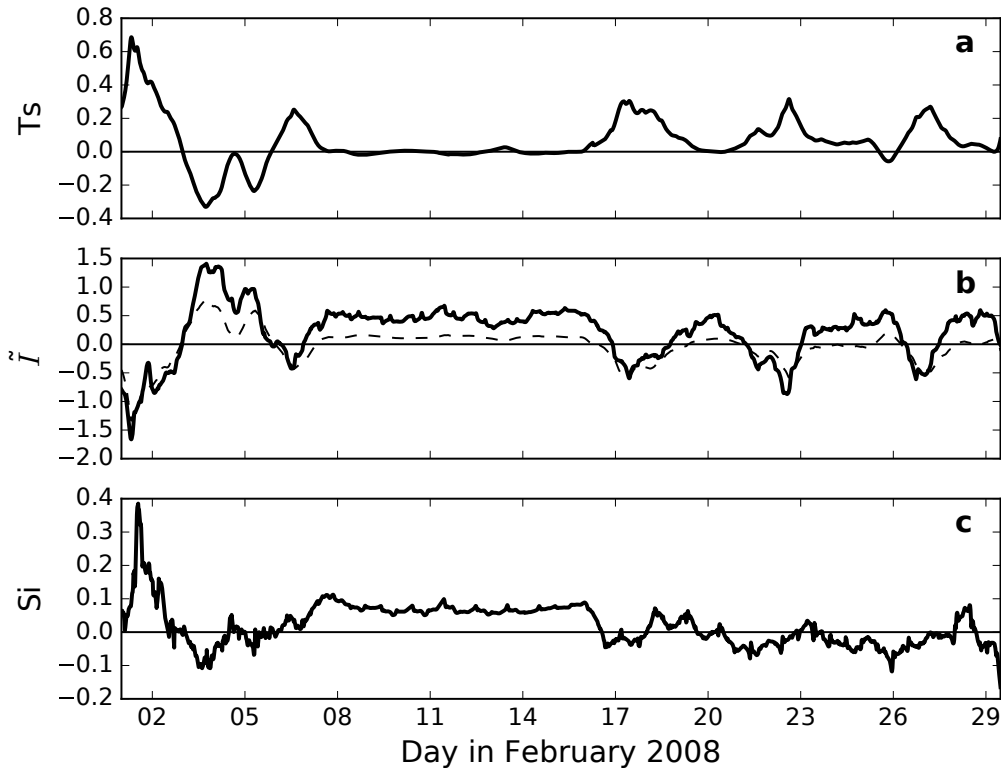
Figure 19: Calculated time series of a) non-dimensional wind stress Ts b) non-dimensional exchange flow intensity $\tilde{I}$ and c) non-dimensional density gradient Si for the transect marked in Fig. 18. The results are based on data of Purkiani et al. (2016) for February 2008. The dashed line in b) shows $\tilde{I}$ calculated with help on an analytical solution.

Similar to the analytical and numerical results from above, the strength of the estuarine exchange flow $\tilde{I}$ can be distinguished between positive and negative circulation, shown in red and blue, respectively. The results agree with the former parameter studies in a way that strong landward wind (Ts > 0) and a negative buoyancy gradient (Si < 0) results in a reversed circulation. Likewise the stronger

the up- and down-estuary wind the stronger the resulting exchange flow. In order to determine the basic Wedderburn number in the Si-Ts parameter space, the $\tilde{I} = 0$ condition has to be ascertained. The analytical solution (34) suggests that the presence of a residual flow does not change the slope of the $\tilde{I} = 0$ isoline but instead leads to a horizontal shift. In the realistic scenario $\tilde{U}_r$ varies with river discharge and changes of water level. Because of that a least-square surface regression is conducted, motivated by the planar structure of Eq. (33):

$$\tilde{I} = a \cdot \text{Ts} + b \cdot \text{Si} + c, \tag{38}$$

where (a, b, c) are fitting parameters. A threshold value of $|\tilde{I}| \leq 0.4$ is used in the calculation of the regression in order to exclude possible immoderate events e.g. strong deviations of the water level. With this, the basic Wedderburn number is given by $\text{We}_b = -b/a$. The resulting value of $\text{We}_b = 0.59 \pm 0.15$ is larger than the results obtained by the 1D analytical stationary solution ($\text{We}_b = 0.15$) and the numerical parameter study in Section 4.2 ($\text{We}_b = 0.45$). Rather, it fits well in the range found above for tidally oscillating estuaries including lateral effects due to varying bathymetries ($\text{We}_b = 0.45...1.3$). In the Si-We parameter space this value describes the limiting value for the hyperbolas where residual flow becomes irrelevant as already predicted by the analytical solution.
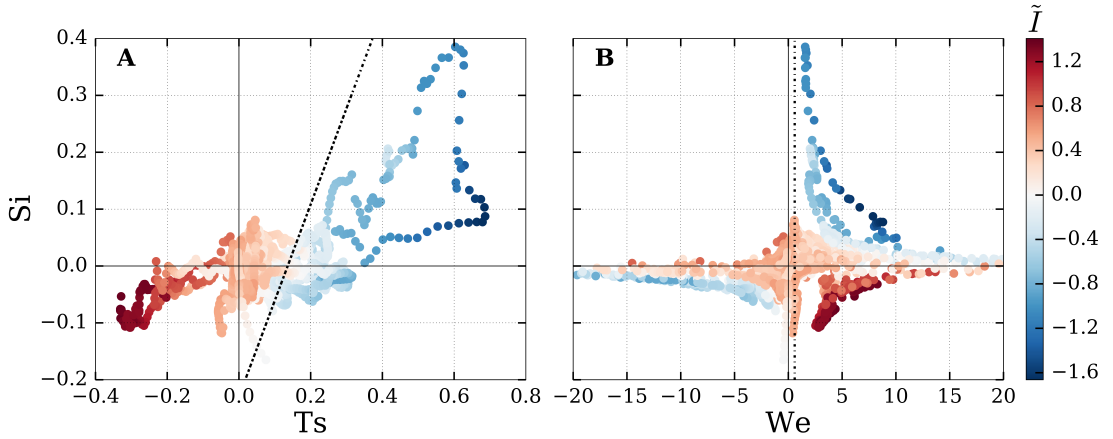

Figure 20: Data shown in Fig. 19 presented in a Si-Ts and Si-We parameter space as defined in Fig. 8 and Fig. 11. The $\tilde{I} = 0$ line for inversion of estuarine circulation is calculated from a least-square surface regression. The corresponding basic Wedderburn number is $\text{We}_b \approx 0.60$.

4.5   Conclusions

The simplifications used in deriving the stationary analytical solution in Section 3.2 can be removed by applying numerical models to study the influence of dynamic drivers of estuarine circulation on the basic Wedderburn number We_b. That is done by applying 1D, 2D and 3D model configurations including realistic solutions of the corresponding buoyancy equation and its feedback on the turbulent eddy viscosity as well as the related effects of tidal straining. By analyzing the slope of the $\tilde{I} = 0$ isoline in a parameter space spanned by the Simpson number Si and the non-dimensional wind stress Ts, the value of We_b for different scenarios can be estimated. The dynamical 1D case without tides ($U_t \approx 0$) confirmed the analytical value of 0.15 in good agreement (Fig. 12). The results suggest that the larger the tidal velocity amplitude the larger the ebb-flood asymmetry of the eddy viscosity (e.g. due to varying vertical stratification) leading to an increased net inflow near-bottom and net outflow near-surface of the gravitational circulation when tidally averaged. As a consequence more up-estuary wind (Ts > 0) is needed to invert the classical estuarine circulation increasing the critical threshold We_b to values of about 0.45 meaning that in the presence of tides non-dimensional wind forcing has to be 45% of non-dimensional buoyancy gradient forcing (Fig. 11). When additionally considering a laterally varying bathymetry in the 2D scenarios (Fig. 16) this value increases even further to $\text{We}_b \approx 0.45...1.3$ (Fig. 17) depending on the steepness of the transect (ratio of water depth at the banks to depth at the center). By reevaluating model results of a realistic 3D scenario of a tidal energetic inlet a value of $\text{We}_b \approx 0.60$ is found (Fig. 20) which is in the range suggested by the 2D cross-estuarine model as a sum of tidal straining and lateral effects.

The existence of a three-layered flow around the $\tilde{I} = 0$ isoline in the Si-Ts and Si-We parameter space, as predicted by the analytical solution, could be confirmed (Fig. 14). The corresponding limiting minimum and maximum Wedderburn numbers are larger than the values presented in Section 3.3 due to the larger basic Wedderburn number. In addition a classification of velocity profiles into five flow classes is introduced by dividing the parameter space in regions dominated by wind and buoyancy gradient forcing and the interaction of both, showing the transition from classical estuarine circulation to inverted circulation which is dominated by wind.

5 Exchange flows in a weakly tidal estuary

5.1 Motivation

The findings in section 3 and 4 highlight the basic Wedderburn number We_b as a parameter for describing the sensitivity of the exchange flow in an estuary to wind forcing. While the former study focuses on the influence of tides in increasing We_b and confirms the applicability of the analytical theory on a realistic 3D tidal inlet, here the results are tested on a realistic weakly tidal estuary exemplarily using the Warnow river in the south-western Baltic Sea. The importance of the exchange flow in the Warnow estuary and its variability with respect to wind forcing is recently underlined by Buer et al. (2018) when studying the transport of *Escherichia coli* bacteria and the resulting bathing water quality. Moreover, Enders et al. (2019) showed in the Warnow estuary the importance of bottom stress for the accumulation of microplastics in the sediment within the estuary.

The aim of this study is now to test if the theory developed in the former sections is still valid even though the non-dimensional parameters are defined for tidal applications, and if the results for the basic Wedderburn number fit in the range proposed above. This chapter is structured as follows: first, the study site is introduced together with its wind characteristics and tidal properties in Section 5.2, followed by a description of the numerical models and their validation (Section 5.3). Finally, the results are presented in Section 5.4 including observations, statistics of annually averaged model results as well as evaluations of the estuarine circulation for a transect at the mouth of the estuary. After investigating the estuarine mixing in Section 5.5 conclusions are drawn in Section 5.6.

5.2 The Warnow estuary

5.2.1 The study site

The Warnow river is located at the German coast of the south-western Baltic Sea (see Fig. 25) near the city of Rostock. Its river discharge varies seasonally with typical values found between $50\,\mathrm{m^3\,s^{-1}}$ in February and $5\,\mathrm{m^3\,s^{-1}}$ in August with an annual mean value of about $Q_r = 15\,\mathrm{m^3\,s^{-1}}$ (Fig. 21). The discharge into the estuarine part is controlled by a weir, which limits the spatial extent of the estuary to the south. In the north the estuary is bounded by two pier heads with a distance of $230\,\mathrm{m}$, which also serve as endpoints of a transect later used for further analyses. In addition the shoals are largely artificially fortified, since the Warnow estuary plays a large role in tourism and industry. Because of these barriers the boundaries of the study site are well defined leading to a total estuary length of about $13\,\mathrm{km}$ and a mean water depth of $5.6\,\mathrm{m}$. With this, the flushing time of the estuary results in $T_{fl} = V/Q_r \approx 54\,\mathrm{d}$, where the underlying total water content of $V = 70.4 \times 10^6\,\mathrm{m^3}$ is calculated from the bathymetric data shown in Fig. 25. A more realistic value, obtained from a numerical model including the estuarine exchange flow, is approximately half the size $T_{fl} \approx 30\,\mathrm{d}$ (see Appendix I), highlighting the role of estuarine circulation on the water exchange. Deepest points in the estuary are located in the shipping channel
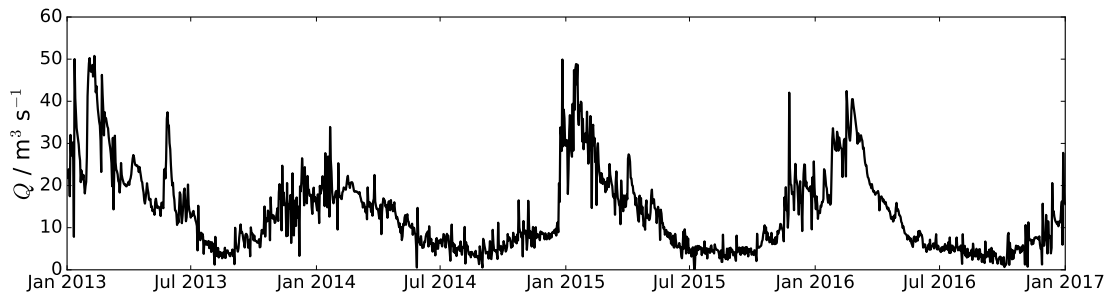

Figure 21: Daily averaged values for the river discharge into the Warnow estuary.

with a depth of about $15\,\mathrm{m}$ reaching $5.5\,\mathrm{km}$ into the adjacent Bay of Mecklenburg (Fig. 25). Due to this channel the Warnow estuary is hydrologically connected with deeper parts of the ambient coastal water.

5.2.2 Wind characteristics

As shown in the previous sections wind forcing is, aside from gravitational forcing, a key mechanism in driving estuarine circulation. Figure 22 shows the relative frequency of observed wind velocities in a height of $10\,\mathrm{m}$, measured by the German Weather Service (DWD) near the mouth of the Warnow estuary, divided into velocity classes of $0.5\,\mathrm{m\,s^{-1}}$. The underlying data set covers the years $2013 - 2017$. The
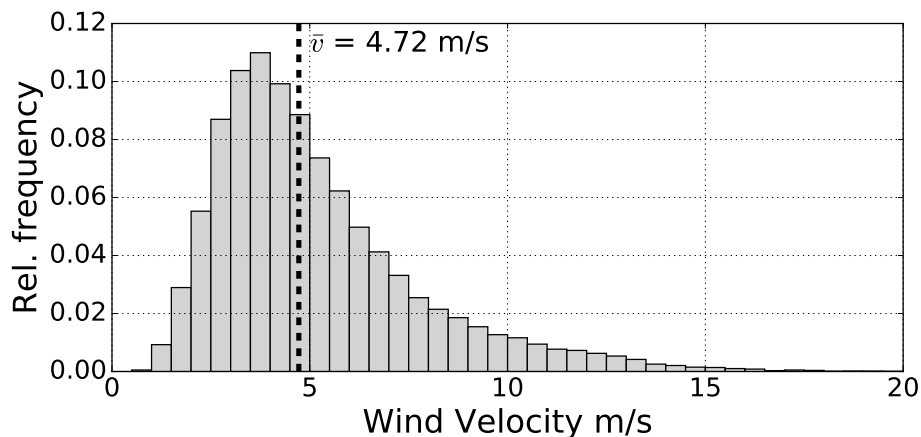
Figure 22: Frequency of hourly measured wind velocities at the mouth of the Warnow estuary in $10\,\mathrm{m}$ height in intervals of $0.5\,\mathrm{m\,s^{-1}}$ with its mean value shown as a dashed line.

distributions of wind velocities approximately follow a Weibull-distribution (see e.g. Lun and Lam, 2000), here having a mean value of about $4.7\,\mathrm{m\,s^{-1}}$. Roughly $5\,\%$ of the velocities are observed to be larger than $10\,\mathrm{m\,s^{-1}}$ (see Table 1). The correspond-

Table 1: Relative frequency of observed wind velocities.

Wind velocity [m/s]	$0 - 5$	$5 - 10$	$10 - 15$	$15 <$
relative frequency	65.6%	29.2%	4.8%	0.4%

ing wind directions are shown in Fig. 23 following meteorological conventions (origin of the wind) with the color code representing ranges of wind velocities. Because the estuary is located mid-latitude and thus in the region of the prevailing westerlies, the largest wind velocities are observed coming from west to north-west. Since the Warnow estuary has a pronounced south-north orientation the wind vectors with the corresponding components are of particular interest. The observations show that wind with a northward component occurs more frequently than with a southward component.
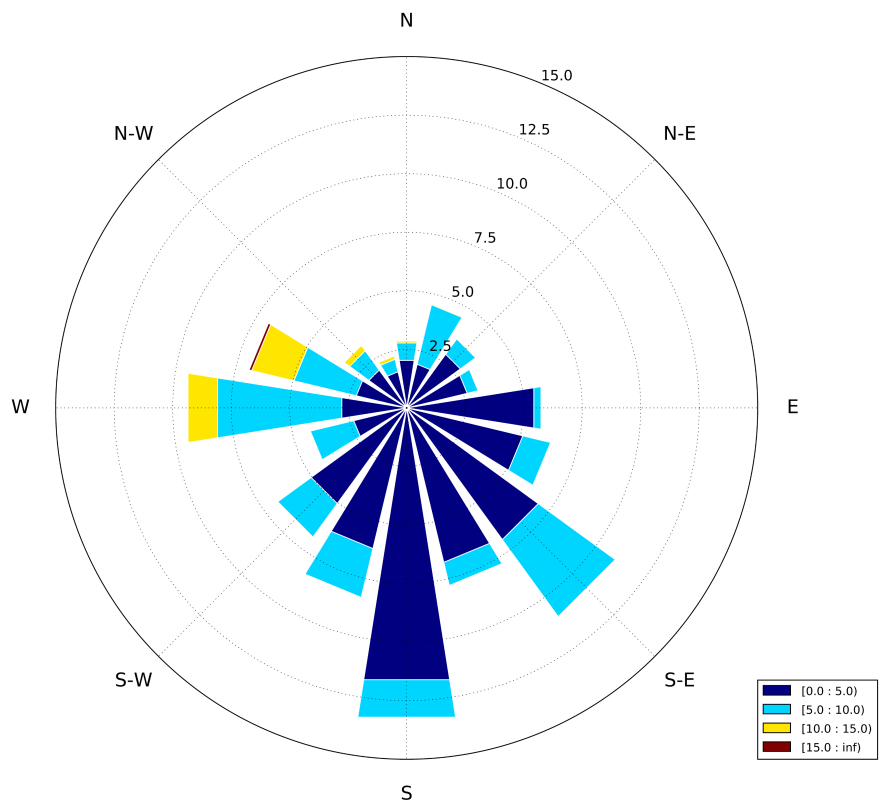
Figure 23: Frequency of hourly measured wind directions (using meteorological convention) at the mouth of the Warnow estuary 10 m height with color coded wind velocities.

5.2.3 Tides

The findings in Section 4 revealed the influence tides have in supporting the gravitational circulation and thus in increasing the basic Wedderburn number We_b. As a consequence the importance of wind increases in weakly tidal estuaries, because less wind is necessary for an inversion of the circulation direction. A tidal analysis for the Warnow estuary is performed by using a Fourier transformation of time series of the water level measured at the weir. The underlying data cover the years $2010 - 2015$ in a temporal resolution of $1\,min$. Because of the long and highly resolved time
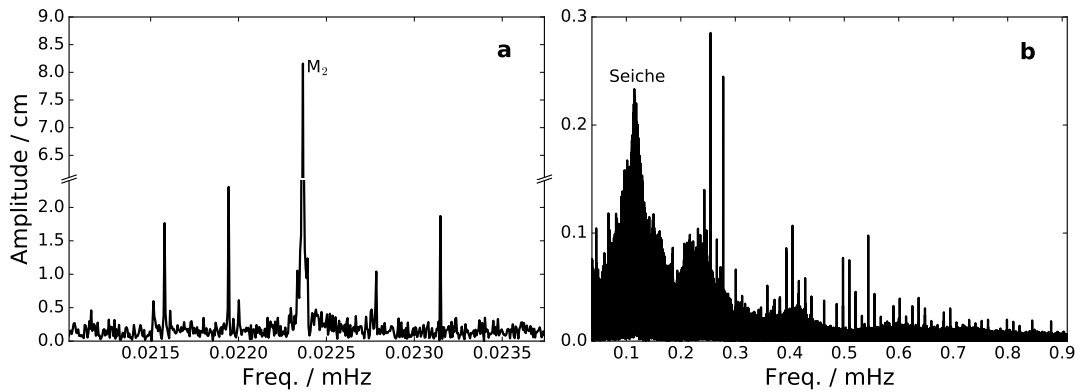
Figure 24: Excerpt of harmonic contributions to sea level changes at the weir in the estuary, exemplarily shown for the M_2-tide (a) and the barotropic seiche (b). Note the different axis-scales.

series a variety of tidal constituents can be identified, where an excerpt is shown exemplarily in Fig. 24. The most important component is the semi-diurnal M_2-tide with an amplitude of about $8\,cm$. Based on these results, the Warnow estuary can be considered as a micro-tidal estuary, synonymously referred to as *weakly tidal* in the following. A special non-tidal type of periodic flow is found with a peak period of about $2.4\,h$: Since the Warnow estuary is a semi-enclosed basin eigen oscillations occur (barotropic seiche) with the zero elevation node being located at the mouth and the maximum elevation observed at the weir. Note that the frequency of the seiche depends on the water depth, which changes temporally due to the varying sea surface height.

5.3 The numerical model

5.3.1 The setup

Similar to the studies in section 4.3 and 4.4 the numerical simulations were carried out with help of the General Estuarine Transport Model GETM (see 2.2 for details) using the General Ocean Turbulence Model GOTM as turbulence closure model (second-order, k-ε, see Section 2.2.1 for details). Note that in this study the same turbulence closure model as for the simulations in Section 4 is used. The simulations were performed in two steps: a large-scale model, covering the region of the western Baltic Sea, was applied in order to calculate boundary conditions for the subsequent simulations of the smaller-scale model of the Warnow estuary and its ambient coast. Both model setups have been developed specifically for the following studies. The model for the western Baltic Sea makes use of a numerical grid in
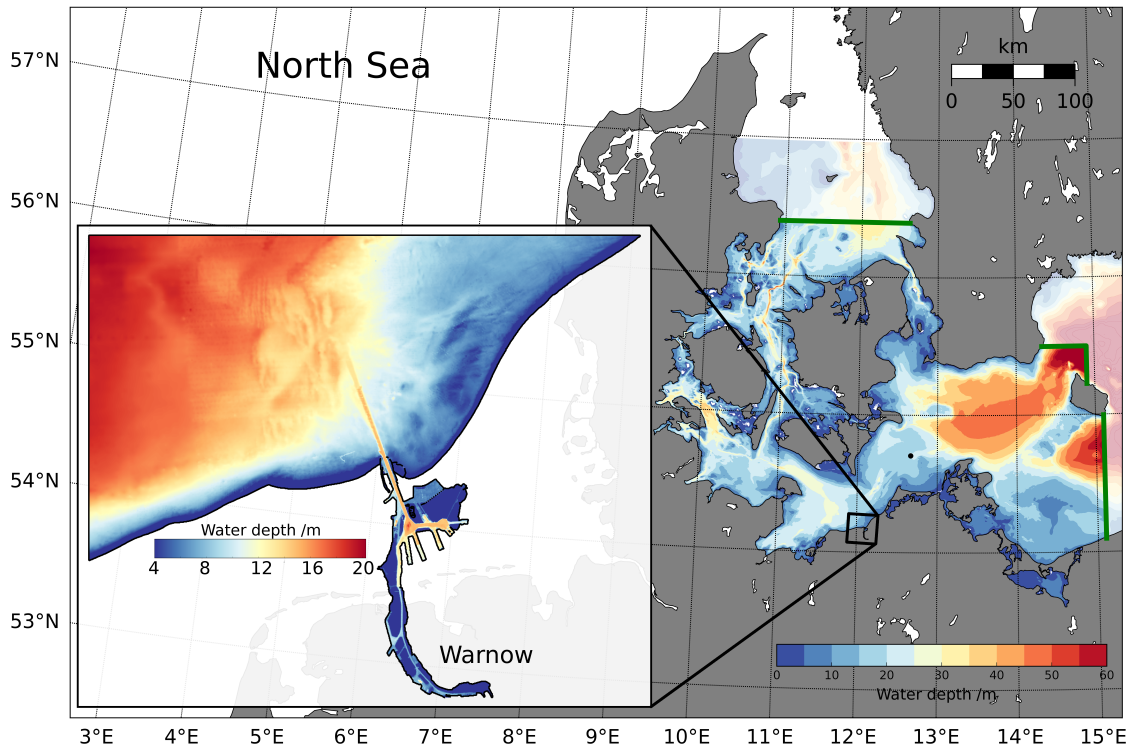
Figure 25: Water depth and expanse of the 20 m model of the Warnow estuary (left) and of the 200 m model of the western Baltic Sea (right). Open boundaries of the latter are highlighted in green, with the larger-scale model (600 m) in semi-transparent. The position of the measurement station 'Darss Sill' is marked as a black dot.

200 m spatial resolution and 40 vertical layers with their layer height adapting to the vertical density gradient (Gräwe et al., 2015; Hofmeister et al., 2010). Time series of water temperature, salinity, horizontal velocities and water level at the open

boundaries (highlighted in green in Fig. 25) are obtained from output of an even larger-scale model of the western Baltic Sea with a resolution of 600 m (see Gräwe et al., 2015, for details). Since the 200 m model has two open boundaries and its hydraulic conductivity is different than in the 600 m model, e.g. due to changed cross-section areas of the channels, the barotropic pressure gradient has been calibrated to compensate for the deviating salinity transports (see e.g. Burchard et al., 2009). Meteorological forcing is calculated from output of the German Weather Service Local Model (DWD-LM) with 3 h temporal and 7 km spatial resolution. The resulting model output of the 200 m model is subsequently used to force the small-scale model of the Warnow estuary at its open boundaries (shown in black in Fig. 25).

The model domain of the Warnow estuary and its adjacent coast are discretized on a structured numerical grid with a horizontal resolution of 20 m using Cartesian coordinates and 25 equidistant bottom following σ-coordinates. For the meteorological forcing the same underlying data set as in the large-scale 200 m model is used. The daily averaged values for the discharge of the Warnow river are provided by the Office for Agriculture and Environment Mittleres Mecklenburg. Both models have a spin-up time of one year, starting from initial conditions of temperature and salinity, spatially interpolated from their larger-scale outer model, respectively. In the following, this study focuses exemplarily on the results for the year 2014, as most of the validation data for the estuary are available during this period.

5.3.2 Validation

Before the numerical results, calculated by the 200 m and the 20 m model, are used for further analysis their quality is estimated by comparison with observational data obtained from measurements. The focus here is especially on the reproduction of the observed salinity, as it largely determines the density and thus the buoyancy gradient which is an important driver of estuarine circulation. Note that the temperature plays only a minor role in changing the density in the western Baltic Sea. For this reason a carefully calibrated large-scale model is necessary to record inflow of high saline water into the western Baltic Sea and to prevent error propagation into the nested small-scale model of the Warnow estuary. A nearby measurement station is the autonomously operating measurement tower *Darss Sill* (marked in Fig. 25) which is part of the MARNET network for marine ecosystem monitoring in the North Sea and the Baltic Sea. Results show that the large-scale 200 m model of the western Baltic Sea reproduced most of the inflow events of saline water in good agreement with observations (exemplarily shown for mid-depth (12 m) in Fig. 26). Note that the specific position of the station at Darss Sill aims to identify inflow of high saline (and usually oxygen-rich) water originating from the North Sea, into

deeper layers of the central Baltic Sea (Gräwe et al., 2015; Burchard et al., 2018a).
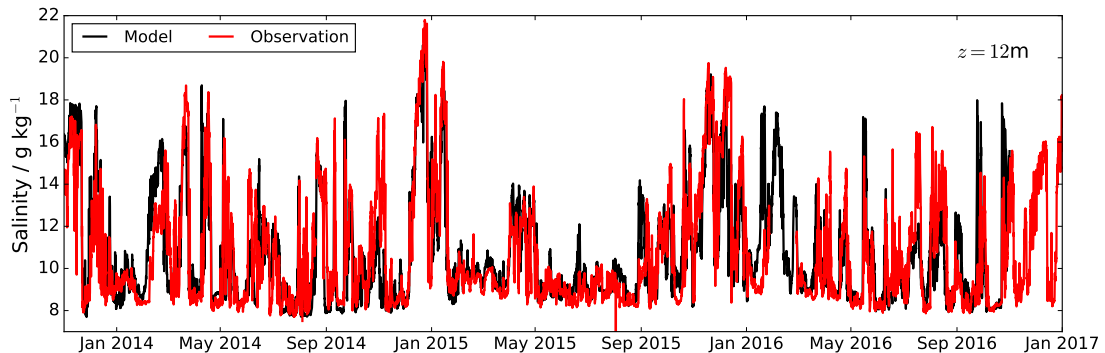

Figure 26: Mid-depth salinity measured at station Darss Sill (red) compared to calculated model results (black) for the western Baltic Sea in 12 m depth.

Figure 27 compares output from the 20 m model of the Warnow estuary in black to observations in red in terms of water level (a), bottom temperature (b) and bottom salinity (c) for the year 2014. The underlying observational data for temperature and water level are provided by the Office for Agriculture and Environment Mittleres Mecklenburg and the salinity is calculated from conductivity measurements of a CTD-probe (Conductivity-Temperature-Depth). As shown in Section 5.2.3 the measured water level includes small tidal variations which is successfully reproduced by the numerical model in terms of timing as well as magnitude. Larger variations of the sea level in the estuary are mainly driven by changes of the water level in the western Baltic Sea caused e.g. by storm events and the resulting compensation movements. The water level is reproduced by the model with a coefficient of determination of $r^2 = 0.84$ and a root mean square error (rmse) of 8.3 cm. The observed and modeled temperature follow a yearly cycle with a highest value of $\theta = 22.3\,°C$ in August and a lowest value of $\theta = 1.2\,°C$ in February. Observations and numerical simulations agree well with a r^2 value of 0.99 but with the model slightly underestimating the bottom temperature between March and May resulting in a rmse value of 0.8 °C. The exceptional event at the end of May, where the temperature dropped by about 10 °C within two days, is captured by the model in good agreement to measured data in time and magnitude. The bottom salinity (Fig. 27c) shows large variations in a range between 9.5 g kg^{-1} and 21.4 g kg^{-1}. Daily values of measured salinity indicate that the modeled salinity is overestimated in February, which is due to overestimated salinities in the 200 m model of the western Baltic Sea (see February 2014 in Fig. 26) passing the error via the open boundaries into the small-scale model. However, in general the inflow events into the estuary (increased salinity peaks) are well reproduced by the model with $r^2 = 0.74$.
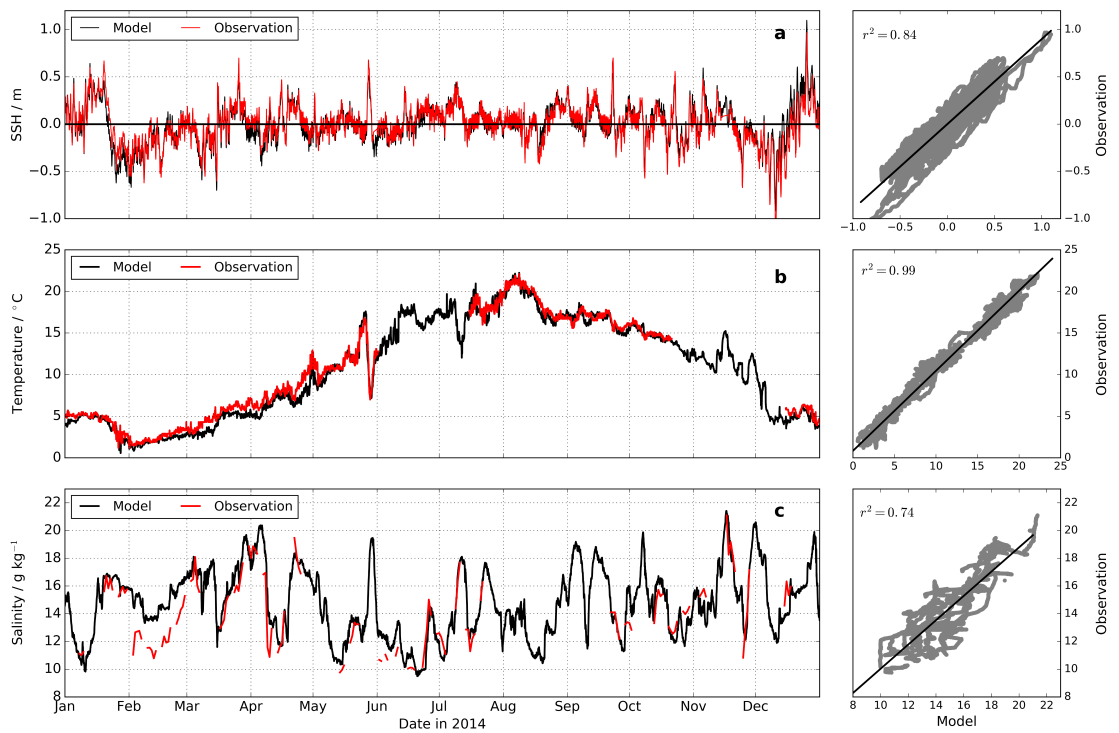
Figure 27: Observation of sea level (a), bottom water temperature (b) and bottom salinity (c) in the Warnow estuary in red compared to model results in black for the year 2014.

5.4 Estuarine Circulation

5.4.1 Observational data

In order to get a broader overview about the dynamics in the near-estuary coastal area, the sea surface temperature (SST) in the western Baltic Sea is calculated from radiances measured by the Earth observation satellite Landsat 8 for a situation in March and July in 2014 (Fig. 28a and b). For that its spectral band 10 (wavelength: $10.30 - 11.30 \, \mu m$) with a spatial resolution of $100 \, m$ and a swath width of $185 \, km$ has been used. Atmospheric correction is applied by using up- and down-welling
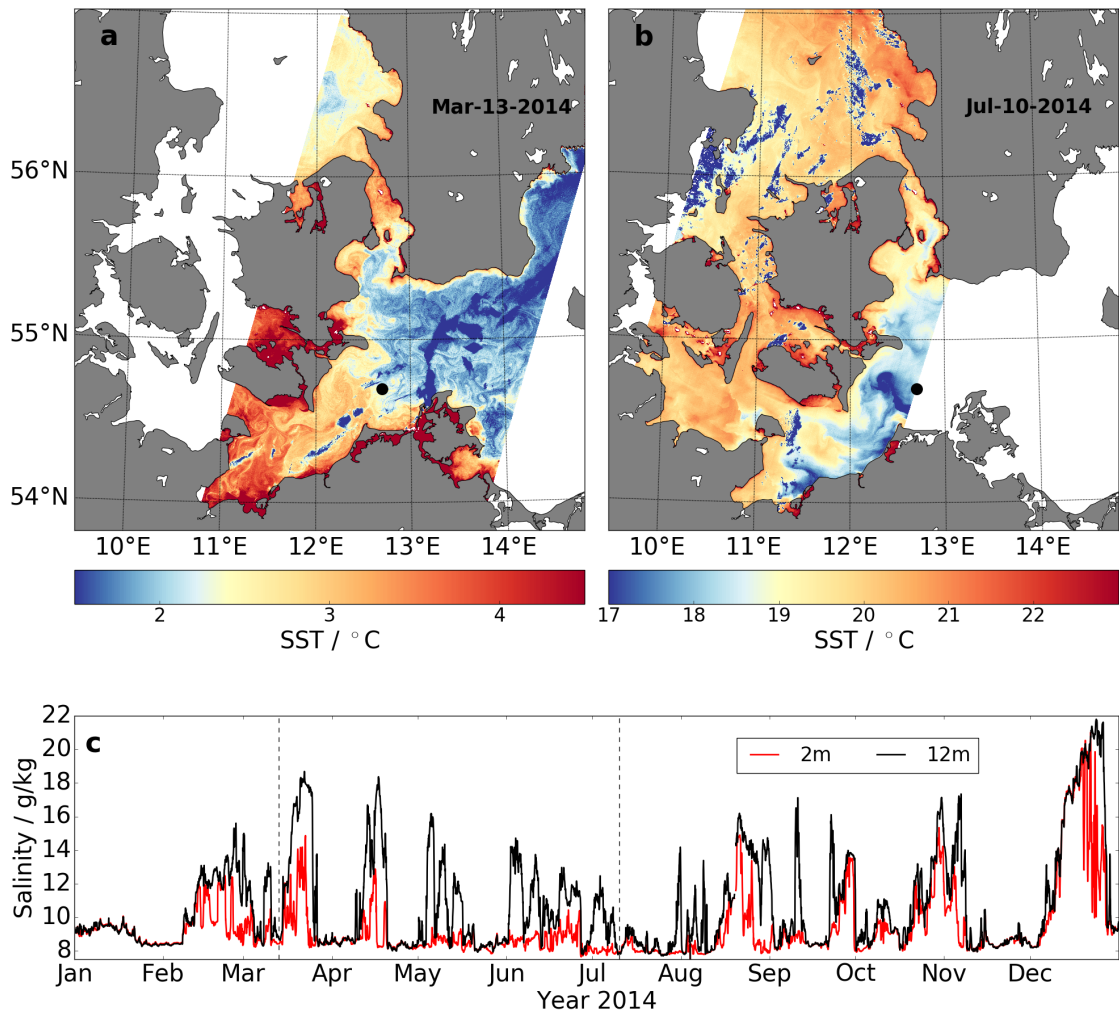
Figure 28: Sea surface temperature (SST) in the Bay of Mecklenburg and parts of the western Baltic Sea calculated from satellite radiances for a situation in a) March and b) July 2014. c) Time series of observed salinity in $2 \, m$ depth in red and mid-depth in black ($12 \, m$). The black dot denotes the corresponding position of the measurement tower Darss Sill. Irregular dark blue patterns are caused by clouds.

radiances as well as the transparency of the atmosphere calculated using a model of a standard atmosphere (for details see e.g. Barsi et al., 2003). Both measurements show a longitudinal gradient in temperature where warmer water is found in the west and colder water in the east with a difference of about $2\,°C$. The origin of these two different water bodies can be identified by considering salinities observed in 2014 by the stationary measurement tower located at Darss Sill, highlighted by the black dot in Fig. 28c. The near-surface salinity ($2\,m$ depth) in red varies between 8 and $15\,g\,kg^{-1}$ while the mid-depth salinity ($12\,m$ depth) varies between 8 and $19\,g\,kg^{-1}$. The measurement dates of the situations in Fig. 28a and b are indicated as dashed lines in Fig. 28c. While in July the colder water has a low surface salinity with values of $s \approx 8\,g\,kg^{-1}$ the situation in March, with warmer water approaching the measurement tower, is captured just a day before the surface salinity increased from 8.5 to $12\,g\,kg^{-1}$. This indicates that the warmer water body has a higher salinity than the colder one, suggesting its origin in water from the North Sea with different properties than the brackish water of the Baltic Sea in the east. Fig. 28 suggests that the Warnow estuary is located in a zone strongly influenced by these two seas resulting in an exposure to ambient water with high salinity (Fig. 28a) as well as with low salinity (Fig. 28b) explaining the high variability in Fig. 27. Changes in salinity in Fig. 28c can be caused by different processes: Besides horizontal advection of North Sea and Baltic Sea water, as shown above, an uplifting of isopycnals due to inflow of dense water at the bottom is able to increase the salinity in shallower areas. Advection in Fig. 28c is marked by changes in both water depths while an uplifting of isopycnals causes changes in the mid-depth salinity but not in the near-surface salinity. Since the shipping channel of the Warnow estuary has a depth of about $15\,m$, both processes potentially increase the salinity in the estuary. The time series in Fig. 28c indicates that changes in salinity (even a doubling) can possibly occur on short time scales of within $2-3$ days.

5.4.2 Annually averaged model results

The observations in the former section suggest a temporally varying salinity in the ambient coastal water of the Warnow estuary, alternating between brackish water and more saline water originating from the Baltic Sea and the North Sea, respectively. Numerical simulations of the western Baltic Sea averaged over the year 2014 show a longitudinal salinity gradient in the surface water with salinities larger than $20\,g\,kg^{-1}$ in the north-west and about $9\,g\,kg^{-1}$ in the east (Fig. 29a). The corresponding bottom salinities are higher in the deeper parts and approximately follow bathymetric features. Results show that the near-bottom currents are generally directed into the Baltic Sea, indicating an inflow of more saline water with increased current speeds in the channels (Fig. 29d). In contrast to this, the velocities at the

surface are directed towards the North Sea, suggesting an outflow of near-surface water. This exchange flow indicates that the western Baltic Sea largely shows the flow characteristics of a classical estuary with saline water being transported into the system, which is then mixed and transported out of the estuary (Knudsen, 1900; Burchard et al., 2018a). Note that the long-term freshwater discharge into the Baltic Sea is estimated at approximately $15\,200\,\mathrm{m^3\,s^{-1}}$ (Matthäus and Schinke, 1999). The
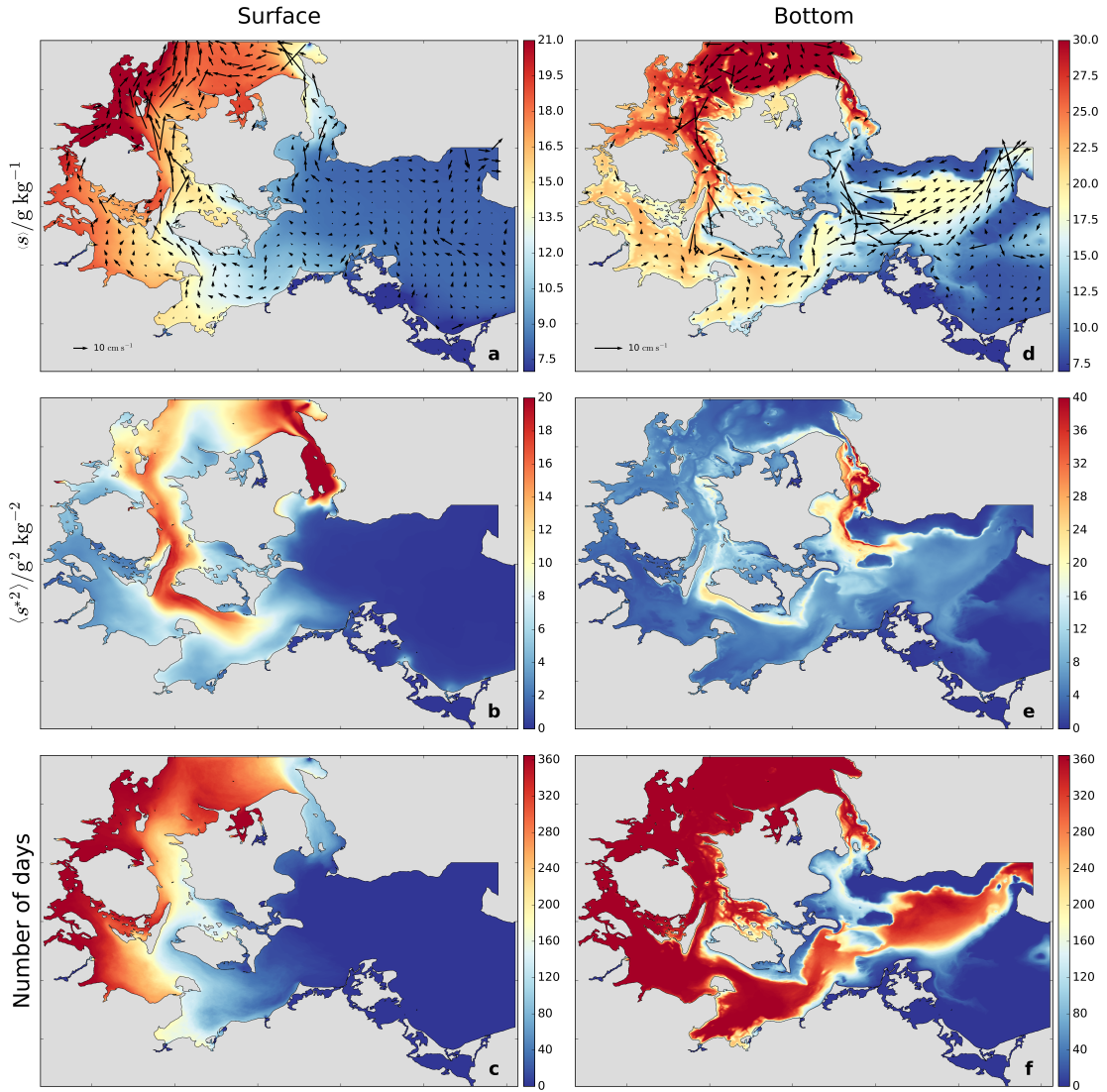
Figure 29: Annually averaged salinity (a,d) and its temporal variance (b,e) at the surface and at the bottom, respectively. The corresponding number of days with salinities larger than $15\,\mathrm{g\,kg^{-1}}$ is shown in (c) and (f). Arrows represent the mean current velocity. The underlying data are obtained from a numerical model for the year 2014.

temporal variance $\langle s^{*2} \rangle$, calculated using deviations of daily averaged values from its annual mean salinity, is small $(< 2\,\mathrm{(g/kg)^2})$ at the surface in the eastern part of the western Baltic Sea indicating only minor changes in salinity (Fig. 29b). Re-

sults show that the situation is different when considering the western parts, which includes the coastal area in front of the Warnow estuary. Here, the surface salinity variance increases to values of $6 - 8\,(\text{g/kg})^2$ and up to $20\,(\text{g/kg})^2$ when considering the Danish streets, highlighting the variability of salinity due to the changing water bodies. The latter is underlined when counting the days with salinities larger than $15\,\text{g}\,\text{kg}^{-1}$. Simulations show that at the surface in the west this threshold value is exceeded on every day of the year 2014 while it is never reached in the eastern part (Fig. 29c). However, in the central area, including the coastal water in front of the Warnow estuary, increased salinities are found on about 120 days. Note that this (arbitrary) threshold of $s = 15\,\text{g}\,\text{kg}^{-1}$ is chosen as an intermediate value between typical maximum $(20\,\text{g}\,\text{kg}^{-1})$ and minimum $(10\,\text{g}\,\text{kg}^{-1})$ bottom salinities observed in the Warnow estuary (Fig. 27c). Bottom salinities are almost always larger in the deeper channels and basins (Fig. 29f).

When focusing on the higher resolved model results for the Warnow estuary, they confirm mean salinities of about $12\,\text{g}\,\text{kg}^{-1}$ at the surface of the coastal water, as already found in the large-scale model. These decrease in the estuary when moving landward (Fig. 30a and Fig. 31a). The salinity variance at the bottom indicates that the shallower areas are exposed to larger variations in contrast to the deeper parts and the estuary itself (Fig. 30e). In the Warnow estuary largest variances in salinity are found near the discharge entrance where freshwater and more saline estuarine water both affect the local salinity (Fig. 31b). In addition to the large-scale dynamics of high saline and brackish water in the western Baltic Sea, results in Fig. 30e show that the near-coastal water is influenced by the effect of coastal upwelling, as indicated by increased values of days exceeding the threshold of $15\,\text{g}\,\text{kg}^{-1}$. The bottom salinity highlights the role of the shipping channel in connecting the estuary with the deeper and more saline offshore water. Current velocities in this channel show a near-bottom up-estuary transport and a near-surface seaward transport verifying the existence of estuarine circulation in the Warnow estuary.

5.4.3 The Total Exchange Flow

In the following, results obtained by the small-scale model are evaluated at a transect between the pier heads at the mouth of the river, in order to study the exchange flow in the Warnow estuary. When analyzing the structure of the cross-sectionally averaged along-estuary velocity component $u(z)$, distinguished into seaward flow $(u < 0)$ in blue and up-estuary flow $(u > 0)$ in red, three scenarios can be identified (Fig. 32): (a) classical estuarine circulation (blue over red), (b) inverse estuarine circulation (red over blue) and (c) three-layered flow (e.g. red-blue-red). All situations occurred frequently during the year 2014 (Fig. 32d). Observations in Section 5.4.1 and the model results in Section 5.4.2 revealed that the changing water bodies in the
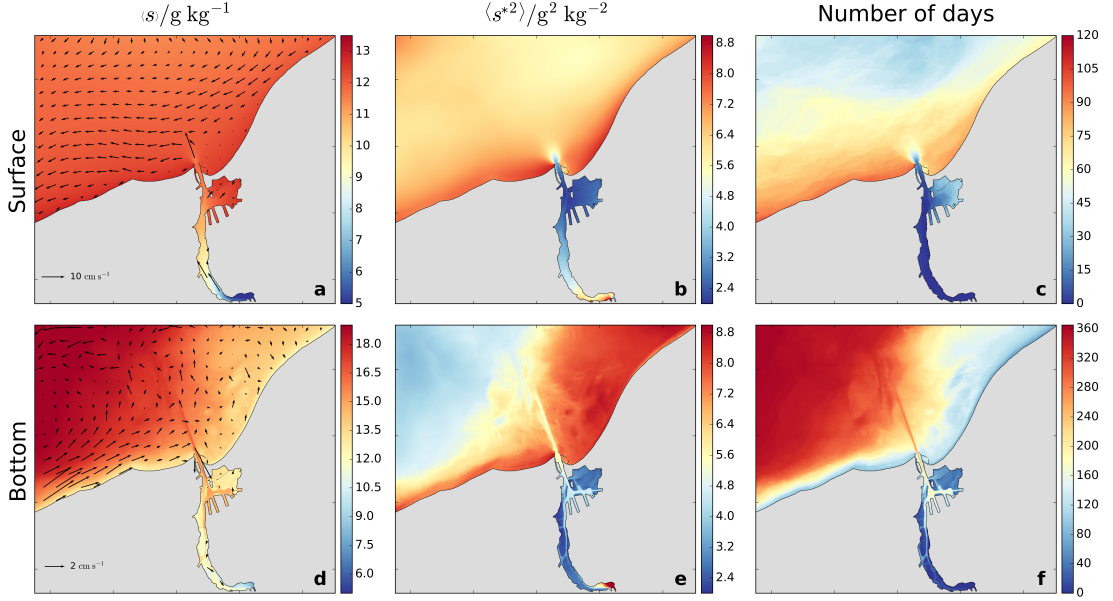
Figure 30: Same as in Fig. 29 but showing model results obtained for the Warnow estuary. Note the different scales in the panels.

western Baltic Sea cause a highly variable salinity in the coastal area of the Warnow estuary (Fig. 30b and e). In order to combine the estuarine exchange flow (Fig. 32d) with the corresponding in- and outflow salinity, MacCready (2011) proposed a transformation from the Eulerian parameter space into the salinity parameter space described in the framework of the *Total Exchange Flow* (TEF). For that the net volume flux per salinity class q is calculated as

$$q\left(S\right) = -\frac{\partial Q\left(S\right)}{\partial S} \quad \text{and} \quad Q\left(S\right) = \left\langle \int_{A(S)} u \mathrm{d}A \right\rangle, \tag{39}$$

where $A(S)$ is the cross-sectional transect area with salinities larger than S. Figure 33d shows the time series of q calculated for the transect at the mouth of the estuary, with positive values in red meaning inflow (up-estuary) while outflow (negative) is shown in blue. Note that the salinity axis is decreasing upward since in a stably stratified water column larger salinities are found near the bottom and lower salinities can be interpreted as being located near the surface. With this, classical estuarine circulation is described by inflow in high salinity classes and outflow in low salinity classes and reversed circulation correspondingly vice versa. The transition from positive to negative circulation is often connected with a shift in the salinity regime where the lowest occurring salinities decrease rapidly (see e.g. Fig. 33d at
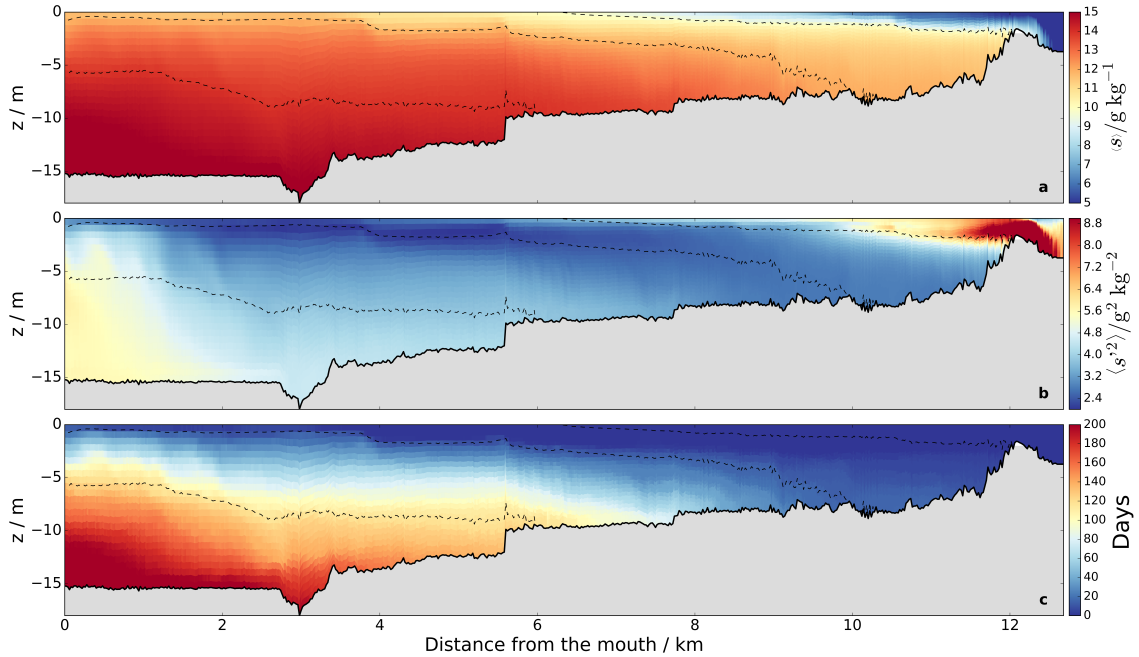
54

Figure 31: Annually averaged salinity (a) and its temporal variance (b) for an along-channel transect in the Warnow estuary. The corresponding number of days with salinities larger than $15 \, \mathrm{g \, kg^{-1}}$ is shown in (c). Dashed lines show isohalines with salinities of $10 \, \mathrm{g \, kg^{-1}}$, $12 \, \mathrm{g \, kg^{-1}}$ and $14 \, \mathrm{g \, kg^{-1}}$ (from top to bottom). The underlying data are obtained from a numerical model for the year 2014.

the end of May with a decrease in salinity from about 15 to $9 \, \mathrm{g \, kg^{-1}}$). This low saline water must originate from the outer ambient coastal area, since the volume flux in the low salinity classes points into the estuary (shown in red), underlining the findings of Section 5.4.1 of an alternating salinity varying between relatively large values and more brackish ones in the western Baltic Sea. Since the outer changes in salinity may occur on short time scales (Fig. 28c) compared to the estuarine adaption time to the new salinity, the density gradient potentially reverses its direction. Due to this, the resulting longitudinal buoyancy gradient $\partial_x b$ at the mouth (transect-averaged) varies in a range between -8 and $+8 \times 10^{-5} \, \mathrm{s^{-2}}$ (Fig. 33a). The corresponding strength of the estuarine circulation I (unscaled version of Eq. 31) generally follows the trend of the buoyancy gradient (Fig. 33c) with a negative gradient resulting in an inverted circulation direction, similar to the results for the tidal channel in Section 4.4 (compare Fig. 19).

By analyzing the direction of the buoyancy gradient its relative frequency of inversion ($\partial_x b < 0$) sums up to 49 % for the year 2014, while for the estuarine circulation a reversion $I < 0$ is found to occur only in 33 % of the data. This imbalance indicates that an additional process must be involved in driving the exchange flow and opposing the gravitational forcing, which is identified as wind straining in the previous sections. The results in the former sections suggest that the estuarine cir-
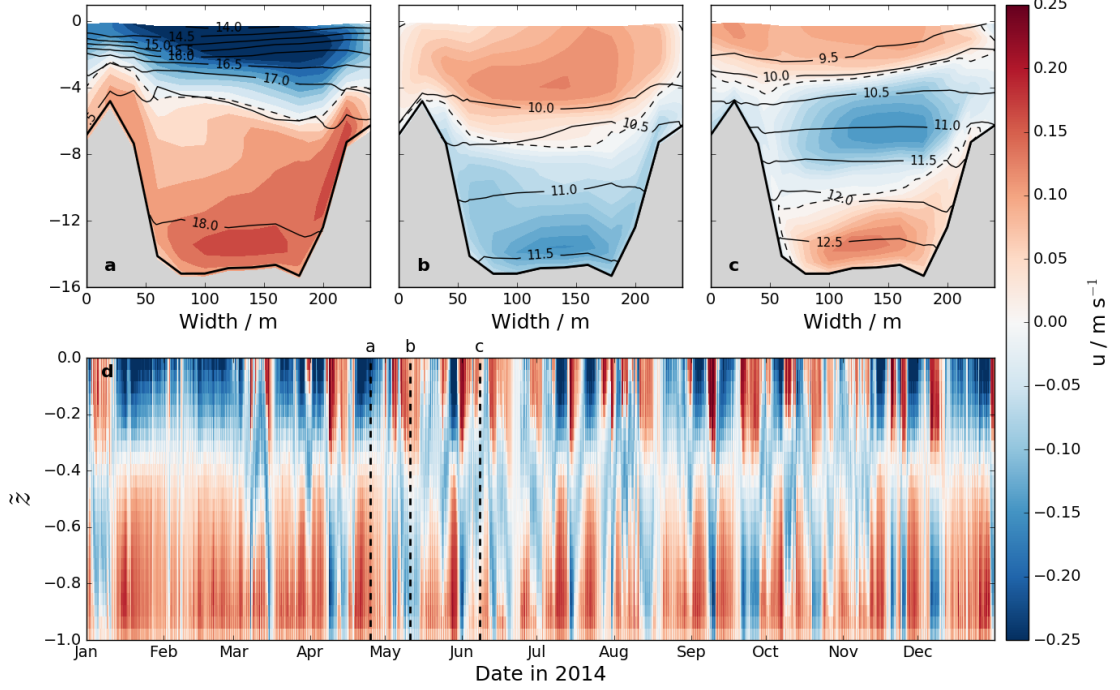
Figure 32: (a)-(c): Along-estuary exchange flow for a transect at the mouth of the estuary for three situations with negative values (blue) pointing seaward and positive values (red) pointing landward. The dashed line indicates $u = 0$, while the solid contour lines give the salinity in $\mathrm{g\,kg^{-1}}$. (d) Time series of the transect-averaged velocity with dashed lines presenting the dates of (a)-(c).

culation $\tilde{I}$ is fully described in a parameter space spanned by the Simpson number Si and the non-dimensional wind stress Ts. This is done by scaling $\partial_x b$, τ_x^s and u with the bottom friction velocity scale according to the definitions presented in section 2.1.4 and 3.3. Since the Warnow is a weakly tidal estuary, typical values of U_* are found to be smaller than $1\,\mathrm{cm\,s^{-1}}$ (Fig. 33c) and thus an order of magnitude weaker than subtidal friction velocities in tidally energetic estuaries. As a consequence, the values of the non-dimensional parameters Si, Ts and $\tilde{I}$ are larger than in the former studies. However, results show that the exchange flow can still be distinguished between positive and negative circulation, shown in red and blue in Fig. 34a, as suggested by the analytical theory and confirmed by the parameter study in Section 4. The critical condition for cancellation $\tilde{I} = 0$ separates both states, indicated by a bold line. Its slope is obtained from a 3D planar regression (Fig. 34b) according to Eq. 38, as already applied to results of the tidal inlet in the Wadden Sea in Section 4.4. With this, the basic Wedderburn number for the Warnow estuary is calculated as $\mathrm{We}_b = 0.33$.

The analytical results in Section 3.3 and the numerical parameter study in Section 4.2.3 both suggest that around the $\tilde{I} = 0$ isoline exists an area with three-layered
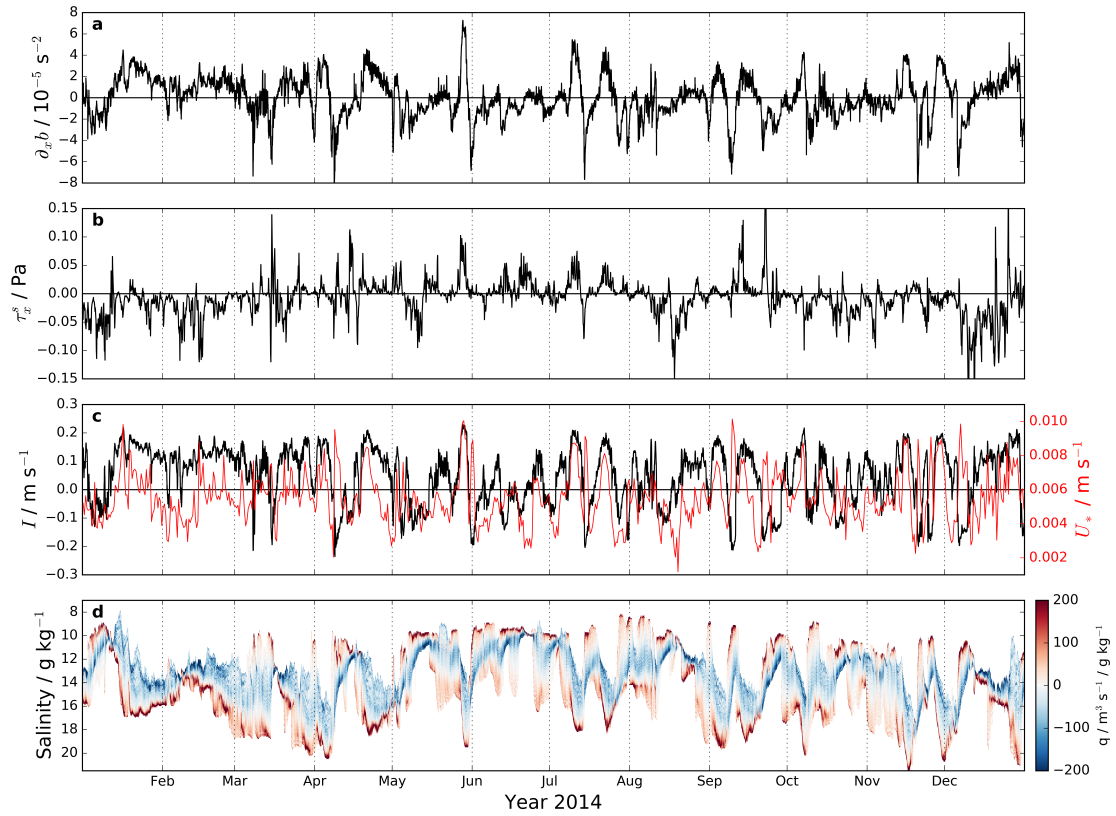
Figure 33: Transect averaged longitudinal buoyancy gradient (a), wind stress (b) and strength of estuarine circulation (black), as well as bottom friction velocity scale (red) (c) at the mouth of the Warnow estuary calculated with a numerical model. The corresponding volume flux per salinity class is shown in (d).

velocity profiles, resulting from the interaction of opposing wind straining and gravitational forcing. By considering situations in Fig. 32 with a certain number of zero crossings only the corresponding data points can be presented in the same Si-Ts parameter space as used above. The results show that several events follow the scheme of being located near the $\tilde{I} = 0$ isoline, but a large number of three-layered flow profiles can not be explained by the idealized theory of the former sections. Reason for this is that deviating from the stationary scenarios here highly transient conditions effect the exchange flow structure.
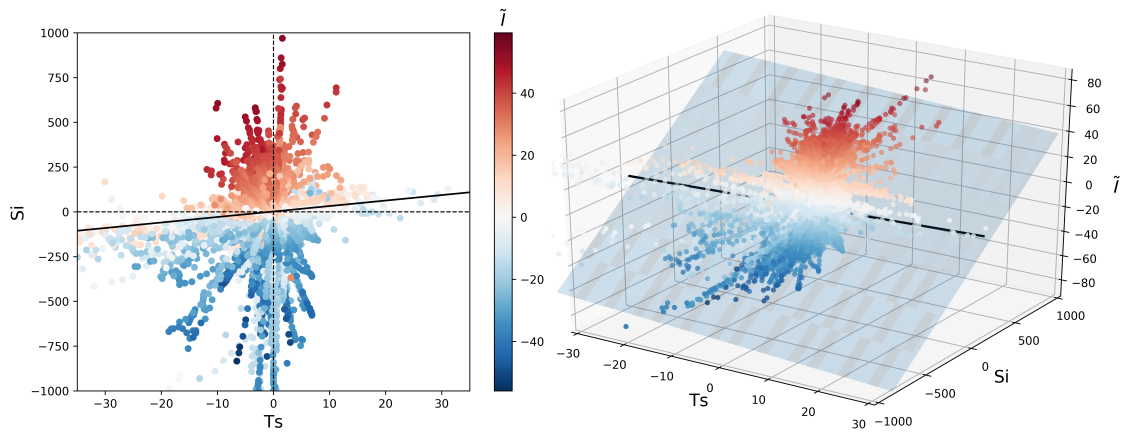
Figure 34: Strength of estuarine circulation $\tilde{I}$ dependent on varying Simpson number Si and non-dimensional wind stress Ts. The straight line indicates the critical condition $\tilde{I} = 0$ for the transition of classical circulation (red) to an inverted circulation (blue), obtained from a 3D planar regression (b).
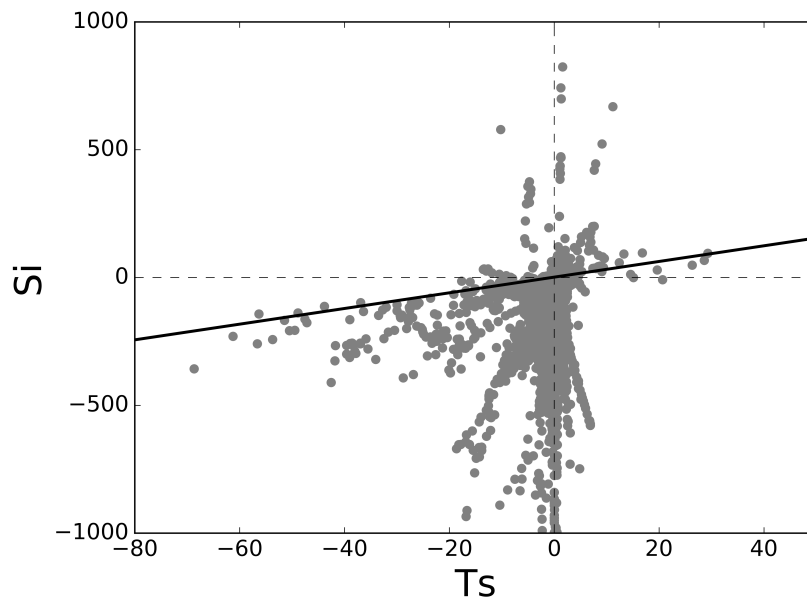
Figure 35: Data points representing three-layered velocity profiles in the Simpson number (Si) - non-dimensional wind stress (Ts) parameter space.

5.5 Mixing in the estuary

While the inflow volume flux only takes place in a small salinity range (Fig. 33), the outflow may extend over several salinity classes due to salinity mixing processes in the estuary. In order to estimate the degree of mixing for the Warnow estuary the inflow and outflow salinities for the transect at the mouth are consistently calculated in the TEF-framework by

$$s_{in} = \frac{F_{in}}{Q_{in}} \quad \text{and} \quad s_{out} = \frac{F_{out}}{Q_{out}}, \tag{40}$$

with the inflow and outflow salt flux F_{in} and F_{out} and volume flux Q_{in} and Q_{out}, respectively (MacCready, 2011; Geyer and MacCready, 2014; Burchard et al., 2018b):

$$F_{in|out} = \int s \left(-\partial_s Q\right)^{in|out} \mathrm{d}s \quad \text{and} \quad Q_{in|out} = \int \left(-\partial_s Q\right)^{in|out} \mathrm{d}s, \tag{41}$$

where the inflow contribution of a quantity λ is calculated as $(\lambda)^{in} = \max(\lambda, 0)$ and the outflow contribution as $(\lambda)^{out} = \min(\lambda, 0)$. Figure 36 shows the outflow salinity s_{out} in relation to the inflow salinity s_{in} calculated from the time series shown in Fig. 33d. Each data point represents a certain point in time in 2014 while the color code gives the respective strength of the exchange flow I (see Fig. 33c). Note that only two-layered flow profiles are considered here, since three-layered profiles would result in poorly interpretable values of s_{in} and s_{out}. The solid line represents a unity line, indicating equal values of inflow and outflow salinity, dividing the parameter space in two sections with I) $s_{out}/s_{in} < 1$ and II) $s_{out}/s_{in} > 1$.

Data points in Section II represent situations with water leaving the estuary having a higher salinity than water entering the estuary, which is the case when the circulation direction is reversed ($I < 0$ in blue) and high saline bottom water is transported seaward. In contrast to this, classical estuarine circulation ($I > 0$), with low saline surface water leaving the estuary, is represented by data shown in Section I in red. A linear regression through data points within a positive circulation, indicated as a dashed line, gives a relationship how the outflow salinity changes with respect to s_{in}. The slope of the regression has a value of $\frac{\partial s_{out}}{\partial s_{in}} = 0.83$ stating that the outflow salinity is about 83% of the inflow salinity. Another interpretation of this value is that the water in the surface layer at the mouth of the estuary consists to 83% of recirculated seawater.

In addition, a third meaning is given by the mixing completeness M_C: By analyzing a salinity variance budget MacCready et al. (2018) found that, when considering long-term averages, the temporally averaged and volume-integrated net mixing M
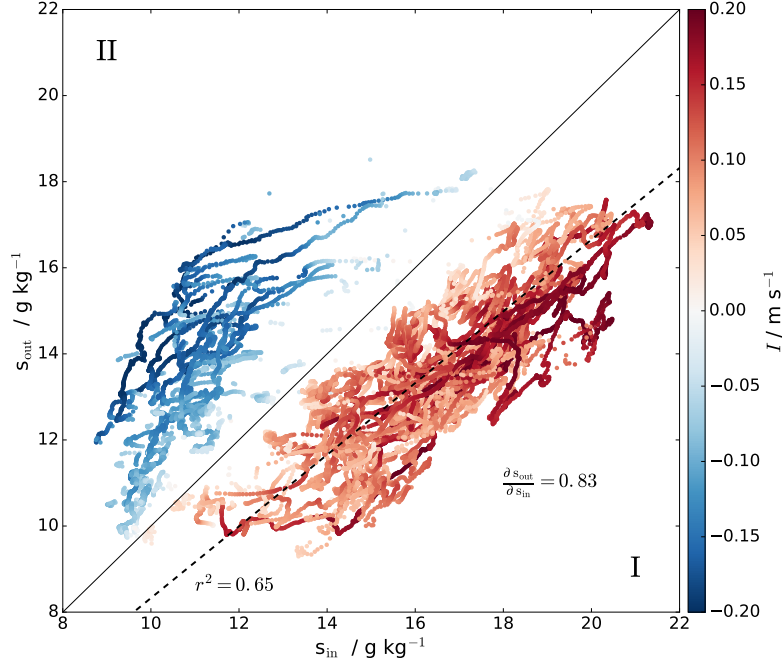
Figure 36: Relationship between outflow salinity s_{out} and inflow salinity s_{in} for classical (red) and reversed (blue) estuarine circulation, with the color code giving the corresponding strength of the exchange flow I. The dashed line is a linear regression through data points within a positive circulation and the solid line represents the unity condition $s_{out} = s_{in}$ for comparison.

in an estuary may be approximated as

$$M = 2 \left\langle \int K \left(\nabla s' \right)^2 dV \right\rangle \approx \langle s_{in} \rangle \langle s_{out} \rangle Q_r, \tag{42}$$

with the eddy diffusivity K, the local deviation from the estuarine-wide mean salinity $s' = s - \widehat{s}$ and the volume averaging operator $\widehat{\cdot}$ as defined in (2). Here, mixing is used as a measure for the rate of destruction of salinity variance $\widehat{s'^2}$. Based on (42), Burchard et al. (2018b) showed that for classical estuarine circulation the ratio of actual mixing to the maximum possible mixing $M_C = M/M_{max} = s_{in}s_{out}Q_r/s_{in}s_{in}Q_r = s_{out}/s_{in}$ estimates the mixing completeness of an estuary in terms of the inflow and outflow salinities. With this, the regression in Fig. 36 additionally represents the mixing completeness of the Warnow estuary at being about 83%.

The mean salinity $\widehat{s}$ introduced above has no spatial gradients (due to its definition) but is still a function of time (Fig. 37a). Its value is generally increasing in the presence of a positive circulation, since saline coastal bottom water is transported into the estuary, and decreases if the exchange flow reverses its direction ($I < 0$). This dependence of the estuarine-wide salinity on the strength of the exchange flow

highlights the applicability of I for system-wide descriptions even though it is calculated only for a transect at the mouth of the estuary.
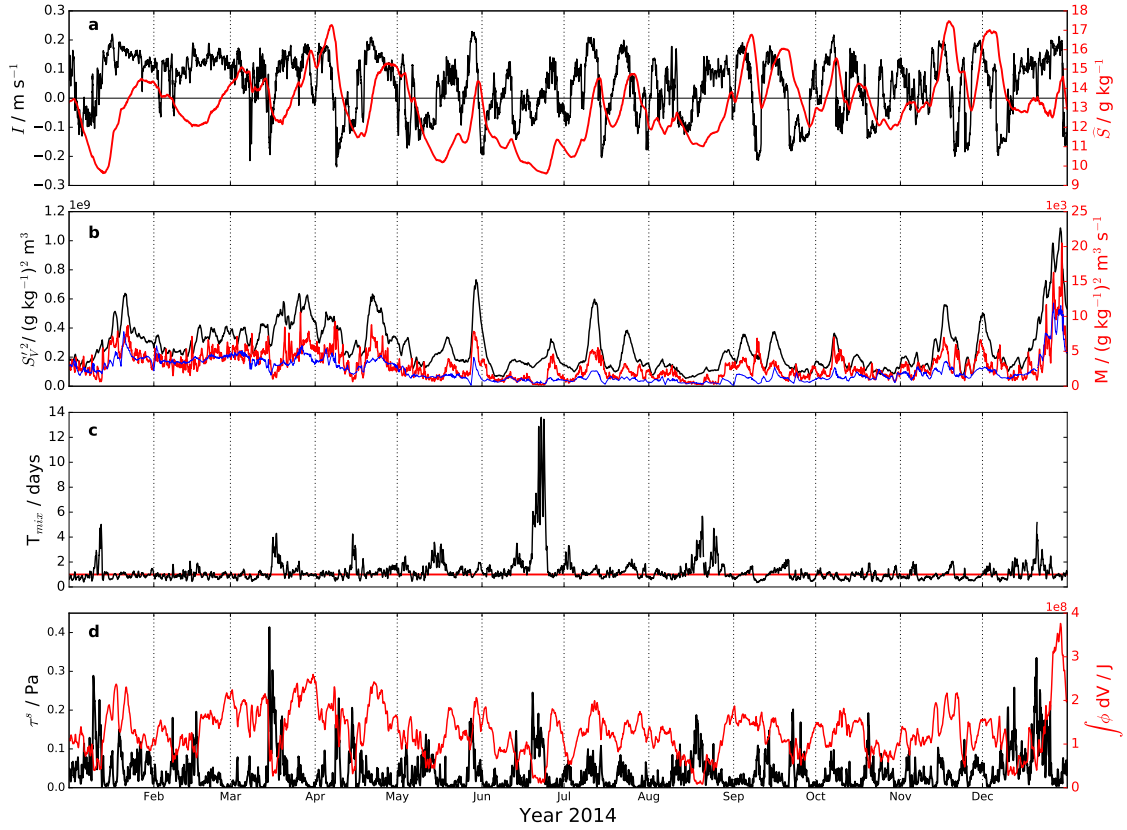
Figure 37: Mixing analysis for the Warnow estuary. a) Strength of total exchange flow I at the mouth in black and estuarine averaged salinity $\widehat{s}$ in red. b) Volume integrated salinity variance $S_V'^2$ (black) compared to total mixing in the estuary calculated by the numerical model (red) and by an analytical approximation (blue). c) Mixing timescale $S_V'^2/M$ in black and the 1day line for reference (red). d) Total surface stress τ^s (black) and the volume-integrated potential energy anomaly in red.

Besides the spatially averaged salinity $\widehat{s}$, its volume-integrated deviation represented by the total salinity variance $S_V'^2 = \int s'^2 \mathrm{d}V$ and the volume-integrated mixing M give insights into the estuarine dynamics (Fig. 37b). Here, the latter is calculated as the sum of numerical and physical mixing obtained from output of the mixing analyses in the numerical model (Klingbeil et al., 2014). The salinity variance increases e.g. due to inflow of high saline water (see also Fig. 27). The mixing increases as a result of local gradients in salinity variance and turbulence induced e.g. shear.

The ratio of total salinity variance $S_V'^2$ to total mixing M has the dimension of a timescale T_{mix}:

$$T_{mix} = \frac{S_V'^2}{M}, \tag{43}$$

which can be interpreted as the time needed to homogenize the estuarine-wide salinity distribution (Fig. 37b) by using the available mixing rate. Results show that the typical mixing timescale for the Warnow estuary is in the order of $T_{mix} \approx 1\,\text{d}$, (red line in Fig. 37c), which is exceeded at certain events during the year to $3-4$ days and in June even to $1-2$ weeks, resulting from small values of M (Fig. 37b). The reduced mixing can be explained by analyzing the density stratification in terms of the volume-integrated potential density anomaly ϕ, as defined in (18), representing the total energy needed to homogenize the individual water columns in the estuary vertically (Fig. 37d). Smaller values of ϕ indicate reduced stratification, suggesting that the water column is well-mixed locally (see Section 4.2.2). As a result, the values of M decrease, as already mixed water cannot be further mixed. The vertically low stratification at certain events coincides with larger values of wind stress (shown in red), indicating a decrease of ϕ due to wind-induced mixing. Note that the vertically mixed water may still have a horizontal salinity gradient (see also Fig. 30a) resulting in a still existing total salinity variance.

5.6 Conclusions

The results in this section describe the inversion of estuarine circulation in a weakly tidal estuary driven by i) an inverted salinity gradient and ii) along-estuary wind forcing. Even though the Warnow estuary is not exposed to strong evaporation the density gradient may reverse its direction, with the estuarine water temporally having a larger salinity than the seawater. This dynamics of alternating gradients can be explained as follows: In the presence of denser water in the near-coastal area of the study site classical estuarine circulation will transport saline water into the estuary, increasing the system-wide mean salinity $\hat{s}$ (Fig. 37a). This process is supported by the artificial shipping channel, which connects the Warnow estuary with dense water in the deeper layers of the Bay of Mecklenburg (Fig. 30d). If the ambient water is replaced by low saline brackish water of the Baltic Sea, the increased salinities in the estuary result in an inversed buoyancy gradient and thus in a reversed circulation direction (Fig. 33). In addition to that wind straining is found to invert the estuarine exchange flow: Similar to the results in section 3 and 4 the strength of the circulation $\tilde{I}$ can be presented in a parameter space spanned by the non-dimensional wind stress Ts and Simpson number Si. By applying a 3D regression the critical condition $\tilde{I} = 0$ is found for the transition from classical to inverted circulation with a basic Wedderburn number of $We_b = 0.33$ as calculated from its slope (Fig. 34). This indicates that the exchange flow is reversed, if the up-estuary non-dimensional wind forcing exceeds 33% of the non-dimensional gravitational forcing. This value is smaller than the basic Wedderburn number found for the tidal inlet in the Wadden Sea (60%), confirming former results that due to the missing tidal forcing the sensitivity of the estuary to wind stress increases. The results show that due to the interaction between along-estuary wind and density gradient forcing three-layered flow structures frequently occur (Fig. 35), which can be explained only partially by the analytical and numerical parameter studies in the former sections. When considering the salinities of the classical estuarine outflow and inflow, results show that both are proportional with increasing inflow s_{in} resulting in increased values of the outflow salinity s_{out}. An application of a least square regression leads to a relationship of $s_{out} = 0.83 \cdot s_{in}$ when considering long-term averages, stating that the outflow at the mouth consists of 83% recirculated seawater (Fig. 36). This value of 83% is found to be identical to the mixing completeness of the Warnow estuary as recently introduced by (MacCready et al., 2018) and (Burchard et al., 2018b) as the ratio of actual mixing to maximum possible mixing. The volume-integrated mixing itself shows a high temporal variability depending on stratification and locally available salinity variance (Fig. 37).

6 Summary and discussion

This study aims to answer the question of how along-estuary wind stress drives the exchange flow in estuaries in the presence of other forcing mechanisms. Especially the critical condition for wind induced inversion of the gravitational circulation, and other exchange flow enhancing effects, is of particular interest which raises the question of a parameter for characterizing the sensitivity of an estuary to wind stress. The latter should be independent of the state but be descriptive for a system allowing the comparison of different estuaries with respect to their response to wind.

a. Analytical solutions

In the present study analytical solutions describing the estuarine exchange flow are developed using a balance between the along-estuary pressure gradient force (baroclinic and barotropic) and a friction term as already proposed by Pritchard (1956). This simple but fundamental approach turns out to be analytically solvable if a tidally constant viscosity is applied and the buoyancy gradient is prescribed and set to a constant value. The latter is justified e.g. by tidal straining observations in Liverpool Bay carried out by Rippeth et al. (2001), which could be successfully reproduced by Simpson et al. (2002) using a 1D numerical model with constant gradients of salinity and temperature. By assuming constant lateral conditions, or treating the quantities as width-averaged over a cross-estuarine transect, the problem can be described by a one-dimensional equation for the longitudinal velocity profile $u(z)$. With this, analytical solutions for the along-estuary velocity profile can be found depending on the choice of turbulence parameterization. The simplest approach of a vertically constant eddy viscosity leads to a polynomial expression, well known as classical Hansen and Rattray (1965) solution. However, by applying a parabolic formulation instead, Burchard and Hetland (2010) derived a different velocity profile for the gravitational circulation with a logarithmic decrease near the bottom. Using the same parabolic parameterization an analytical solution, now additionally including wind forcing is newly derived, depending on the along-estuary wind stress. A comparison with results of a turbulence model (second order, k-ε) shows that the parabolic eddy viscosity leads to more realistic velocity profiles than the Hansen and Rattray (1965) solution (Fig. 6). The classical and the more realistic analytical solution have in common that the respective velocity profiles are added up by three contributions resulting from a horizontal buoyancy gradient (u_g), a residual flow velocity (u_r) and an along-channel wind stress (u_w). Gravitational forcing and wind forcing both lead to a two-layered flow structure, where a positive buoyancy gradient is found to drive classical estuarine circulation with a near-bottom landward current and a near-surface seaward flow. The same is true for down-estuary

64

(negative) wind stress, while the analytical solution suggests that an up-estuary wind leads to the same vertical structure but with a reversed sign, resulting in an inverted circulation direction. A disadvantage of the newly derived wind-driven profile u_w, when compared to the classical Hansen and Rattray (1965) solution, is that the velocity becomes infinite directly at the surface due to the parameterization of the viscosity being zero at the upper boundary. A modified formulation of the parabolic eddy viscosity, with a non-zero value at the surface (e.g. $A_v(z = \eta) = \kappa|u_*^s|z_0^s$), is found to lead to analytically non-solvable equations. Using an analytically vanishing viscosity at the surface can be interpreted as assuming a surface roughness length of $z_0^s = 0$, while the realistic numerical results make use of a dynamic formulation for the surface roughness depending on the surface friction velocity (Charnock, 1955):

$$z_0^s = a \left(u_*^s\right)^2 / g, \tag{44}$$

with the model constant $a = 1400$. When moving from realistic values with an order of magnitude of 10^{-2} m (e.g. for wind stress with $\tau^s = 0.1\,\text{Pa}$) to small values of 10^{-6} m, results show only a small sensitivity of the numerical strength of the wind-driven exchange flow $\tilde{I}$ (see Eq. (32)) with respect to the surface roughness length z_0^s (Fig. 38). In addition, further analysis of the results seems to be worthwhile
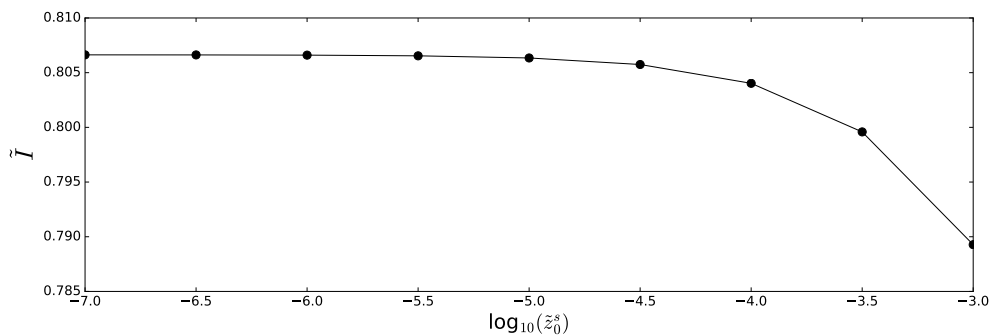
Figure 38: Resulting strength of estuarine circulation $\tilde{I}$ for seaward wind (Ts = -0.12, Si = 0) and varying prescribed non-dimensional surface roughness $\tilde{z}_0^s = z_0^s/H$. The results are calculated with a numerical turbulence model (second order, k-ε) using a water depth of $H = 10\,\text{m}$ and a tidal velocity amplitude of $U_t = 1\,\text{m\,s}^{-1}$ (Un = 0.04), see Section 4.

since the crucial properties of a vanishing vertical integral of u_w (no net transport due to the wind-driven exchange flow) and a zero slip at the bottom $u_w(-H, t) = 0$ are fulfilled and the vertical structure corresponds well with the numerical results (Fig. 6).

The analytical solution shows that the parameter space is comprehensively described by the Simpson number Si, the non-dimensional residual flow velocity $\tilde{U}_r$ and

the non-dimensional wind stress Ts when scaling the velocity profile with the bottom friction velocity scale U_*. Nevertheless, results show that the non-dimensional solution still slightly depends on the non-dimensional bottom roughness length $\tilde{z}_0^b$. The advantage of using U_* for scaling, instead of e.g. the tidal velocity amplitude U_t or the surface friction velocity u_*^s, is that the Simpson number is already included in the analytical solution and the newly appearing non-dimensional wind stress can be interpreted as the ratio of wind stress to bottom stress. Note that scaling with U_* and U_t could be transformed into each other via a quadratic drag coefficient, see Eq. (21).

In order to quantify the strength of the resulting estuarine circulation a measure $\tilde{I}$ based on the scaled along-estuary velocity is used, see Eq. (32). Here, a modified version suggested by Burchard et al. (2011) is applied, now including a weighting by the water depth when calculating transect averaged values. This measure has already proven its usefulness in other studies (e.g. Schulz et al., 2015; Purkiani et al., 2016). Using this formulation instead of the rms velocity (e.g. Weisberg and Sturges, 1976; Lerczak and Geyer, 2004) or the depth-averaged absolute velocity $\overline{|u|}$ (Burchard and Hetland, 2010) has the advantage that the total strength of the circulation is the sum of the individual contributions caused by the velocity terms u_g, u_r and u_w. Moreover, its value turns out to be sensitive to the sign of the velocity profiles thus allowing the indication of the direction of the circulation (classical or inversed). With this, classical estuarine circulation is described by $\tilde{I} > 0$ (*positive* circulation) and inversed estuarine circulation by $\tilde{I} < 0$ (*negative* circulation).

By using the realistic analytical solution for the velocity profile an analytical formulation for the strength of the estuarine circulation, depending on Si, Ts and $\tilde{U}_r$ can be derived (Eq. 33). In agreement to previous studies (e.g. Hansen and Rattray, 1965) it is found that the larger the ratio of buoyancy gradient forcing to tidal forcing (or Si in this case) is, the larger the resulting exchange flow will be (Fig. 7, Fig. 8) due to stronger gravitational circulation. In addition an inversed buoyancy gradient Si < 0 results in a negative circulation as observed in inverse estuaries (Johns et al., 2003; Nunes and Lennon, 1986). Seaward wind (Ts < 0) is found to increase the total exchange flow since the wind-induced near-bottom and near-surface currents are aligned with the flow caused by the gravitational circulation if Si > 0. On the contrary, landward wind (Ts > 0) decreases the estuarine circulation due to the counteracting current directions, agreeing with observations of Scully et al. (2005) in the York River estuary where up-estuary wind is found to reduce the total classical estuarine circulation.

The results suggest that an even stronger up-estuary wind is able to overcome the density-driven circulation resulting in a reversion of the exchange flow direction ($\tilde{I} < 0$). As a consequence the critical condition $\tilde{I} = 0$ serves as a measure for the

cancellation of gravitational forcing and wind forcing. The analytical condition for the critical wind stress necessary for cancellation turns out to be a simple linear relationship $\mathrm{Ts}_{crit} = A \cdot \mathrm{Si} + B \cdot \tilde{U}_r$, with A and B being constants slightly depending on $\tilde{z}_0^b$ (Fig. 9). With this, the slope of the $\tilde{I} = 0$ isoline in a Si-Ts parameter space diagram (wind being on the x-axis) is given by $1/A$. The analytical solution suggests that the constant factor A can be interpreted as a local Wedderburn number We = Ts/Si, as introduced by Purkiani et al. (2016), by dividing the critical wind stress by the Simpson number, motivating its designation here as basic Wedderburn number We$_b$. Its analytical value is found to be approximately 0.15 (Fig. 9), meaning that if the non-dimensional wind forcing exceeds 15 % of the non-dimensional gravitational forcing, the exchange flow reverses its direction. It turns out that additional residual flow, e.g. due to river discharge, shifts the $\tilde{I} = 0$ isoline horizontally in a way, that more wind is needed to invert the circulation but does not change its slope and thus the value of We$_b$ (Fig. 8c). Therefore, the basic Wedderburn number itself is not dependent on the state of the estuary but instead describes the sensitivity of an estuary to wind stress. Because We$_b$ is the result of a non-dimensional analyses, it can be used to compare different estuaries with respect to their behavior to wind.

b. Numerical parameter studies

The analytical solutions for the velocity and the resulting expression for the strength of the exchange flow have in common that their derivation assume a tidally constant eddy viscosity for simplicity (e.g. $A'_v = 0$) and thus do not include any feedback from a varying stratification. By doing so the eddy viscosity shear covariance $\langle A'_v \partial_z u' \rangle$ (ESCO, Dijkstra et al., 2017), resulting from a decomposition of quantities into a tidal mean and a tidally varying component, is neglected. Since this expression is known as a source term for driving estuarine circulation, originating from asymmetries between ebb and flood during a tidal cycle (Jay and Musiak, 1994), the analytical solutions miss a significant contribution of the tidal dynamics to the exchange flow. An evolving stratification and with this a tidally varying eddy viscosity profile are considered by application of a one-dimensional numerical turbulence model (second order, k-ε), but still with a prescribed constant horizontal buoyancy gradient (in terms of an along-estuary salinity gradient), wind stress and tidal velocity amplitude. As a non-dimensional measure for the tidal dynamics the Unsteadiness number Un proves to be useful as already successfully implemented in other studies (Burchard and Hetland, 2010; Burchard et al., 2011). The results show that the basic Wedderburn number increases for smaller values of Un (Fig. 12) with values of about We$_b \approx 0.45$ for typical tidal scenarios. When increasing Un (e.g. decreasing the tidal velocity amplitude) the basic Wedderburn number decreases to a value of approximately 0.15 which is in good agreement with the idealized steady-state

analytical solution derived in Section 3.3. As a consequence, up to three times more landward wind stress is necessary in the presence of tides to invert the classical estuarine circulation, compared to the non-tidal scenario solely driven by the buoyancy gradient. This result conforms with findings of Burchard and Hetland (2010) who showed that tidal straining may increase estuarine circulation in such a strong way, that 2/3 of the total exchange flow is contributed by this effect (and 1/3 contributed by the gravitational exchange flow itself).

It turns out that additionally including a residual flow velocity in the numerical simulation does not change the value of We_b but shifts the $\tilde{I} = 0$ isoline towards larger values of the up-estuary wind stress (Fig. 11), which is in agreement with findings of the analytical solution. This reinforces the hypothesis that the basic Wedderburn number is a robust measure for describing the sensitivity of an estuary to wind stress, since the tidal regime of an estuary is usually not a subject to strong variations (besides spring/neap tide modifications), but a characteristic and generally predictable property of a study site.

For down-estuary wind, Chen and Sanford (2009) hypothesize that there should be an optimal (negative) Wedderburn number at which down-estuarine wind forcing results in a maximum stratification. For weaker winds, the stratifying wind straining would be too small to generate maximum stratification, and for stronger winds, wind mixing would dominate over wind straining. Chen and Sanford (2009) estimated this optimal Wedderburn number for maximum stratification at a value of about $\mathrm{We}_o \approx -1$. The analytical stationary results are of no help when investigating this process, since the eddy viscosity parametrization does not depend on stratification and stratification is not calculated anyway (since it cannot be calculated analytically for parabolic eddy viscosity and diffusivity). For the dynamic one-dimensional scenario, the calculated tidally averaged stratification is a function of Ts and Si and thus a function of We and Si. From these parameter space plots it becomes obvious that the maximum stratification is reached for small negative local Wedderburn numbers. When the local Wedderburn number is further decreasing, stratification is decreasing as well, such that for these one-dimensional simulations the optimal local Wedderburn number for maximum stratification is of the order of $\mathrm{We}_o \approx -0.1$, a value which is much smaller than the value of $\mathrm{We}_o \approx -1$ estimated by Chen and Sanford (2009) for an idealized three-dimensional estuary. There are several explanations for this discrepancy: First of all, the experiments by Chen and Sanford (2009) were based on wind events of a duration of three days, while the experiments in Section 4 analyze tidally periodic states under constant wind forcing. Next, different estimates for the stratification are used in both studies. Furthermore, the two studies cover different parts of the parameter space, as this study focuses on tidally energetic estuaries while their study investigates partially mixed estuaries.

Such estuaries are excluded from the parameter study, since they cannot be represented by one-dimensional water column models due to the lack of feedback from estuarine circulation on the pressure gradient. With this, the results show that for the limit of strong and increasing down-estuary wind the exchange flow is increasing (Fig. 11), but stratification is decreasing (Fig. 13). A possible explanation is that down-estuary wind increases the tidal asymmetry in bed stress, adding a wind-related flood-oriented component to the flood dominance due to the gravitational forcing. Thus wind straining will increase estuarine exchange through the direct wind straining effect and the indirect effect of increasing tidal asymmetry in eddy viscosity and thus increasing ESCO. This seems to overcompensate the increased wind mixing effect. For the stratification, in turn, the increased estuarine exchange is the only enhancement mechanism, counteracted by the increased vertical mixing, which seems to be predominant for strong down-estuary wind.

The one-dimensional case-studies (analytical and numerical) are useful if considering lateral homogeneous flows e.g. caused by a flat bottom. More realistic scenarios include a laterally varying bathymetry which is known to cause secondary circulations (Lerczak and Geyer, 2004) and to increase ESCO (Burchard and Schuttelaars, 2012), both enhancing classical estuarine circulation. The results, obtained with a 2D numerical slice model of a cross-estuary transect, confirm that the steeper the parabolic bathymetry (larger ratio of water depth at the shoals to the depth at the center of the channel) the larger the ebb-flood asymmetry in the eddy viscosity (Fig. 15). Consequently, the ESCO-driven circulation and thus the total strength of the exchange flow $\tilde{I}$ increase without changing the underlying forcing. With this, the basic Wedderburn number is found to increase from 0.45 (flat bottom) to 1.3 (full parabolic) meaning that up to three times more longitudinal surface stress is needed to reverse the estuarine circulation, than compared to the amount in a tidal channel with flat bottom. The reason behind this is that up-estuary wind needs to additionally cancel the along-estuary exchange flow induced by the secondary circulations, besides the gravitational circulation and the effect of tidal straining.

When moving to a realistic three-dimensional estuarine system such as a tidal channel in the Wadden Sea, the analysis of the basic Wedderburn number becomes difficult due to the variability in the residual flow velocity. Careful analysis of the dynamics in the tidal channel of the Wadden Sea results in $\mathrm{We}_b = 0.6$, as shown in Fig. 20. This value is larger than the 1D analytical (0.15) and 1D dynamical (0.45) basic Wedderburn number but fits in the range found when additionally considering a laterally varying bathymetry (0.45 to 1.3). With this in addition to the influence of tides, effects of lateral circulation are supporting estuarine circulation in a way such that stronger up-estuarine wind (60 % of the gravitational forcing) is needed to neutralize the estuarine circulation. Note that the importance of lateral circulation

69

effects in this tidal channel has already been extensively investigated by Becherer et al. (2011) and Purkiani et al. (2015).

c. Application to a weakly tidal estuary

The former results suggest that in tidally energetic estuaries a large amount of the up-estuary wind forcing, needed for the inversion of estuarine circulation, is used up to compensate for the exchange flow induced by tidally-driven processes. However, the situation is different when studying an estuary with negligible tidal forcing. Here, the Warnow estuary in the south-western Baltic Sea is used exemplarily as a prototype for such a weakly tidal estuary. Spectral analyses of the sea level show a tidal range of about $8\,\mathrm{cm}$ suggesting that tidal forcing plays only a minor role in driving estuarine circulation, which reduces the governing mechanisms to wind straining and buoyancy gradient forcing including the resulting effects of stratification and mixing. Results show that the formation of the buoyancy gradient in the estuary is driven by various processes (see Section 5.4). Large-area temperature observations in the western Baltic Sea, obtained from satellite data, as well as local offshore time series of salinity measurements suggest that the study site is exposed to strong changes in the water body, alternating between relatively high saline water and low saline brackish water originating from the North Sea and the Baltic Sea, respectively. This is confirmed by model results for the sea surface salinity in the western Baltic Sea, showing a steadily declining salinity when moving eastward (Fig. 29), but an uneven distribution in temporal salinity variance. While the eastern parts show only a small variance ($\leq 2\,(\mathrm{g/kg})^2$), increased values are found near the study side ($\approx 8\,(\mathrm{g/kg})^2$) and even larger variances when considering the Danish Streets ($> 20\,(\mathrm{g/kg})^2$), indicating temporal unsteady salinities. Offshore time series of salinity measurements at the surface ($2\,\mathrm{m}$) and at mid-depth ($12\,\mathrm{m}$) identify two possible mechanisms for an increase in salinity in the near-estuary coastal water. On the one hand an increase in salinity near the surface coupled with an increase at mid-depth can be explained by horizontal advection of vertically mixed water. On the other hand, a salinity increase in mid-depth but without changes in the surface layer indicates an inflow of saline water in deeper layers. The latter increases the salinity either actively by replacing the mid-depth water or passively as a near-bottom inflow and a resulting uplift of the isopycnals into mid-depth. Since the estuary is hydrologically connected with this mid-depth layer due to the artificial shipping channel having a depth of about $15\,\mathrm{m}$, both processes potentially lead to an increase in salinity in the estuary when estuarine circulation transports the saline bottom water landward. In addition, as a third process coastal upwelling is found to increase the near-coast salinity (Fig. 30). With this, the seawater salinity in front of the estuary is found to be highly variable due to its location between the

North Sea to the west and the central Baltic Sea to the east. In times of water with high salinity in front of the estuary the results show that the buoyancy gradient is generally positive resulting in a classical circulation transporting the saline bottom seawater into the estuary and therefore increasing the salinity in the estuary (see also Fig. 37a). When the saline coastal water is replaced by the brackish water of the Baltic Sea the density gradient at the mouth of the estuary is found to reverse its direction, since the salinity of the riverine water is still increased by the former influx of saline coastal water. This suggests that in the Warnow estuary the salinity gradient can be temporally reversed similar to inverse estuaries found in arid regions (Nunes and Lennon, 1986; Johns et al., 2003). Contrary to the latter the cause here is not strong evaporation but the storage of salt in the estuary in combination with the water exchange time of the estuary (flushing time ≈ 30 days) being larger than the time scale of changes in the ambient water, which can be in the order of $1-2$ days (Fig. 28c).

When further analyzing the density gradient and wind forcing in terms of Simpson number Si and non-dimensional wind stress Ts at the mouth of the river, it turns out that due to the missing tides the bottom friction velocity scale is much smaller ($\sim 10^{-3}\,\mathrm{m\,s^{-1}}$) than in tidally energetic estuaries ($\sim 10^{-2}\,\mathrm{m\,s^{-1}}$), leading to unusual large values of Si, Ts and $\tilde{I}$. Note that the Simpson number was originally introduced for studying tidal mixing in estuaries (Simpson et al., 1990). Nevertheless, the method of calculating the basic Wedderburn number in the Si-Ts parameter space, as proposed by the analytical solution and confirmed by the numerical parameter studies, turns out to still be valid. When using the same surface regression method as successfully applied for the 3D Sylt-scenario, the basic Wedderburn number results in $\mathrm{We}_b \approx 0.33$ for the Warnow estuary (Fig. 34). This is only half of the value found for the tidal inlet in the Wadden Sea ($\mathrm{We}_b \approx 0.6$) and even smaller than the dynamic 1D model result ($\mathrm{We}_b \approx 0.45$), but larger than the stationary analytical and dynamic non-tidal solution ($\mathrm{We}_b \approx 0.15$). A possible reason for this is that even in the absence of tidal forcing, wind straining still has to counter effects induced by lateral processes in addition to the gravitational circulation. The smaller basic Wedderburn number indicates that the exchange flow in the weakly tidal estuary is more sensitive with respect to wind stress than the estuarine circulation in the tidal energetic inlet.

These results show that an inversion of estuarine circulation in the Warnow estuary can occur in several ways: (i) inversion due to an inversed buoyancy gradient resulting from varying coastal waters, (ii) inversion due to up-estuary wind straining resulting from a relative high sensitivity of the estuary to wind forcing and (iii) inversion of the inversed circulation resulting in a classical exchange flow. The latter is the case when down-estuary wind forcing drives a positive circulation even though

the buoyancy gradient is reversed. This complex interaction of gravitational circulation and wind forcing, both with varying signs, is found to result in three-layered velocity profiles (Fig. 10, Fig. 14) when counting the number of zero-crossings. The analytical solution for the velocity profile indicates that this multi-layered flow structure occurs in a transition zone between classical and inversed estuarine circulation with the $\tilde{I} = 0$ isoline being the bisector. Based on this, the velocity profiles can be assigned to five distinct flow classes (Fig. 14) as confirmed by the 1D numerical simulations. However, when considering the three-layered events in the Warnow estuary the results are less conclusive. A variety of these scenarios are located around the $\tilde{I} = 0$ isoline, which is in agreement with the former results, but several data points do not comply with this schema. A possible reason for this is that the residual flow velocity additionally contributes to the vertical velocity structure, which is not considered in the analytical and numerical parameter study. Moreover, the residual flow is found to shift the $\tilde{I} = 0$ isoline (Fig. 11c, Fig. 8c) and with this potentially the position of the three-layered exchange flow in the Si-Ts parameter space.

When considering long term averages of inflow and outflow salinity, resulting from the exchange flow and mixing in the estuary, it turns out that they change proportionally with increasing inflow salinity causing an increase in the outflow salinity. The proportionality factor of 83 % suggests that the outflowing water consists to 83 % of recirculated seawater and 17 % of freshwater discharge, respectively. Recent salinity mixing theories by MacCready et al. (2018) and Burchard et al. (2018b) suggest that this factor additionally represents the mixing completeness (ratio of actual mixing to maximum possible mixing) of the estuary. The mixing completeness of 83 % is larger than values calculated by Burchard et al. (2018b) for the Baltic Sea ($Mc = 54\%$). Making use of an idealized estuary with tidal forcing, MacCready et al. (2018) recently showed that the mixing completeness in their study varied between 95 % and 62 % during spring and neap tide, respectively. As pointed out by MacCready et al. (2018), more estuaries have to be studied in terms of this new mixing approach in order to put these numbers into context.

However, the results in Section 5 show that the volume-integrated mixing, the volume-averaged salinity and the volume-integrated salinity variance are highly variable over time. The comparison of the volume-integrated mixing (i) obtained by the numerical model and (ii) calculated using the simple relation $M_{tot} \approx \langle s_{in} \rangle \langle s_{out} \rangle Q_r$ proposed by MacCready et al. (2018), shows largely good agreement even though the latter is originally based on long-term averages. Deviations between the exact and the analytically calculated mixing can be explained by the fact that the simple analytical formulation neglects various processes, such as e.g. storage of volume and salt as identified by Burchard et al. (2018b). When calculating the mixing timescale as the ratio of total salinity variance to total mixing, the results are in the order of

one day for the Warnow estuary. This value is found to increase if the total mixing decreases. A possible reason for the decreased mixing during certain events is an already vertically homogenized water column as indicated by small values of the volume-integrated potential energy anomaly. The latter coincides with increased values of surface stress, suggesting that the estuary is mixed vertically due to wind and thus decreased in stratification, while still existing horizontal density gradients result in spatial salinity variance.

7 Conclusions

The strength of the estuarine exchange flow $\tilde{I}$ can be formulated analytically using an analytical solution for the along-estuary velocity profile with a parabolic eddy viscosity. With this, the estuarine circulation can be described in a parameter space spanned by the Simpson number Si and the non-dimensional wind stress Ts. Cancellation of gravitational forcing and wind forcing is described as the critical condition $\tilde{I} = 0$. The reciprocal value of its slope, the basic Wedderburn number We_b, is found to be a promising parameter for drawing comparisons and may classify different estuaries regarding to their sensitivity to wind stress, since its value is largely independent of the state of the estuary. Results show that the more processes are involved in driving the exchange flow, the more up-estuary wind is necessary to invert the circulation. For realistic applications, with possibly highly variable subtidal residual flow velocities, a planar regression in the Si-Ts parameter space has proven to be useful in determining the basic Wedderburn number as used exemplarily for a tidally energetic inlet ($\text{We}_b \approx 0.6$) and a weakly tidal estuary ($\text{We}_b \approx 0.3$). The results underline the importance of the alignment of the estuary with respect to the prevailing wind directions.

Unanswered is the question which non-dimensional parameter may describe the dynamics driven by gravitational forcing in weakly tidal estuaries, since the Simpson number turns out to be unusually large as a consequence of small bottom friction velocities. A promising candidate might be the reciprocal Wedderburn number $1/\text{We} = \text{Si}/\text{Ts} = \partial_x b H^2 / u_*^s |u_*^s| = \text{Si}^*$ which may be interpreted as a modified Simpson number using the surface friction velocity scale. In addition, more research is necessary for understanding three-layered velocity structures in realistic applications even though the theoretical results obtained from the analytical and numerical parameter studies may point in the right direction. One possible approach would be to consider residual flow corrected velocity profiles ($\tilde{u}^* = \tilde{u} - \tilde{U}_r$) in the future when studying exchange flows in the Si-Ts parameter space. Investigating additional estuaries would be helpful in setting the mixing completeness in a broader context, which is also true for the basic Wedderburn number and the estuarine mixing time scale T_{mix}. The latter raises the question whether time values of one day, as found for the Warnow estuary, are typical of certain types of estuaries.

References

Barsi, J. A., Barker, J. L., and Schott, J. R. (2003). An Atmospheric Correction Parameter Calculator for a single thermal band earth-sensing instrument. *IEEE International Geoscience and Remote Sensing Symposium 2003*, 00:2–4.

Becherer, J., Burchard, H., Flöser, G., Mohrholz, V., and Umlauf, L. (2011). Evidence of tidal straining in well-mixed channel flow from micro-structure observations. *Geophys. Res. Lett.*, 38:2–6.

Becherer, J., Stacey, M. T., Umlauf, L., and Burchard, H. (2015). Lateral Circulation Generates Flood Tide Stratification and Estuarine Exchange Flow in a Curved Tidal Inlet. *Journal of Physical Oceanography*, 45:638–656.

Buer, A. L., Gyraite, G., Wegener, P., Lange, X., Katarzyte, M., Hauk, G., and Schernewski, G. (2018). Long term development of Bathing Water Quality at the German Baltic coast: spatial patterns, problems and model simulations. *Marine Pollution Bulletin*, 135:1055–1066.

Burchard, H. (2009). Combined Effects of Wind, Tide, and Horizontal Density Gradients on Stratification in Estuaries and Coastal Seas. *Journal of Physical Oceanography*, 39:2117–2136.

Burchard, H. and Baumert, H. (1998). The Formation of Estuarine Turbidity Maxima Due to Density Effects in the Salt Wedge. A Hydrodynamic Process Study. *Journal of Physical Oceanography*, 28:309–321.

Burchard, H. and Bolding, K. (2002). Three-dimensional modelling of estuarine turbidity maxima in a tidal estuary. *Technical Report EUR 20253 EN. Tech. rep., European Commission.*

Burchard, H., Bolding, K., Feistel, R., Gräwe, U., Klingbeil, K., MacCready, P., Mohrholz, V., Umlauf, L., and van der Lee, E. M. (2018a). The Knudsen theorem and the Total Exchange Flow analysis framework applied to the Baltic Sea. *Progress in Oceanography*, 165:268–286.

Burchard, H., Flöser, G., Staneva, J. V., Badewien, T. H., and Riethmüller, R. (2008). Impact of density gradients on net sediment transport into the WaddenSea. *Journal of Physical Oceanography*, 38:566–589.

Burchard, H. and Hetland, R. D. (2010). Quantifying the Contributions of Tidal Straining and Gravitational Circulation to Residual Circulation in Periodically Stratified Tidal Estuaries. *Journal of Physical Oceanography*, 40:1243–1262.

Burchard, H., Hetland, R. D., Schulz, E., and Schuttelaars, H. M. (2011). Drivers of Residual Estuarine Circulation in Tidally Energetic Estuaries: Straight and Irrotational Channels with Parabolic Cross Section. *Journal of Physical Oceanography*, 41:548–570.

Burchard, H. and Hofmeister, R. (2008). A dynamic equation for the potential energy anomaly for analysing mixing and stratification in estuaries and coastal seas. *Estuarine, Coastal and Shelf Science*, 77:679–687.

Burchard, H., Janssen, F., Bolding, K., Umlauf, L., and Rennau, H. (2009). Model simulations of dense bottom currents in the Western Baltic Sea. *Continental Shelf Research*, 29:205–220.

Burchard, H., Lange, X., Klingbeil, K., and Maccready, P. (2018b). Mixing estimates for estuaries. *Journal of Geophysical Research:Oceans*. revised.

Burchard, H., Schulz, E., and Schuttelaars, H. M. (2014). Impact of estuarine convergence on residual circulation in tidally energetic estuaries and inlets. *Geophysical Research Letters*, 41:913–919.

Burchard, H. and Schuttelaars, H. M. (2012). Analysis of Tidal Straining as Driver for Estuarine Circulation in Well-Mixed Estuaries. *Journal of Physical Oceanography*, 42:261–271.

Burchard, H., Schuttelaars, H. M., and Geyer, W. R. (2013). Residual Sediment Fluxes in Weakly-to-Periodically Stratified Estuaries and Tidal Inlets. *Journal of Physical Oceanography*, 43:1841–1861.

Cameron, W. M. and Pritchard, D. W. (1963). Estuaries. *In M. N. Hill (editor), The Sea, Vol. 2. John Wiley & Sons, New York*, pages 306–324.

Chant, R. J. (2002). Secondary circulation in a region of flow curvature: Relationship with tidal forcing and river discharge. *Journal of Geophysical Research*, 107:14:1–14:11.

Charnock, H. (1955). Wind stress on a water surface. *Quarterly Journal of the Royal Meteorological Society*, 81:639–640.

Chatwin, P. C. (1976). Some remarks on the maintenance of the salinity distribution in estuaries. *Estuarine and Coastal Marine Science*, 4:555–566.

Chen, S.-N. and Sanford, L. P. (2009). Axial Wind Effects on Stratification and Longitudinal Salt Transport in an Idealized, Partially Mixed Estuary. *Journal of Physical Oceanography*, 39:1905–1920.

Cheng, Y., Canuto, V. M., and Howard, A. M. (2002). An Improved Model for the Turbulent PBL. *Journal of the Atmospheric Sciences*, 59:1550–1565.

Dijkstra, Y. M., Schuttelaars, H. M., and Burchard, H. (2017). Generation of exchange flows in estuaries by tidal and gravitational eddy viscosity-shear covariance (esco). *Journal of Geophysical Research:Oceans*, 122:4217–4237.

Enders, K., Käppler, A., Biniasch, O., Stollberg, N., Lange, X., Fischer, D., Eichhorn, K.-J., Pollehne, F., Oberbeckmann, S., and Labrenz, M. (2019). Tracing microplastics in aquatic environments based on sediment analogies. submitted.

Geyer, W. R. (1993). Three-dimensional tidal flow around headlands. *Journal of Geophysical Research*, 98:955–966.

Geyer, W. R. (1997). Influence of Wind on Dynamics and Flushing of Shallow Estuaries. *Estuarine, Coastal and Shelf Science*, 44:713–722.

Geyer, W. R. and MacCready, P. (2014). The Estuarine Circulation. *Annual Review of Fluid Mechanics*, 46:175–197.

Geyer, W. R. and Ralston, D. K. (2015). Estuarine frontogenesis. *Journal of Physical Oceanography*, 45:546–561.

Gräwe, U., Flöser, G., Gerkema, T., Duran-Matute, M., Badewien, T. H., Schulz, E., and Burchard, H. (2016). A numerical model for the entire Wadden Sea: Skill assessment and analysis of hydrodynamics. *Journal of Geophysical Research: Oceans*, 121:5231–5251.

Gräwe, U., Holtermann, P., Klingbeil, K., and Burchard, H. (2015). Advantages of vertically adaptive coordinates in numerical models of stratified shelf seas. *Ocean Modelling*, 92:56–68.

Gräwe, U., Naumann, M., Mohrholz, V., and Burchard, H. (2015). Anatomizing one of the largest saltwater inflows into the Baltic Sea in December 2014. *Journal of Geophysical Research: Oceans*, 120:7676–7697.

Gräwe, U. and Wolff, J.-O. (2010). Suspended particulate matter dynamics in a particle framework. *Environmental Fluid Mechanics*, 10:21–39.

Hansen, D. V. and Rattray, M. (1965). Gravitational circulation in straits and estuaries. *Journal of Marine Research*, 23:104–122.

Hetland, R. D. and Geyer, W. R. (2004). An Idealized Study of the Structure of Long, Partially Mixed Estuaries. *Journal of Physical Oceanography*, 34:2677–2691.

Hofmeister, R., Burchard, H., and Beckers, J.-M. (2010). Non-uniform adaptive vertical grids for 3d numerical ocean models. *Ocean Modelling*, 33:70–86.

Holtermann, P. L., Burchard, H., Gräwe, U., Klingbeil, K., and Umlauf, L. (2014). Deep-water dynamics and boundary mixing in a nontidal stratified basin: A modeling study of the Baltic Sea. *Journal of Geophysical Research: Oceans*, 119:1465–1487.

Hosseini, S. T. and Siadatmousavi, S. M. (2018). Field observations of hypersaline runoff through a shallow estuary. *Estuarine, Coastal and Shelf Science*, 202:54–68.

Ianniello, J. P. (1979). Tidally Induced Residual Currents in Estuaries of Variable Breadth and Depth. *Journal of Physical Oceanography*, 9:962–974.

Jay, D. A. and Musiak, J. D. (1994). Particle trapping in estuarine tidal flows. *J. Geophys. Res.*, 99:445–461.

Johns, W. E., Yao, F., Olson, D. B., Josey, S. A., Grist, J. P., and Smeed, D. A. (2003). Observations of seasonal exchange through the Straits of Hormuz and the inferred heat and freshwater budgets of the Persian Gulf. *Journal of Geophysical Research*, 108:21:1–21:18.

Klingbeil, K., Becherer, J., Schulz, E., de Swart, H. E., Schuttelaars, H. M., Valle-Levinson, A., and Burchard, H. (2018). Thickness-Weighted Averaging in tidal estuaries and the vertical distribution of the Eulerian residual transport. *Journal of Physical Oceanography*. revised.

Klingbeil, K., Mohammadi-Aragh, M., Gräwe, U., and Burchard, H. (2014). Quantification of spurious dissipation and mixing – Discrete Variance Decay in a Finite-Volume framework. *Ocean Modelling*, 81:49–64.

Knudsen, M. (1900). Ein hydrographischer Lehrsatz. *Hydrogr. Mar. Meteorol.*, 28:316–320.

Lange, X. and Burchard, H. (2019). The relative importance of wind straining and gravitational forcing in driving exchange flows in tidally energetic estuaries. *Journal of Physical Oceanography*. accepted.

Large, W. G. and Pond, S. (1981). Open Ocean Momentum Flux Measurements in Moderate to Strong Winds. *Journal of Physical Oceanography*, 11:324–336.

Lerczak, J. A. and Geyer, W. R. (2004). Modeling the lateral circulation in straight, stratified estuaries. *Journal of Physical Oceanography*, 34:1410–1428.

Linden, P. F. (1979). Mixing in Stratified Fluids. *Geophysical & Astrophysical Fluid Dynamics*, 13:3–23.

Linden, P. F. and Simpson, J. E. (1988). Modulated mixing and frontogenesis in shallow seas and estuaries. *Continental Shelf Research*, 8:1107–1127.

Lun, I. Y. F. and Lam, J. C. (2000). A study of Weibull parameters using long-term wind observations. *Renewable Energy*, 20:145–153.

MacCready, P. (2011). Calculating estuarine exchange flow using isohaline coordinates. *Journal of Physical Oceanography*, 41:1116–1124.

MacCready, P. and Geyer, W. R. (2010). Advances in estuarine physics. *Annual review of marine science*, 2:35–58.

MacCready, P., Geyer, W. R., and Burchard, H. (2018). Estuarine Exchange Flow Is Related to Mixing through the Salinity Variance Budget. *Journal of Physical Oceanography*, 48:1375–1384.

Matthäus, W. and Schinke, H. (1999). The influence of river runoff on deep water conditions of the Baltic Sea. *Hydrobiologia*, 393:1–10.

McGregor, R. C. (1972). The Influence of Eddy Viscosity on the Vertical Distribution of Velocity in the Tidal Estuary. *Geophysical Journal*, 29:103–108.

Monismith, S. (1986). An experimental study of the upwelling response of stratified reservoirs to surface shear stress. *Journal of Fluid Mechanics*, 171:407–439.

Monismith, S. G., Burau, J. R., and Stacey., M. T. (1996). Stratification Dynamics and Gravitational Circulation in Northern San Francisco Bay. *San Francisco Bay: The Ecosystem. Ecosystem, J. T. Hollibaugh, Ed.*, (American Association for the Advancement of Science):123–153.

Mortensen, N. A., Okkels, F., and Bruus, H. (2005). Reexamination of Hagen-Poiseuille flow: Shape dependence of the hydraulic resistance in microchannels. *Physical Review E - Statistical, Nonlinear, and Soft Matter Physics*, 71:1–4.

Nunes, R. and Lennon, G. W. (1986). Physical Property Distributions and Seasonal Trends in Spencer Gulf, South Australia: an Inverse Estuary. *Australian Journal of Marine and Freshwater Research*, 37:39–53.

Nunes, R. and Simpson, J. H. (1985). Axial convergence in a well- mixed estuary. *Estuarine, Coastal and Shelf Science*, 20:637–649.

Pritchard, D. (1952a). Estuarine hydrography. *Advances in Geophysics*, 1:243–280.

Pritchard, D. (1952b). Salinity distribution and circulation in the Chesapeake Bay estuarine system. *Journal of Marine Research*, 11:106–123.

Pritchard, D. (1954a). A study of flushing in The Delaware Model. *The Chesapeake Bay Institute, The Johns Hopkins University, Tech. Rept. VII, Reference 54-4*, page 143 pp.

Pritchard, D. (1954b). A study of the salt balance in a coastal plain estuary. *Journal of Marine Research*, 13:133—144.

Pritchard, D. (1956). The dynamic structure of a coastal plain estuary. *Journal of Marine Research*, 15:33–42.

Purkiani, K., Becherer, J., Flöser, G., Gräwe, U., Mohrholz, V., Schuttelaars, H. M., and Burchard, H. (2015). Numerical analysis of stratification and de-stratification processes in a tidally energetic inlet with an ebb tidal delta. *J. Geophys. Res.*, 120:225–243.

Purkiani, K., Becherer, J., Klingbeil, K., and Burchard, H. (2016). Wind-induced variability of estuarine circulation in a tidally energetic inlet with curvature. *J. Geophys. Res.*, 121:3261–3277.

Ralston, D. K., Geyer, W. R., and Lerczak, J. A. (2008). Subtidal Salinity and Velocity in the Hudson River Estuary: Observations and Modeling. *Journal of Physical Oceanography*, 38:753–770.

Rippeth, T. P., Fisher, N. R., and Simpson, J. H. (2001). The cycle of turbulent dissipation in the presence of tidal straining. *Journal of Physical Oceanography*, 31:2458–2471.

Sassi, M. G., Duran-Matute, M., van Kessel, T., and Gerkema, T. (2015). Variability of residual fluxes of suspended sediment in a multiple-inlet system: the Dutch Wadden Sea. *Ocean Dynamics*, 65:1321–1333.

Schiele, K. S., Darr, A., Zettlr, M. L., Friedland, R., Tauber, F., Weber, M. v., and Voss, J. (2015). Biotope map of the German Baltic Sea. *Marine Pollution Bulletin*, 96:127–135.

Schulz, E., Schuttelaars, H. M., Gräwe, U., and Burchard, H. (2015). Impact of the Depth-to-Width Ratio of Periodically Stratified Tidal Channels on the Estuarine Circulation. *Journal of Physical Oceanography*, 45:2048–2069.

Scully, M. E., Friedrichs, C., and Brubaker, J. (2005). Control of estuarine stratification and mixing by wind-induced straining of the estuarine density field. *Estuaries*, 28:321–326.

Scully, M. E. and Friedrichs, C. T. (2007). The Importance of Tidal and Lateral Asymmetries in Stratification to Residual Circulation in Partially Mixed Estuaries. *Journal of Physical Oceanography*, 37:1496–1511.

Simpson, J. H. (1981). The Shelf-Sea Fronts: Implications of their Existence and Behaviour. *Philosophical Transactions of the Royal Society of London. Series A*, 302:531–546.

Simpson, J. H., Brown, J., Matthews, J., and Allen, G. (1990). Tidal Straining, Density Currents, and Stirring in the Control of Estuarine Stratification. *Estuaries*, 13:125–132.

Simpson, J. H., Burchard, H., Fisher, N. R., and Rippeth, T. P. (2002). The semi-diurnal cycle of dissipation in a rofi: Model-measurement comparisons. *Continental Shelf Research*, 22:1615–1628.

Smith, R. (1976). Longitudinal dispersion of a buoyant contaminant in a shallow channel. *Journal of Fluid Mechanics*, 78:677–688.

Stacey, M. T. (1996). Turbulent mixing and residual circulation in a partially stratified estuary. *PhD diss. Stanford Univ., Stanford, CA.*, page 209pp.

Stacey, M. T., Brennan, M. L., Burau, J. R., and Monismith, S. G. (2010). The Tidally Averaged Momentum Balance in a Partially and Periodically Stratified Estuary. *Journal of Physical Oceanography*, 40:2418–2434.

Stacey, M. T., Burau, J. R., and Monismith, S. G. (2001). Creation of residual flows in a partially stratified estuary. *Journal of Geophysical Research*, 106:13–17.

Stacey, M. T., Fram, J. P., and Chow, F. K. (2008). Role of tidally periodic density stratification in the creation of estuarine subtidal circulation. *Journal of Geophysical Research: Oceans*, 113:1–13.

Umlauf, L. and Burchard, H. (2005). Second-order turbulence closure models for geophysical boundary layers. A review of recent work. *Continental Shelf Research*, 25:795–827.

Valle-Levinson, A. (2010). *Definition and classification of estuaries*, page 1–11. Cambridge University Press.

Valle-Levinson, A. (2011). 1.05 - classification of estuarine circulation. In Wolanski, E. and McLusky, D., editors, *Treatise on Estuarine and Coastal Science*, pages 75 – 86. Academic Press, Waltham.

van Aken, H. M. (1986). The onset of seasonal stratification in shelf seas due to differential advection in the presence of a salinity gradient. *Continental Shelf Research*, 5:475–485.

Verspecht, F., Rippeth, T. P., Howarth, M. J., Souza, A. J., Simpson, J. H., and Burchard, H. (2009). Processes impacting on stratification in a region of freshwater influence: Application to Liverpool Bay. *Journal of Geophysical Research: Oceans*, 114:1–12.

Wang, T., Geyer, W. R., and MacCready, P. (2017). Total Exchange Flow, Entrainment, and Diffusive Salt Flux in Estuaries. *Journal of Physical Oceanography*, 47:1205–1220.

Weisberg, R. H. (1976). The nontidal flow in the Province River of Narragansett Bay: a stochastic approach to estuarine circulation. *Journal of Physical Oceanography*, 6:721–734.

Weisberg, R. H. and Sturges, W. (1976). Velocity Observations in the West Passage of Narragansett Bay: A Partially Mixed Estuary. *Journal of Physical Oceanography*, 6:345–354.

Wolanksi, E. (1986). An evaporation-driven salinity maximum zone in Australian tropical estuaries. *Estuarine, Coastal and Shelf Science*, 22:415–424.

A Flushing time in the Warnow estuary

In order to estimate the time necessary for an almost complete water exchange in the Warnow estuary, the numerical setup in Section 5.3 is combined with the Framework for Aquatic Biogeochemical Models (FABM), providing methods for modeling additional numerical tracers. For that, the estuary is monthly initialized with a homogeneously distributed passive tracer (without feedback on the density) representing the initial riverine water (Fig. 39). Afterwards the model simulations are performed with realistic forcing for the year 2014 as described in Section 5.3.1. The yearly averaged decrease in initial riverine water concentration shows that after approximately six days 50 % and after 30 days only 2 % of the initial Warnow water is left (Fig. 40). When repeating the simulations with the same forcing data, but using a bathymetry reconstructed by using historical navigational maps of the year 1880 (Fig. 39b), the water exchange is much slower than compared to today's bathymetry (approximately 35 % of the initial water after 30 days).

Note that today's shipping channel has a water depth of about 15 m while the historical channel is only approximately 4 m deep, underlining the influence of river deepening on the dynamics in the estuary.
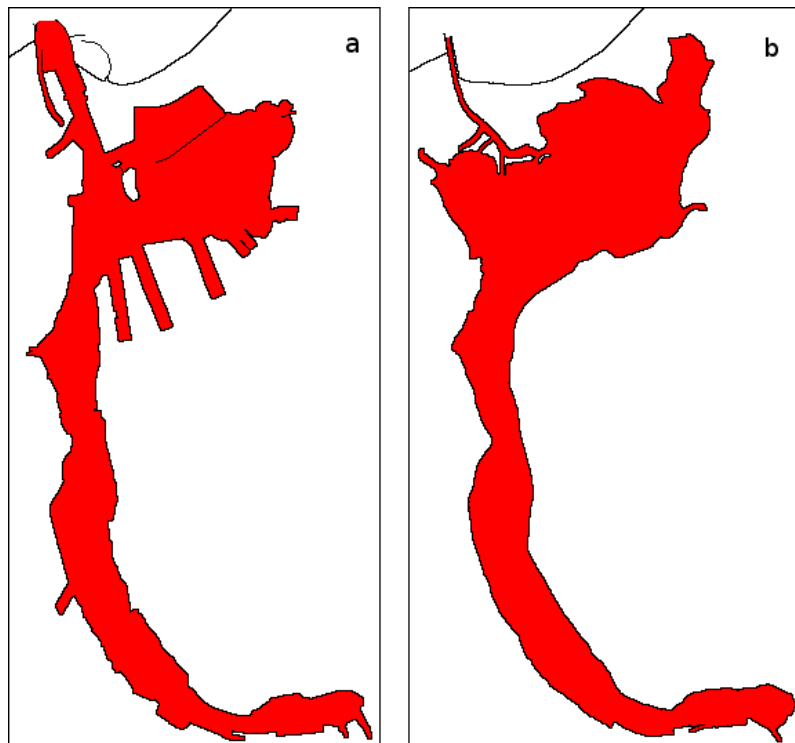

Figure 39: Initial concentration of a passive tracer in the Warnow estuary for the year 2014 (a) and 1880 (b).
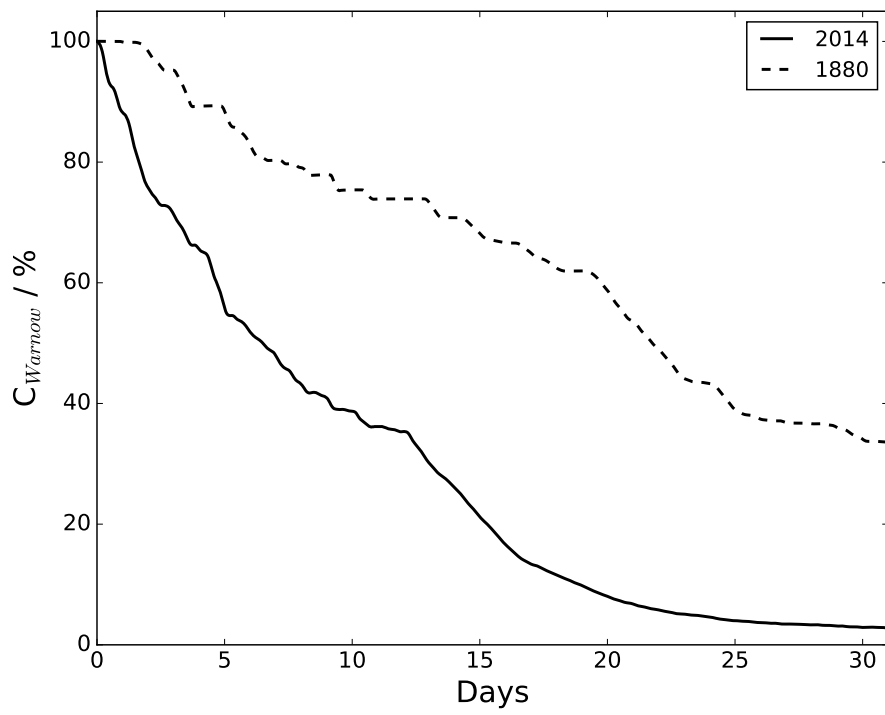
Figure 40: Annually averaged decrease of monthly initialized riverine water in the Warnow estuary.

Selbstständigkeitserklärung

Ich versichere hiermit an Eides statt, dass ich die vorliegende Arbeit selbstständig angefertigt und ohne fremde Hilfe verfasst habe. Dazu habe ich keine außer den von mir angegebenen Hilfsmitteln und Quellen verwendet und die den benutzten Werken inhaltlich und wörtlich entnommenen Stellen habe ich als solche kenntlich gemacht.

Rostock, den